Quantification of Microscopic Brain Structures Using Diffusion Magnetic Resonance



Wilfred W. Lam

Keble College

University of Oxford

A Thesis Submitted for the Degree of

Doctor of Philosophy

Trinity 2014

Quantification of Microscopic Brain Structures Using Diffusion Magnetic Resonance

Wilfred W. Lam
Keble College, University of Oxford

A Thesis Submitted for the Degree of Doctor of Philosophy
Trinity 2014

Abstract

Diffusion-weighted magnetic resonance imaging can be used to estimate microstructural parameters of white matter in the brain. Two complementary techniques are investigated: the use of the temporal diffusion spectrum to explore small length scales and the STEAM technique to probe larger features.

The diffusion spectrum has the potential to be more sensitive to small pores compared to conventional time-dependent diffusion. However, analytical expressions for the diffusion spectrum of particles only exist for simple geometries such as cylinders, which are often used as a model for intra-axonal diffusion. We propose a mathematical model for the extra-axonal space with parameters that are related to the microstructural properties of pore size, tortuosity, and surface-to-volume ratio. Measurements were made with an extra-axonal space phantom to validate the model. Fitted values for the phantom pore size match those from simulation.

We extend the model to include the intra-axonal signal contribution. However, the parameters used to describe the intra- and extra-axonal spaces are related and it is important to remove redundant parameters to avoid overparameterization, which would make the model less robust. We propose analytical expressions to simplify the model. The model was then applied to measurements on fixed corpus callosum, which is a model system consisting of parallel axons. The estimated values of the axon volume fraction and mean and standard deviation of the axon radius distribution are comparable to those found in literature.

Temporal diffusion spectra are useful for measuring the geometric properties of small spaces such as axon radii. However, longer diffusion times accessible using the STEAM sequence are necessary to probe structures with longer diffusion distances such as those parallel to the direction of axons. We used a model from the literature originally developed for use with animal magnetic resonance scanners and simplified it to quantify axial hindrance from data acquired on healthy volunteers in a clinical scanner. The interpretation of axial hindrance, which is a largely unexplored area of research, is discussed.

Acknowledgements

First, I would like to thank my supervisors Karla Miller and Saâd Jbabdi for believing in me, continually teaching me how to communicate, providing motivation when necessary, and looking out for me at all times.

I am indebted to many collaborators including: from New York University, Prof. Els Fieremans and Dr. Lauren Burcaw for taking the effort to produce a labour-intensive phantom; from University College London, Dr. Bernard Siow and Prof. Daniel Alexander for providing time and the opportunity to acquire data with a state of the art MR scanner – I'll always remember the enjoyable conversations during late night scans with Bernard; and from Oxford, Dr. Rogier Mars for providing the brain specimen, Dr. Steven Chance for dissecting it, and Dr. Sean Foxley for demonstrating how to prepare it. My studies were also assisted financially by the Nuffield Department of Clinical Neurosciences and the Department of Experimental Psychology at Oxford, the Natural Sciences and Engineering Research Council of Canada, Guarantors of Brain, and the Keble Association.

I owe many thanks to the FMRIB Physics Group for spending countless hours in the scanner for my experiments, for the entertaining lunchtime conversations, and especially for taking the initiative to water the FMRIB jungle after my departure. Special thanks go to James for helping me get started with my work and interesting technical discussions, Ti for calculating the maximum volume fractions for random packing, and Nadine for making the agar phantom. Thanks too to Bolton, Jerome, and everyone else at the BSB for keeping me company during long hours in a windowless MR scanner control room.

I really am most grateful to Rachel for turning her life upside down to be close to me during my studies and always gently nudging me to improve both my work and as a person. I also thank Angus and Colleen for letting us drag them around England and hosting our dumpling parties.

All these people made my stay in the UK full of wonderful memories.

Finally, I would like to thank my parents for allowing me to pursue my interests and supporting me in whatever I do.

Contents

Contents i

List of Tables v

List of Figures vii

List of Symbols and Abbreviations ix

List of Publications xi

1 Introduction 1
- 1.1 Motivation . . . 1
- 1.2 Thesis Outline . . . 2

2 Background 3
- 2.1 White Matter Physiology . . . 3
  - 2.1.1 Components . . . 5
    - 2.1.1.1 Axons . . . 5
    - 2.1.1.2 Glial Cells . . . 5
    - 2.1.1.3 Corpus Callosum: A Model System for Microstructure 8
    - 2.1.1.4 Myelin . . . 10
  - 2.1.2 Pathophysiology . . . 11
    - 2.1.2.1 Myelin Degradation . . . 11
    - 2.1.2.2 Axon Loss . . . 12
    - 2.1.2.3 Increased Membrane Permeability . . . 12
    - 2.1.2.4 Changes in Glial Cell Number . . . 13
  - 2.1.3 MR-Relevant Physical Properties . . . 13
    - 2.1.3.1 Diffusivity . . . 14
    - 2.1.3.2 Tortuosity . . . 16
    - 2.1.3.3 Extracellular Volume Fraction . . . 17
    - 2.1.3.4 Permeability . . . 17
- 2.2 MR Basics . . . 18
  - 2.2.1 Polarization . . . 18
  - 2.2.2 Excitation . . . 20
  - 2.2.3 Intrinsic Signal Decay . . . 20
  - 2.2.4 Signal Decay from Magnetic Field Inhomogeneity . . . 21

2.2.5 Spin Echo . . . 22
2.2.6 Spatial Encoding . . . 22
2.2.7 Signal Acquisition . . . 23
2.2.7.1 Single-Line Readout . . . 24
2.2.7.2 Echo-Planar Readout . . . 25
2.2.8 Diffusion Encoding . . . 26
2.2.9 Diffusion MR Imaging Artefacts . . . 28
2.2.9.1 Eddy Current Effects . . . 28
2.2.9.2 Susceptibility Effects . . . 29
2.2.9.3 Bulk and Pulsatile Motion . . . 29
2.3 Estimating Properties of White Matter with MR . . . 30
2.3.1 Diffusion-Based . . . 30
2.3.1.1 Pulsed Gradient Spin Echo . . . 34
2.3.1.2 Oscillating Gradient Spin Echo . . . 36
2.3.1.3 Multiple-Pulsed Field Gradient . . . 37
2.3.2 Non-Diffusion-Based . . . 37
2.3.2.1 Quantitative T_2 . . . 39
2.3.2.2 Magnetization Transfer . . . 39
2.3.2.3 T_1/T_2 Ratio . . . 39

3 A Model for Extra-Axonal Diffusion Spectra 41
3.1 Introduction . . . 41
3.2 Theory . . . 43
3.2.1 The Diffusion Spectrum . . . 43
3.2.2 Preliminary Simulations . . . 44
3.2.3 Basic Exchange Model . . . 45
3.2.4 Improved Exchange Model with Variable Radius . . . 50
3.2.5 Interpretation of Model . . . 51
3.3 Methods . . . 56
3.3.1 Monte Carlo Simulations . . . 56
3.3.2 Forward Model Comparison to Simulations for Regular Packing 59
3.3.3 Model Fitting . . . 59
3.3.4 Describing the Microstructure . . . 60
3.4 Results . . . 61
3.4.1 Forward Model Comparison to Simulations for Regular Packing 61
3.4.2 Model Fitting . . . 62
3.5 Discussion . . . 71
3.5.1 Alternative Models . . . 71
3.5.2 Practical Considerations . . . 74
3.5.3 Model Considerations . . . 76
3.6 Conclusions . . . 76
3.A Calculations to Support the Fast Exchange Limit Assumption . . . 76
3.B Geometric Quantities for Periodically Packed Cylinders . . . 78
3.B.1 Effective Pore Radius . . . 78
3.B.2 Pore Surface-to-Volume Ratio . . . 78

4 Measurements of Diffusion Spectra **79**
4.1 Introduction . . . 79
4.2 Fibre Phantom Experiment . . . 80
4.2.1 Methods . . . 81
4.2.1.1 Experiment . . . 81
4.2.1.2 Analysis . . . 84
4.2.1.3 Simulations . . . 84
4.2.1.4 Forward Modelling . . . 85
4.2.2 Results . . . 86
4.2.2.1 Experiment . . . 86
4.2.2.2 Simulations . . . 91
4.3 An Extra- and Intra-Axonal Space Model . . . 94
4.3.1 Full Model . . . 94
4.3.2 Simplified Model: Relation between Axon and Pore Radii . . . 95
4.3.3 Comparison of Simplified Model to Simulations . . . 99
4.3.3.1 Methods . . . 99
4.3.3.2 Results . . . 99
4.4 Brain Specimen Experiment . . . 102
4.4.1 Methods . . . 102
4.4.1.1 Experiment . . . 102
4.4.1.2 Analysis . . . 104
4.4.2 Results . . . 105
4.5 Discussion . . . 112
4.5.1 Alternative Models . . . 112
4.5.2 Insights from Experiments and Future Work . . . 113
4.5.2.1 Hindered Diffusion "Parallel" to Axons . . . 113
4.5.2.2 Mismatch between Measured and Fit $D(0)$ . . . 114
4.5.2.3 Noisy $D(\omega)$ with Axons Perpendicular to the Field . . . 114
4.6 Conclusions . . . 115

5 Measurements at Long Diffusion Time **117**
5.1 Introduction . . . 117
5.1.1 STEAM Sequence . . . 118
5.1.2 Three-Pool Model . . . 119
5.2 Methods . . . 128
5.2.1 Measurements . . . 128
5.2.2 Scan Parameters . . . 128
5.2.3 Isotropic Phantoms . . . 129
5.2.4 Anisotropic Phantom . . . 129
5.2.5 Healthy Volunteers . . . 130
5.2.6 Analysis . . . 131
5.3 Results . . . 134
5.3.1 Measurements . . . 134
5.3.1.1 Isotropic Phantoms . . . 134
5.3.1.2 Anisotropic Phantom . . . 134

5.3.1.3 Healthy Volunteers . . . 135
5.3.2 Model Fitting . . . 136
5.4 Discussion . . . 143
5.4.1 Fitted Parameter Comparison with Literature . . . 143
5.4.2 Diffusion Parallel to Axons . . . 144
5.4.3 Model Assumptions . . . 146
5.5 Conclusions . . . 147

6 Summary and Future Work **149**
6.1 Future Work . . . 150
6.1.1 EAS Diffusion Spectrum Model Improvement . . . 150
6.1.2 EAS Diffusion Spectrum Model Validation . . . 150
6.1.3 EAS Diffusion Spectra of Tissue . . . 151
6.1.4 The Origins of Axial Hindered Diffusion . . . 152

References **153**

List of Tables

2.1 Values of T_1 and T_2 in Healthy, In Vivo White Matter 21

3.1 Monte Carlo Simulation Parameters 58
3.2 Recent Oscillating Gradient Experiments in Literature 75

4.1 Diffusion Gradient Parameters Used for Fibre Phantom 83
4.2 Simulated and Fitted Values of Model Parameters for Fibre Phantom 92
4.3 Diffusion Gradient Parameters Used for Specimens 105
4.4 Fitted and Literature Values of Model Parameters for Specimens . . . 111

5.1 Three-Pool Model Parameters 122
5.2 Diffusion Parameters for STEAM and Spin Echo Experiments 129
5.3 Non-Diffusion Parameters for STEAM and Spin Echo experiments . . 130
5.4 Non-Linear Least Squares Initial Values for Full Three-Pool Model . . 132
5.5 Summary of Models Fitted to STEAM Data 133
5.6 Fitted Parameters of Two-Pool Model with Impermeable Ellipsoids . 141

List of Figures

2.1 Allocation of Space in Optic Nerve . . . 4
2.2 Myelinated Axon and Oligodendrocyte . . . 6
2.3 Micrograph of Oligodendrocyte . . . 7
2.4 Micrograph of Astrocyte . . . 8
2.5 MR Image of Human Corpus Callosum . . . 9
2.6 Distributions of Human Corpus Callosum Axon Diameter . . . 10
2.7 Micrograph of Myelinated Axon . . . 11
2.8 Particles Undergoing Free, Hindered, and Restricted Diffusion . . . 15
2.9 Equilibrium Spin Distribution in External Magnetic Field . . . 19
2.10 Spin Distribution with Application of RF Pulse . . . 20
2.11 Formation of Spin Echo . . . 22
2.12 Single-Line Readout k-Space Trajectory . . . 25
2.13 Echo-Planar Readout k-Space Trajectory . . . 26
2.14 Pulsed Gradient Spin Echo Sequence . . . 27
2.15 Velocity Autocorrelation Functions and Diffusion Spectra . . . 32
2.16 Oscillating Gradient Spin Echo Sequence . . . 36
2.17 PGSE and OGSE Sequences and Corresponding $F(\omega)$ . . . 38

3.1 $D(\omega)$ for Intra- and Extra-Axonal Space . . . 45
3.2 Simulated $D_{\text{ext}}(\omega)$ with $b = 0.5$, 1, and 2 ms/μm^2 . . . 47
3.3 Restricted Component of EAS Diffusion Spectrum and Variable Radius 49
3.4 Calculation of R_{pore} . . . 52
3.5 Square and Hexagonally Packed Cylinders . . . 53
3.6 $D_{\text{ext}}(\omega)$ Model Parameters . . . 54
3.7 Calculation of R_{min} . . . 54
3.8 Explanation of How R_0 is Affected by p . . . 55
3.9 Randomly Packed Cylinders . . . 57
3.10 EAS Pore Segmentation for Randomly Packed Cylinders . . . 61
3.11 $D_{\text{ext}}(\omega)$ for Square and Hexagonally Packed Cylinders . . . 63
3.12 $D_{\text{ext}}(\omega)$ Residuals for Square and Hexagonally Packed Cylinders . . . 64
3.13 $D_{\text{ext}}(\omega)$ for Randomly Packed Cylinders . . . 65
3.14 $D_{\text{ext}}(\omega)$ Residuals for Randomly Packed Cylinders . . . 65
3.15 $1/\lambda$, R_0, and R_∞ for Square and Hexagonally Packed Cylinders . . . 66
3.16 L_{abut} and L for Square and Hexagonally Packed Cylinders . . . 68
3.17 R_0 and R_∞ for Randomly Packed Cylinders . . . 70
3.18 Comparison of Fitting between Two Models . . . 72

3.19 Residuals of Fitting between Two Models 73

4.1 Fibre Phantom 80
4.2 OGSE Gradient Waveforms with and without Zero Padding 82
4.3 Axial Images of Fibre Phantom 87
4.4 CPMG Signal versus TE of Fibre Phantom 88
4.5 Measured $D(\omega)$ of Fibre Phantom 89
4.6 $1/\lambda$ versus f_{int} 90
4.7 Measured, Fitted, and Predicted $D(\omega)$ of Fibre Phantom 91
4.8 Fibre Phantom Simulation 93
4.9 Parameters of IAS and EAS Models Plotted against Each Other . . . 97
4.10 Comparison of R_{int} and Proposed Functions of R_{pore} 98
4.11 Simulated and Predicted $D(\omega)$ for Randomly Packed Cylinders 100
4.12 Fitted Values for f_{int}, $\mu_{R,\text{int}}$, and $\sigma_{R,\text{int}}$ 101
4.13 Signal from Low b-Value Scans 104
4.14 Axial Images of Genu Specimen 106
4.15 Axial Images of Mid Body Specimen 107
4.16 Axial Images of Splenium Specimen 108
4.17 CPMG Signal versus TE of Genu Specimen 109
4.18 Measured $D(\omega)$ of Specimens 110
4.19 Measured and Fitted $D(\omega)$ of Specimens 111

5.1 Pulse Diagrams for PGSE and STEAM 120
5.2 Attenuation between STEAM and Spin Echo Sequences 121
5.3 Schematic of Three-Pool Model 123
5.4 ADC versus Diffusion Direction of Agar and Liquid Soap Phantoms . 135
5.5 ADC and Attenuation versus Fibre Angle of Fibre Phantom 136
5.6 ADC and Attenuation versus Fibre Angle of In Vivo Tissue 137
5.7 Attenuation of In Vivo Tissue Fitted to Models 138
5.8 Attenuation Residuals of In Vivo Tissue 139
5.9 Bayesian Information Criteria of Models 141
5.10 Comparison of STEAM Models 142
5.11 ADC versus Fibre Angle and Fanning 145

6.1 Form of $D_{\text{ext}}(\omega)$ for Regular and Random Packing at Low ω 151

List of Symbols and Abbreviations

γ	Gyromagnetic ratio
δ	Pulsed gradient lobe duration
Δ	Diffusion time or pulsed gradient lobe onset-to-onset separation
λ	EAS tortuosity
τ	Mean residence time of particles in a compartment
ω	Gradient frequency
ADC	Apparent diffusion coefficient
b	Diffusion weighting factor
D	Diffusivity (also known as diffusion coefficient)
D_{f}	Free diffusivity
$D(\omega)$	Diffusion spectrum
E	Signal attenuation
EAS	Extra-axonal space
FWHM	Full width at half maximum
$\vec{G}$	Spatially vary magnetic field gradient
IAS	Intra-axonal space
OGSE	Oscillating gradient spin echo sequence
p	Fractional separation between adjacent cylinders
PGSE	Pulsed gradient spin echo sequence
q	Diffusion sensitivity (independent of diffusion time)
R_{int}	Axon or cylinder radius
R_{pore}	Effective radius of EAS pore
R_0	Radius of EAS restricted diffusion component at $\omega = 0$
R_∞	Radius of EAS restricted diffusion component as $\omega \to \infty$
S	Signal of a voxel
S_0	Signal of a voxel with $b = 0$
SD	Standard deviation
SE	Spin echo sequence
SNR	Signal-to-noise ratio
STEAM	Stimulated echo acquisition mode sequence
T_1	Spin–lattice relaxation time
T_2	Spin–spin relaxation time
TE	Echo time
TR	Repetition time

List of Publications

Journal Articles

Lam, W. W., Jbabdi, S., and Miller, K. L. (2015). A Model for extra-axonal diffusion spectra with frequency-dependent restriction. *Magn Reson Med*, 73(6):2306–2320.

Conference Proceedings

Lam, W. W., Jbabdi, S., and Miller, K. L. (2012). Measurement of post-mortem brain microstructure using a clinical MR scanner with oscillating gradients. In *Proceedings of the 20th Annual Meeting of ISMRM*, page 3570, Melbourne, Australia.

Lam, W. W., Jbabdi, S., and Miller, K. L. (2013). Modelling extra-axonal diffusion spectra for oscillating gradient measurements. In *Proceedings of the 21st Annual Meeting of ISMRM*, page 2074, Salt Lake City, Utah, USA.

Lam, W. W., Jbabdi, S., and Miller, K. L. (2014). A model for extra-axonal diffusion spectra. In *Proceedings of the 22nd Annual Meeting of ISMRM*, page 395, Milan, Italy.

Lam, W. W., Siow, B., Burcaw, L., Alexander, D. C., Lythgoe, M. F., Miller, K. L., and Jbabdi, S. (2015). Validation of extra-axonal diffusion spectrum model with frequency-dependent restriction. In *Proceedings of the 23rd Annual Meeting of ISMRM*, page 2775, Toronto, Ontario, Canada.

Lam, W. W., Siow, B., Foxley, S., Chance, Steven A., Mars, Rogier B., Alexander, D. C., Lythgoe, M. F., Miller, K. L., and Jbabdi, S. (2015). Estimation of microstructural properties of fixed corpus callosum from OGSE measurements. In *Proceedings of the 23rd Annual Meeting of ISMRM*, page 2785, Toronto, Ontario, Canada.

Lam, W. W., Miller, K. L., Kleinnijenhuis, M., and Jbabdi, S. (2015). Longitudinally hindered diffusion of in vivo human white matter at long diffusion time. In *Proceedings of the 23rd Annual Meeting of ISMRM*, page 2776, Toronto, Ontario, Canada.

Kleinnijenhuis, M., Mollink, J., Kinchesh, P., **Lam, W. W.**, Galinsky, V. L., Frank, L. R., Smart, S. C., Jbabdi, S., and Miller, K. L. (2015). Monte Carlo diffusion simulations disambiguate the biophysical mechanisms of diffusion hinderance along tracts. In *Proceedings of the 23rd Annual Meeting of ISMRM*, page 2756, Toronto, Ontario, Canada.

Kleinnijenhuis, M., Mollink, J., Kinchesh, P., **Lam, W.**, Khrapitchev, A., Sibson, N., Galinsky, V., Frank, L., Smart, S., Jbabdi, S., and Miller, K. (2015). Monte Carlo simulations disambiguate the biophysical mechanisms of diffusion hindrance along tracts. In *Proceedings of the 21st Annual Meeting of OHBM*, page 1769, Honolulu, Hawaii, USA.

Chapter 1

Introduction

Magnetic resonance (MR) imaging offers insights into the structure and function of the brain non-destructively, which would be useful to both scientists and clinicians. Diffusion-weighted imaging in particular can quantitatively inform on the microstructure of the brain.

1.1 Motivation

There are a number of debilitating diseases that affect white matter such as multiple sclerosis, the leukodystrophies, and Alzheimer's disease. MR potentially offers a non-invasive opportunity to diagnose and monitor changes in these diseases. Current methods in diffusion MR imaging do not report on microstructural geometry with sufficient specificity to identify changes in disease. This thesis aims to develop models and techniques that could help ameliorate this problem. There also could be benefits to basic science with improved understanding of the microstructure of white matter.

1.2 Thesis Outline

Chapter 2 gives a brief overview of the relevant background to this thesis. Topics include white matter physiology and pathophysiology, selected concepts in MR, and techniques used to estimate the properties of white matter with MR.

The three research chapters that follow in this thesis are generally organized chronologically in the order the work was done.

Chapter 3 introduces a new model that relates the motional properties of diffusing particles, embodied by the diffusion spectrum, in the extra-axonal space (EAS) to geometric properties of that space. We demonstrate that the model can predict diffusion spectra generated by Monte Carlo simulations of idealized axons under various packing arrangements and densities.

Chapter 4 describes experiments to measure the diffusion spectrum of a phantom designed to mimic the EAS and fitting the model to the spectrum from Chapter 3 to estimate the known geometry of the phantom. The EAS model is extended to include the intra-axonal space (IAS), simplified to make fitting more robust, and applied to diffusion spectra acquired in ex vivo brain specimens.

Chapter 5 presents the unexpected result that the apparent diffusion coefficient along the axial direction of axons in the brain is significantly hindered. This finding was hinted at in the measurements on specimens in Chapter 4 and is further explored in healthy volunteers.

Finally, Chapter 6 summarizes the contributions of this thesis and postulates future work to extend and clarify the results of the experiments presented.

Chapter 2

Background

This chapter will introduce the basic biology of white matter in the brain; the physical and magnetic resonance (MR)-derived properties used to describe white matter; and specific MR techniques and models used to estimate these properties. Only details relevant to this thesis will be included in this chapter, which is not meant to be an exhaustive review.

2.1 White Matter Physiology

The brain is a complex organ made of many tissue types arranged in a myriad of ways. This thesis concerns white matter, which is chiefly made up of axons, myelin, and three types of glial cells: astrocytes, oligodendrocytes, and microglia (discussed below). The white matter regions of the brain contain long-range connections between the brain's gray matter "processing units", which are characterized by cellular projections (axons) that are often covered in a white insulating substance (myelin). The allocation of space in the optic nerve, an example of white matter, is given in Fig. 2.1.

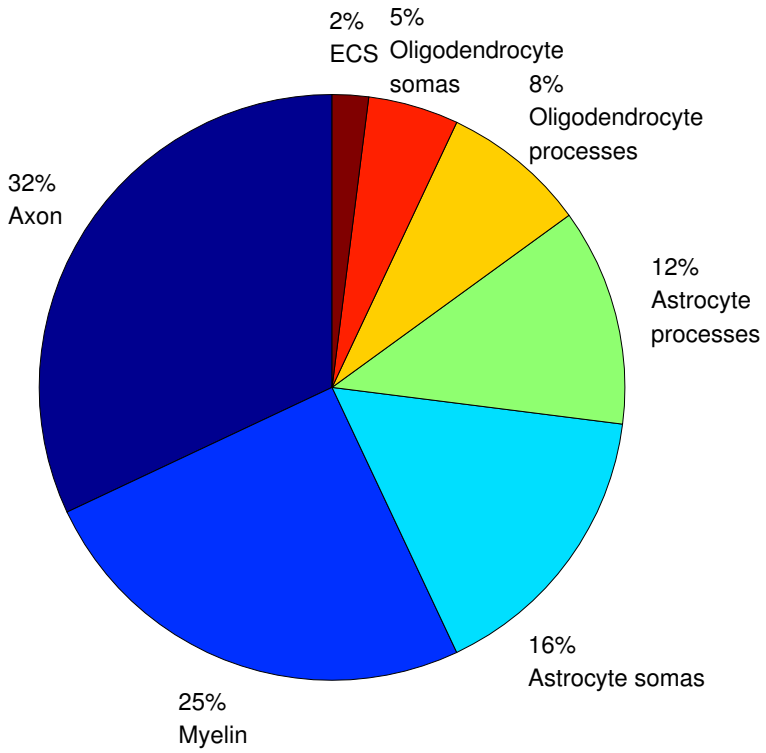


Figure 2.1: Allocation of space in the guinea pig optic nerve from electron microscopy (Perge et al., 2009). ECS denotes the extracellular space. Microglia have been excluded. Note that the 2% allocated to ECS is significantly less than the (20–22 $\pm$ 1)% measured in other white matter (Mazel et al., 1998).

2.1.1 Components

2.1.1.1 Axons

An axon is a long extension (process) from the cell body (soma) of one neuron that connects to a dendrite on another (Fig. 2.2) at a junction called a synapse. Axons have diameters in the range $\approx$ 0.1–10 µm (Perge et al., 2012) and lengths spanning short distances between adjacent gyri to longer ones spanning brain hemispheres and still longer ones in the spinal cord and peripheral nervous system. Axons contain mostly neurofilaments with the balance being microtubules and mitochondria (Lee and Cleveland, 1996). Neurofilament number and spacing affect axon diameter (Kumar et al., 2002). Axons may be wrapped in a myelin sheath, which is secreted by oligodendrocytes in the central nervous system to increase signal conduction speed (Fig. 2.2).

The human brain relies on the precise timing and rapid transmission of signals in certain axons (and on firing rate, which is less precise, in others) to process information. Precision is improved by myelination and propagation velocity is increased by both larger axon diameter and myelination in a metabolically efficient manner (Wang et al., 2008; Perge et al., 2012). Myelination plays a role in learning and continues to change throughout life (Fields, 2008). Dysfunctional myelination leads to a host of neurological conditions, which will be discussed below.

2.1.1.2 Glial Cells

Glial cells are non-neuronal cells, but also perform functions that are intrinsic to the functioning of the brain. A brief description of each major type follows.

Oligodendrocytes (Fig. 2.3) are mainly responsible for the myelination of axons in the central nervous system with a minority of satellite oligodendrocytes not connected to a myelin sheath and instead serving to regulate the neuronal microenvironment

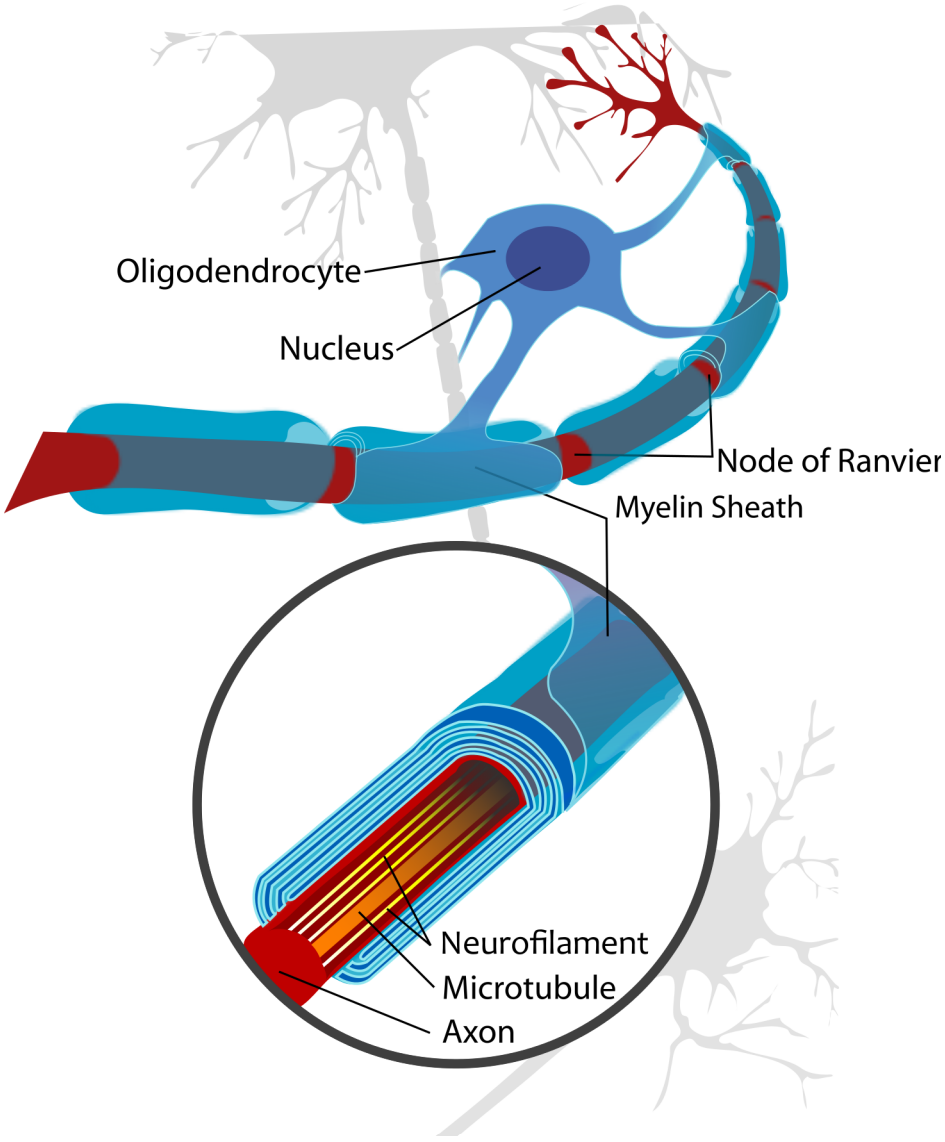


Figure 2.2: Myelinated axon and oligodendrocyte with inset showing the two components of the cytoskeleton: the neurofilament and microtubule. (Adapted from Neuron_with_oligodendrocyte_and_myelin_sheath.svg / Wikimedia Commons / Public Domain)

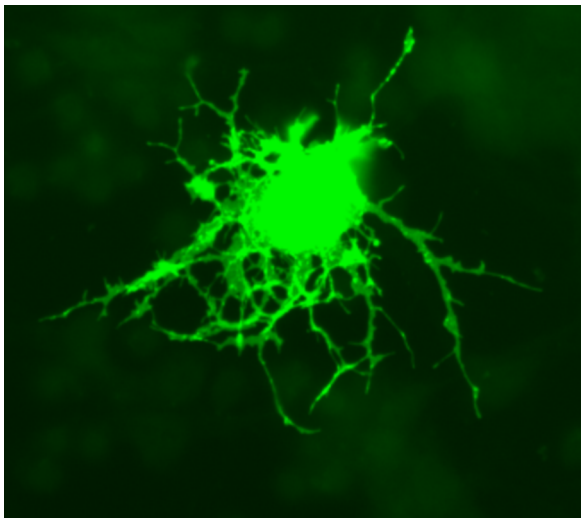


Figure 2.3: Mouse oligodendrocyte transfected with green fluorescent protein from cell culture. (User:Methoxyroxy / Wikimedia Commons / Public Domain)

(Ludwin, 1997; Baumann and Pham-Dinh, 2001). In the peripheral nervous system, the role of myelination is performed by Schwann cells instead of oligodendrocytes. Oligodendrocytes are approximately spherical with an average diameter of 12–14 μm (Weruaga-Prieto et al., 1996; Bakiri et al., 2011).

Astrocytes (Fig. 2.4) have diverse morphology, location, and responsibilities. Fibrous astrocytes, which are found in white matter, are equally spaced with overlapping domains (183 ± 6.1 μm in diameter) defined by their processes, which are aligned with axons, terminate at nodes of Ranvier, and thought to provide structural support (Oberheim et al., 2009; Wang and Bordey, 2008). They also regulate the environment for oligodendrocytes (Lundgaard et al., 2014). Protoplasmic astrocytes, which are found in grey matter, are larger and have more processes than fibrous astrocytes (Lundgaard et al., 2014). Their purpose includes synaptogenesis, angiogenesis, extracellular ion buffering, neurotransmitter uptake and metabolism, and blood–brain barrier maintenance (Wang and Bordey, 2008). Interlaminar and varicose projection astrocytes are also found in the grey matter of primates, but not rodents, and their function is unknown (Oberheim et al., 2009). The ratio of astrocytes to neurons increases dramatically with brain complexity (Nedergaard et al., 2003). There is

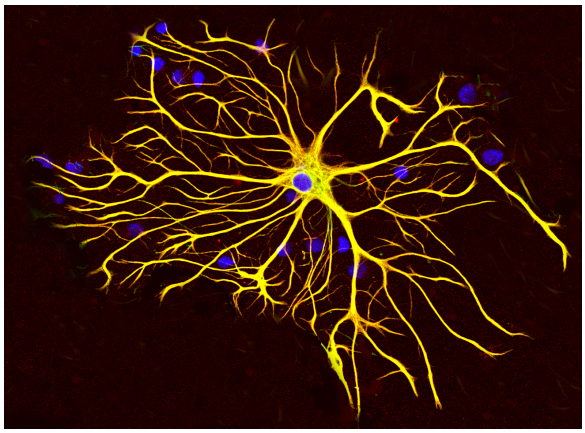


Figure 2.4: Confocal micrograph of a rat astrocyte from cell culture stained with antibodies to glial fibrillary acidic protein (red) and vimentin (green). Both proteins are present in the neurofilaments, so the cell appears yellow. DNA is visualized with DAPI stain (blue) and reveals the nuclei of the astrocyte and other cells. (Gerry Shaw / Wikimedia Commons / CC-BY-SA-3.0)

on-going research into the heterogeneous functions of astrocytes (Zhang and Barres, 2010).

Microglia are immune cells that make up approximately 10% of glial cells and can double in number during injury, infection, or endogenous toxins (Barres, 2008). They are also an area of active research (Hanisch, 2013).

2.1.1.3 Corpus Callosum: A Model System for Microstructure

The experimental data in Chapters 4 and 5 come from the corpus callosum, a structure of coherent axons at the midline of the brain that connects the hemispheres. It provides a convenient environment for testing white matter microstructural measures because it is large and, thus, is easy to localize and provides ample signal; has mainly parallel fibres; and has well-characterized microstructural variation along its length. The corpus callosum is generally divided by anatomists into the rostrum, genu, body, and splenium (Fig. 2.5). Distributions of the corpus callosum axon diameters are shown in Fig. 2.6.

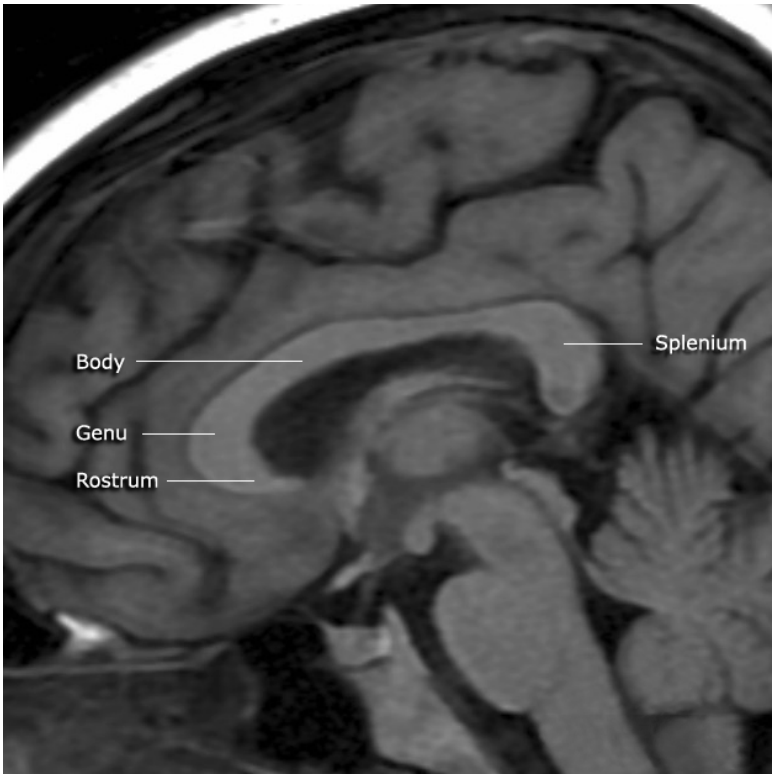


Figure 2.5: MR image of the human corpus callosum. (Frank Gaillard (Radiopaedia.org) / Wikimedia Commons / CC-BY-SA-3.0 / GFDL)

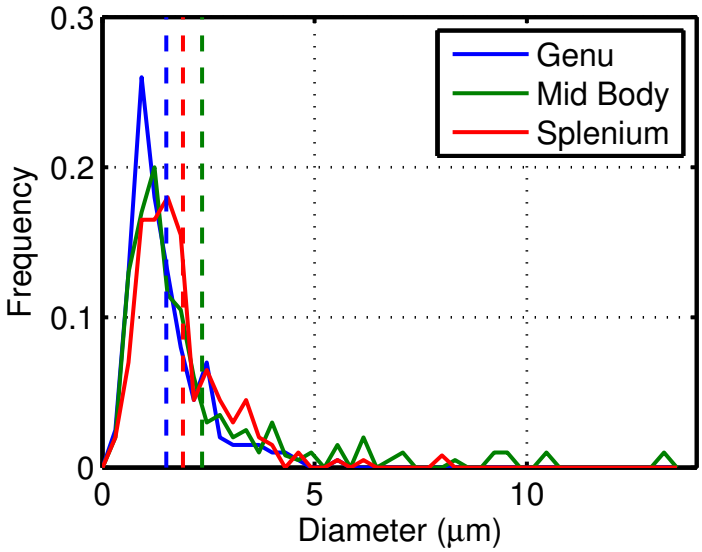


Figure 2.6: Distributions of the human corpus callosum axon diameter for the genu, mid body, and splenium from electron microscopy (Aboitiz et al., 1992). These diameters have been scaled by the factor cited in the reference to reverse the effects of shrinkage after fixation and embedding in paraffin and differ from Fig. 4 of the reference, which shows uncorrected values. The dashed lines indicate the probability-weighted mean diameters and show the low–high–low anterior–posterior trend reported in literature (Alexander et al., 2010).

2.1.1.4 Myelin

Myelin is a fatty substance that is secreted by oligodendrocytes in the central nervous system and imparts the white colour to white matter. It is found rolled around axons (Fig. 2.7) in discrete segments separated by myelin-free segments denoted nodes of Ranvier (Fig. 2.2). Myelinated segments are referred to as internodes. The ratio between axon diameter and fibre diameter (diameter of axon and myelin) is termed the g ratio. A value of approximately 0.6 has been derived to yield the maximal conduction velocity of signals along axons (Rushton, 1951), but the g ratio has been found to vary with sex and axon diameter (Paus and Toro, 2009).

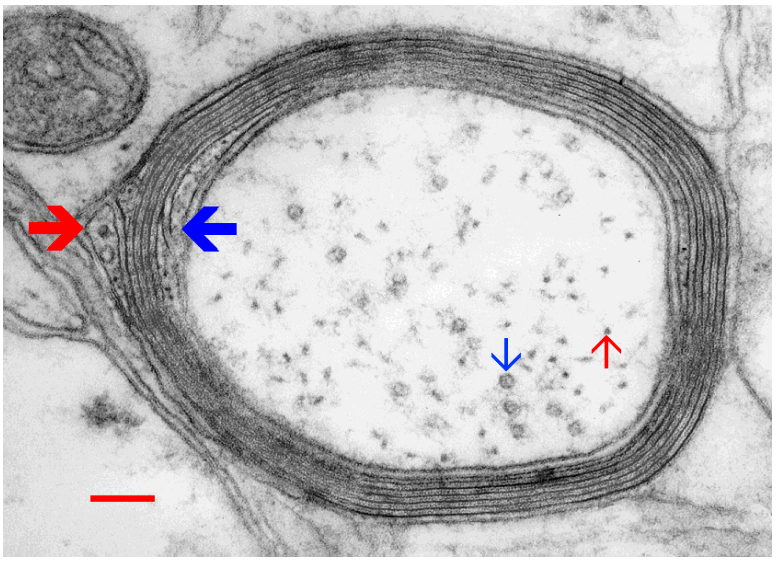


Figure 2.7: Electron micrograph of a myelinated axon (human, neocortex) in cross section. The outer (large red arrow) and inner (large blue arrow) cytoplasmic tongues of an oligodendrocyte process are apparent. A microtubule is marked by the small blue arrow and a neurofilament by the red. Bar = 200 nm. (Atlas of Ultrastructural Neurocytology, http://synapses.clm.utexas.edu/atlas/contents.stm)

2.1.2 Pathophysiology

All the properties discussed above (e.g., myelination, axon size distribution, and glial cells) can relate to white matter dysfunction. Below, several categories of pathophysiology are presented, each with a brief description of the impact of representative pathology.

2.1.2.1 Myelin Degradation

There are many causes of myelin degradation. Some are genetic, either inherited or from mutation, and affect the formation of myelin by interfering with normal oligodendrocyte (Nave and Trapp, 2008) or astrocyte (Lundgaard et al., 2014) function. Others have later onset and destroy existing, healthy myelin.

Dysmyelination refers to defective structure and function of the myelin sheath and the genetic diseases that lead to dysmyelination are referred to as leukodystrophies. These diseases can be juvenile- or adult-onset and symptoms can include demen-

tia, paraparesis, ataxia, hyperirritability, hemiparesis, and seizures depending on the type of leukodystrophy (Schmahmann et al., 2008). For the juvenile-onset leukodystrophies, the population incidence has been measured to be 13 per 100,000 live births, mortality 34%, and average age at death 8.2 years (Bonkowsky et al., 2010).

Demyelination refers to the destruction of the myelin sheath, which is a hallmark of diseases such as multiple sclerosis (MS). This disease causes recurring episodes of progressively worse neurological dysfunction and has no cure. The dysfunction includes cognitive impairment, loss of vision, tremor, diplopia, weakness, pain, and fatigue (Compston and Coles, 2008). The global median estimated prevalence and incidence of MS is 30 and 2.5 per 100,000, respectively, and up to 60% of people with MS are no longer ambulatory 20 years after onset (World Health Organization, 2008).

2.1.2.2 Axon Loss

Axon loss can occur for a variety of reasons. Material to maintain the axon is transported intra-axonally from the cell body. When there is a cut or crushing of an axon, the portion of the axon distal to the injury will undergo an axon-specific degradation known as Wallerian degeneration, which is distinct from apoptosis (Raff et al., 2002). Axons can also exhibit Wallerian-like degeneration from the distal end in a retrograde fashion without any axonal transection; this is termed dying back disorder. This is seen in motor neuron, Alzheimer's, Parkinson's, and Huntington's diseases and are associated with accumulations of specific proteins (Raff et al., 2002; Coleman and Freeman, 2010). However, in contrast to axon loss, there is little literature describing axon shrinkage.

2.1.2.3 Increased Membrane Permeability

The axon membrane (axolemma) increases in permeability in the presence of acidosis (Hsu et al., 2000) and traumatic axon injury (Wolf et al., 2001) and in the cases of

immune-mediated diseases such as MS (Kornek et al., 2001). Permeability could be an important biomarker in addition to those listed above.

2.1.2.4 Changes in Glial Cell Number

Changes in glial cell number can be a marker for inflammation in disease. For example, in those with MS, there is inflammation throughout CNS white matter, depletion of oligodendrocytes, and an abnormal increase in the number of astrocytes (Compston and Coles, 2008). In those with amyotrophic lateral sclerosis, the number of microglia and astrocytes was observed to be significantly higher than in controls in all areas of the corpus callosum except the rostrum (Sugiyama et al., 2013).

More details of white matter pathologies can be found in literature (Medana and Esiri, 2003; Schmahmann et al., 2008).

2.1.3 MR-Relevant Physical Properties

In this section, the principle physical properties used to characterise white matter in the context of diffusion MR imaging are introduced. We will return to these properties at the end of this chapter, after reviewing the basic concepts underpinning MR imaging.

As related to the diseases presented above, the most directly relevant physical properties are the diameter distribution, myelin thickness, and the surface-to-volume ratio of the axons, which can change with axonal loss and myelin degradation. However, these cannot be directly observed using MR techniques. Instead they influence the properties listed below and can potentially be inferred by measurements and an appropriate model. The physical properties of glial cells is of importance as well, but are often ignored when a basic model is sought.

2.1.3.1 Diffusivity

The diffusivity or diffusion coefficient is a measure of the random movement of particles due to Brownian motion, which is caused by collisions of particles and is a function of their thermal energy. Formally, it is the proportionality constant relating the diffusion flux (flow per unit area) of a substance to its spatial concentration gradient assuming steady state conditions (Callaghan, 1991). In the absence of any barriers or hindrances to diffusion (Fig. 2.8), displacement is dictated by the free diffusion coefficient D_f of a given molecule and is related to the mean squared free diffusion displacement x_f in one dimension by Einstein's equation (Einstein, 1905)

$$\left\langle x_\mathrm{f}^2 \right\rangle = 2\Delta D_\mathrm{f}, \tag{2.1}$$

where Δ is the diffusion time of the measurement. The free diffusivity of water is 2.919 $\mu\mathrm{m}^2/\mathrm{ms}$ at 35 °C (Mills, 1973) and can be calculated for other temperatures T using the following (Delannoy et al., 1991):

$$\frac{1}{T} = \frac{1}{T_0} - \frac{k}{E_\mathrm{a}} \ln\left(\frac{D}{D_0}\right) \tag{2.2}$$

where D_0 is the diffusivity at a reference temperature T_0, k is Boltzmann's constant, and E_a is the activation energy for translational molecular diffusion, which has been measured to be approximately 0.18 eV (Simpson and Carr, 1958). This equation assumes small or linear variations of E_a with T (Le Bihan et al., 1989).

Where there are hindrances to diffusion in the form of physical barriers, the measured diffusivity will be lower than free diffusivity and is termed the apparent diffusion coefficient (ADC). Spaces containing boundaries (Fig. 2.8) can exhibit 1) restricted diffusion, in which the mean square displacement of particles is bounded, and, at long diffusion times, the ADC becomes zero (and the displacement immeasurable)

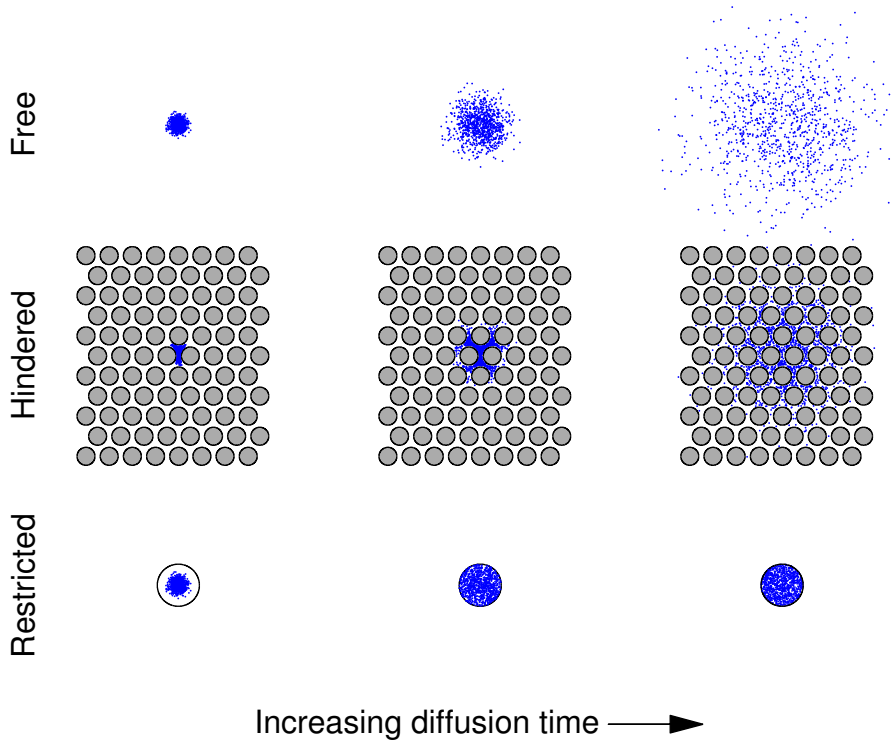


Figure 2.8: Particles undergoing free, hindered, and restricted diffusion at a range of diffusion times. At long diffusion times, the mean ADC in restricted spaces approaches zero and displacement information cannot be recovered.

or 2) hindered diffusion, in which the mean square displacement of particles is not bounded, but less than that for free diffusion (Sen and Basser, 2005b). This has been used to quantify the length scales of restrictions in tissue using diffusion MR (Tanner and Stejskal, 1968), although a model and, in general, a plurality of measurements are needed. At short diffusion times, the minority of particles encounter the boundaries, but the majority do not, and the ADC is related to the surface-to-volume ratio of the particles' environment (Mitra et al., 1993). In healthy humans, apparent diffusivity parallel and perpendicular to the axis of white matter fibres falls in the range 1.09–1.71 $\mu m^2/ms$ and 0.4–1.16 $\mu m^2/ms$, respectively (Chapman et al., 2013; De Santis et al., 2014). Parallel diffusivity within single fibre axonal tracts is less than the free diffusivity of water likely due to neuronal structures such as organelles, vesicles, and the cytoskeleton and the viscosity of the axoplasm, as well as possible orientation dispersion of the axons within the tract.

2.1.3.2 Tortuosity

Tortuosity is a measure of the hindrance to diffusion by the geometry of the environment in which diffusing particles are found. Formally, tortuosity λ is the square root of the ratio of free to hindered mean squared diffusion displacements $\langle x_f^2 \rangle$ and $\langle x_h^2 \rangle$, respectively, (Nicholson, 2001):

$$\lambda = \sqrt{\langle x_f^2 \rangle \,/\, \langle x_h^2 \rangle} \tag{2.3}$$

$$= \sqrt{D_f / \mathrm{ADC}}. \tag{2.4}$$

It is unity for environments with free diffusion and infinite for those with restricted diffusion. Analytical expressions for the tortuosity of the space around periodically packed cylinders are given in Perrins et al. (1979) and Sen and Basser (2005a). In the rat corpus callosum, the tortuosity parallel and perpendicular to the fibres has been

measured to be approximately 1.48 and 1.68, respectively, and, in rat grey matter, 1.60 (Mazel et al., 1998).

For randomly packed axons idealized as parallel cylinders, the tortuosity perpendicular to the axons was calculated to be (Szafer et al., 1995)

$$\lambda = (1 - f_{\text{int}})^{-1/2}, \tag{2.5}$$

where f_{int} is the intra-axonal volume fraction. However, this has been found through simulation to primary hold at f_{int} values lower than those found in tissue (Fonteijn et al., 2009) where there is greater variability in λ than this formula predicts.

2.1.3.3 Extracellular Volume Fraction

The extracellular space (ECS) volume fraction or porosity is another important property of white matter because the ECS will have different physical properties than the intracellular space and signal models must take this into account. It has been measured in the rat corpus callosum to be 0.21 ± 0.01 (Mazel et al., 1998) and is significantly different from the ECS volume fraction presented in Fig. 2.1, but the reason for this is unclear. The measurements for Fig. 2.1 were made in optic nerve, which may have a different ECS volume fraction than in the corpus callosum.

2.1.3.4 Permeability

The permeability of a cell membrane is important to characterize, for instance, because the concentration of ions in the intra- and extra-axonal space is important for signal conduction and closely regulated (Barnett and Larkman, 2007). The mechanism which underlies passive permeability is diffusion (Mathai et al., 2008). MR is sensitive to the diffusive movement of water between different tissue compartments such as the intra-axonal, intra-glial, and extracellular spaces and models would be

more accurate if exchange between them were taken into account. The passive permeability P of a membrane is related to the physical composition of the membrane and its thickness and has been estimated in fixed optic nerve to be (0.9 ± 0.2) and $(1.7 \pm 0.3) \times 10^{-3}$ cm/s for axons and glia, respectively (Stanisz et al., 1997). This implies lower permeability with myelination, which is consistent with the relatively low diffusivities measured in myelin water of 0.37 and 0.13 μm^2/ms parallel and perpendicular to the nerve, respectively (Andrews et al., 2006).

The mean residence time of water in a compartment is closely related to P and can also be modelled to gain insight into the microscopic behaviour of water. Formally, the residence time is inversely related to both P and the surface to volume ratio of the compartment (Chen and Springer, 1981). The mean residence times of intra- and extracellular water for the in vivo rat brain is approximately 550 and 120 ms, respectively (Quirk et al., 2003), and 200 ms for intra-axonal water specifically (Landis et al., 2000). These values are much longer than typical diffusion MR measurements and many models assume no exchange between the intra- and extracellular space.

2.2 MR Basics

This section will review the most relevant concepts in MR needed to understand the work in this thesis. Many aspects of MR physics will be omitted in the interest of brevity.

2.2.1 Polarization

Hydrogen nuclei in water molecules gives rise to the signal measured with "proton" MR. Specifically, the signal is due to a vector property of the nuclei called spin, which causes nuclei to have a magnetic moment. In the absence of an external magnetic field, the magnetic moment of an ensemble of protons are oriented with equal probability

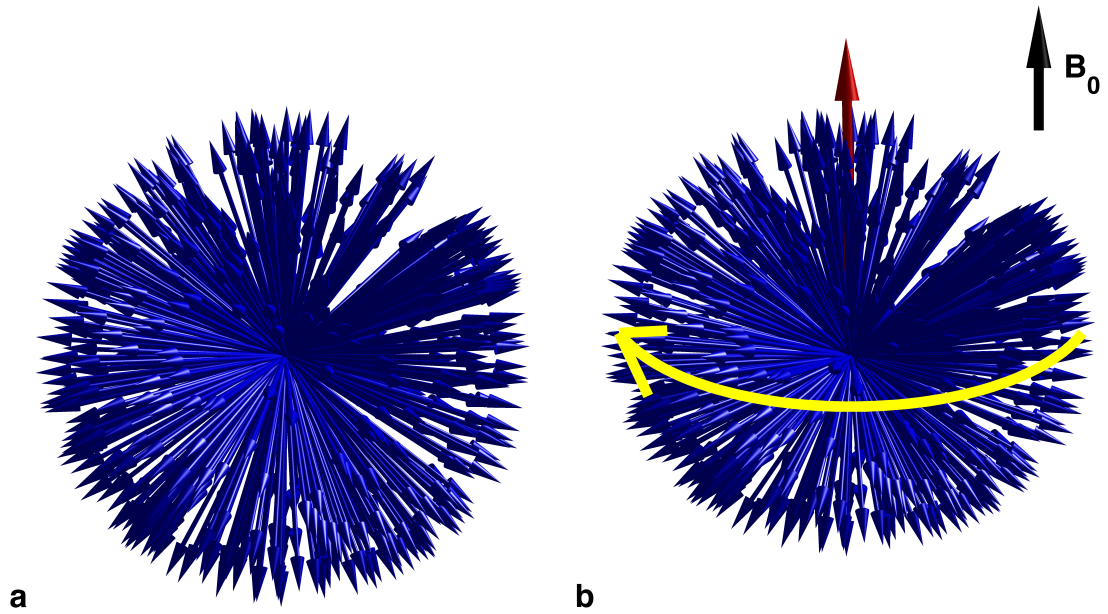


Figure 2.9: Equilibrium spin distribution (**a**) before and (**b**) after the application of an external magnetic field $\mathbf{B_0}$. The vector sum of the spins is given by the larger red arrow. The precession of the spins about $\mathbf{B_0}$ is indicated by the curved yellow arrow. The amount of polarization and magnetization have been exaggerated compared to those in typical experiments for illustrative purposes.

in all directions (Fig. 2.9a). In the presence of an external magnetic field denoted $\mathbf{B}$ (typically provided by the constant field of the superconducting magnetic of an MR scanner and denoted $\mathbf{B_0}$), the spins exhibit a directional bias (polarization) towards magnetic north of this field (Hanson, 2008). This results in a net magnetization aligned with the main field (Fig. 2.9b). The spins will also precess about this field with a frequency ω_0 (resonance or Larmor frequency)

$$\omega_0 = \gamma|\mathbf{B}| \tag{2.6}$$

where γ is the gyromagnetic ratio, a physical property of the nucleus being excited, and is approximately 267.51 rad/ms/mT for ^{1}H (Bernstein et al., 2004a). $\mathbf{B_0}$ creates a frame of reference for the experiment, defining both a principle direction (longitudinal axis) and a plane perpendicular to it (transverse plane).

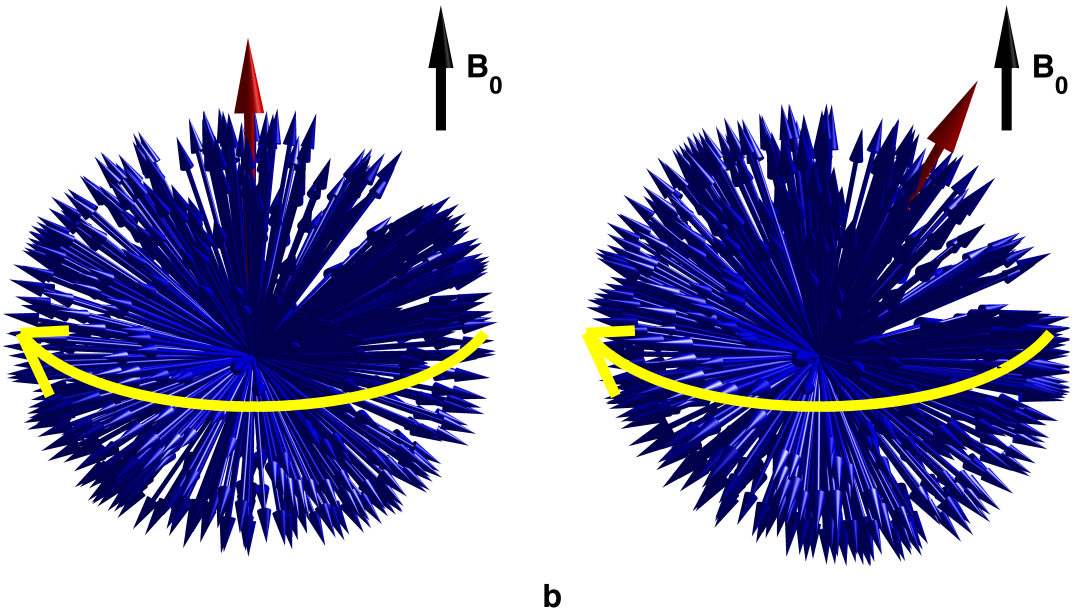


Figure 2.10: Spin distribution in an external magnetic field $\mathbf{B_0}$ (**a**) before and (**b**) after the application of an RF pulse at the resonance frequency and pointing in the direction of the reader. The vector sum of the spins is given by the larger red arrow. The precession of the spins about $\mathbf{B_0}$ is indicated by the curved yellow arrow.

2.2.2 Excitation

A second external magnetic field perpendicular to $\mathbf{B_0}$ and oscillating at the resonance frequency (usually in the radiofrequency (RF) range) is then briefly applied to "excite" the spins. This is called an RF excitation pulse. The net magnetization vector sweeps to follow the oscillating field, moving it out of its equilibrium orientation in alignment with $\mathbf{B_0}$ (Fig. 2.10b). The angle subtended by the net magnetization and magnetic north is denoted the tip or flip angle.

2.2.3 Intrinsic Signal Decay

Only magnetization that is precessing in the transverse plane can be detected by one or more radio antennae (receiver coils) and constitutes the signal from the MR scanner. When the RF field is removed, the net magnetization re-aligns with $\mathbf{B_0}$ relatively slowly with an exponential time constant T_1 in a process known as T_1 relaxation or

Tissue	T_1 (ms)	T_2 (ms)	B_0 (T)	Ref.
White matter	650 ± 50	80	1.5	Wright et al. (2008); Cox and Gowland (2010)
White matter	840 ± 50	71	3	Wright et al. (2008); Cox and Gowland (2010)
White matter	1130 ± 100	47	7	Wright et al. (2008); Cox and Gowland (2010)
ICS	235 ± 10	46 ± 2	2	Silva et al. (2002)
ECS	48 ± 8	6 ± 2	2	Silva et al. (2002)
Myelin water	-	10–50	4.7	Horch et al. (2011)
Myelin proteins and lipids	-	0.05–1	4.7	Horch et al. (2011)

Table 2.1: Values of T_1 and T_2 in healthy, in vivo white matter. B_0 is the magnitude of scanner magnetic field $\mathbf{B_0}$. ICS and ECS denote the intra- and extracellular spaces, respectively.

decay (also known as spin–lattice relaxation). The spins in the transverse plane will gradually lose their phase coherence (dephase) due to slight temporal differences in their resonance frequencies, which change with random fluctuations in the magnetic field experienced by each spin as spins interact with each other, with a time constant T_2 in a process known as T_2 relaxation or decay (also known as spin–spin relaxation). Measurements of the T_1 and T_2 of in vivo white matter are given in Table 2.1.

2.2.4 Signal Decay from Magnetic Field Inhomogeneity

Another significant source of dephasing of spin in the transverse plane is magnetic field inhomogeneity, for example, arising from imperfections in the MR scanner magnet or introduced by the object being imaged. The relaxation time constant associated with this is denoted T_2'. T_2' and T_2 are related to the effective transverse decay T_2^* by

$$\frac{1}{T_2^*} = \frac{1}{T_2} + \frac{1}{T_2'}. \tag{2.7}$$

Although this effect is desirable when measuring local field inhomogeneity, such as in the BOLD effect (Ogawa et al., 1990), often it is an unwanted source of signal loss.

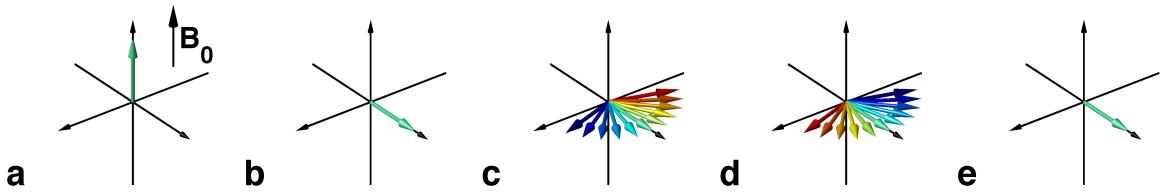


Figure 2.11: Schematic diagram of the formation of a spin echo. **a:** Longitudinal magnetization before the RF pulse is parallel to the static magnetic field $\mathbf{B_0}$. **b:** Magnetization tipped into the transverse plane by a 90° ($\pi/2$) excitation pulse. **c:** Dephased transverse magnetization. **d:** Dephased transverse magnetization after a 180° (π) refocusing pulse is applied at time TE/2. **e:** Refocused transverse magnetization at time TE ("echo").

The next subsection will briefly describe one technique to remove this effect.

2.2.5 Spin Echo

The spin echo pulse sequence was developed to replace the rapid signal reduction from T_2^* relaxation (e.g., in a gradient recalled echo sequence) with the slower reduction from T_2 (Hahn, 1950). This sequence (Fig. 2.11) takes advantage of the fact that the T_2' dephasing is driven by static magnetic field inhomogeneities, which allows this signal loss to be reversed. The reversal is achieved by applying an RF pulse with a flip angle of 180° at an arbitrary time denoted TE/2 after the excitation pulse and waiting until time TE to acquire the MR signal. The 180° pulse is called a refocusing pulse because it causes the accrued phase after the pulse due to field inhomogeneity to be opposite that acquired before the pulse and the transverse spins to coincide ("focus") at time TE. TE stands for echo time, where an echo is the peak in signal when transverse spins are relatively in phase other than at the excitation pulse.

2.2.6 Spatial Encoding

The spatially varying composition of the object being scanned is encoded using three additional magnetic fields. The fields, known as gradients, vary linearly in space along three orthogonal directions and add to the main magnetic field. The strength of the

gradient fields can be manipulated independently with high temporal precision.

One way that gradients are used is to excite only spins in a thin slice. Assuming (with no loss of generality) that the main magnetic field $\mathbf{B_0}$ is along the z-axis and we wish to excite a slice perpendicular to this axis, the z-axis gradient $\mathbf{G_z}$ (with field variation parallel to the bore) would be played. Summing the main and gradient fields gives the resultant net field

$$\mathbf{B} = (B_0 + G_z z)\hat{\mathbf{z}}, \tag{2.8}$$

where B_0 and G_z are the magnitudes of $\mathbf{B_0}$ and $\mathbf{G_z}$, respectively, and $\hat{\mathbf{z}}$ is the unit vector along the z-axis.

The introduced gradient causes spins to have spatially varying excitation frequencies according to Eq. 2.6. Specific spins within a narrow range of z-coordinates can be excited with an RF pulse containing only the frequencies corresponding to that slice. The direction of the gradient used to select the slice is termed the slice selection direction. MR scans that involve exciting a thin slice are referred to as 2D scans. This thesis will concern only 2D scans.

2.2.7 Signal Acquisition

After all the spins have been spatially encoded comes the task of acquiring signal to form an image. The receiver coil(s) pick up a signal modulated (i.e., having a carrier frequency) at the resonance frequency of the excited spins, which reflects the MR-relevant properties of the tissue (e.g., T_1, T_2, etc.). With appropriately timed changes to the magnetic field gradients, this signal can further be manipulated to encode spatial information, enabling us to form an image.

In order to recover spatially encoded information in a 2D scan, gradients perpendicular to the slice selection gradient are played. These gradients impart a relationship

between spatial location and resonance frequency, such that spatial phase patterns are imposed upon the magnetization. As these phase patterns evolve over time, the net signal corresponds to different points in a conceptual frequency domain called k-space (which, when using slice selection, is a 2D plane). The image is given by the Fourier transform of the k-space signal. The coverage of k-space (distance from centre and density of sampled points) determines the spatial resolution and field of view of the final image.

This thesis will concern only gradients that have amplitudes that are trapezoidal functions of time and traverse k-space rectilinearly, i.e., "Cartesian" trajectories. One axis of k-space is known as the frequency encoding (or readout) axis and the other as the phase encoding axis. There are many different techniques to perform such a readout (Bernstein et al., 2004b) and here we describe the two used in this thesis.

2.2.7.1 Single-Line Readout

The single-line readout (also known as "spinwarp" or 2/3DFT) acquires signal from one line of k-space per excitation pulse. It is the slowest MR image acquisition technique, but relatively robust to image artefacts. In this readout,

1. Gradients along the phase encoding and readout axes are briefly played to move to the edge of k-space for the desired line ("pre-phasers"). In general, no signal is acquired during this time (receiver coils are offline).

2. The readout gradient is switched on to a constant amplitude with opposite polarity to the readout pre-phaser. This gradient traverses k-space along the readout axis from one edge of k-space to the other. Signal is received during the entirety of the readout gradient, recording a single line of k-space (Fig. 2.12a).

3. After a period of time TR (repetition time) has passed since the last excitation pulse, steps 1 and 2 repeated with an altered phase encoding pre-phaser gradient

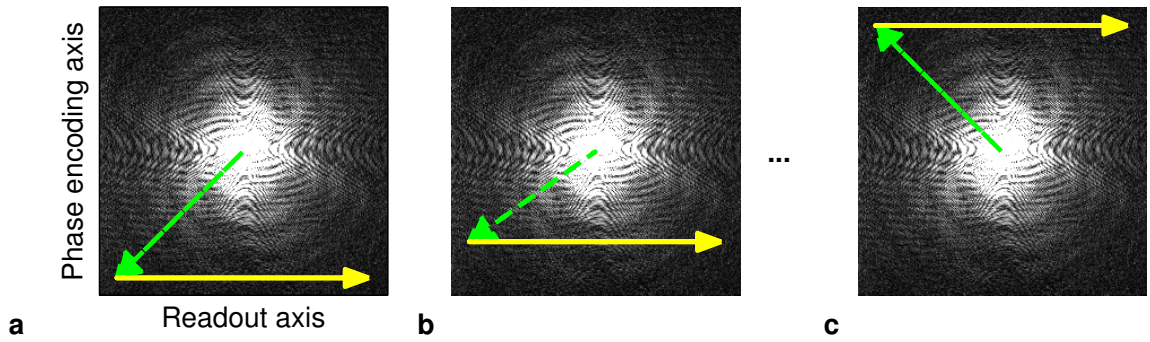


Figure 2.12: k-Space trajectory for the single-line readout showing the showing the trajectories of the pre-phaser (dashed green arrows) and readout (solid yellow arrows) gradients for the (**a**) first, (**b**) second, and (**c**) last lines of k-space acquired. The trajectories in each subfigure follow a separate excitation pulse.

to encode a different line of k-space (Fig. 2.12b). This is repeated until k-space is completely sampled (Fig. 2.12c).

2.2.7.2 Echo-Planar Readout

The echo-planar imaging (EPI) readout (Mansfield, 1977) acquires multiple readout lines in k-space per excitation pulse. This type of readout has the benefit of reduced acquisition time at the expense of more image artefacts such as distortion from magnetic field inhomogeneity (e.g., in areas near the sinuses or ear canals). Typically, all the lines of k-space are acquired after one excitation pulse as follows.

1. Pre-phaser gradients are used as above, with the area required to move to one corner of the desired k-space coverage.

2. The readout gradient is played while the receiver is active, collecting signal from a single line of k-space.

3. The receiver is turned off and the phase encoding gradient is played very briefly ("blipped") with area sufficient to move to the adjacent desired k-space line.

4. The readout gradient is repeated, but with opposite polarity to the previous line such that the next k-space line is acquired in the opposite direction.

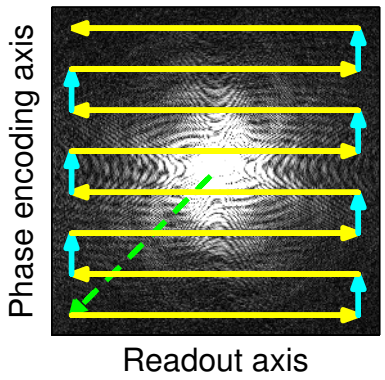


Figure 2.13: k-Space trajectory for the echo-planar readout showing the trajectories for the pre-phaser (dashed green arrow), readout (solid yellow arrows), and phase encoding (solid cyan arrows) gradients.

5. Steps 3 and 4 are repeated until k-space is completely sampled. (Fig. 2.13).

TE is the time in which the origin of k-space is acquired because that is when the average intensity of all spatial frequencies is acquired.

2.2.8 Diffusion Encoding

The gradients can also be used to introduce a relatively large modulation of the spin phase along the direction of the gradient. In this way, the MR signal can be made sensitive to diffusion by adding a specific, spatially varying phase pattern to the transverse component of the spins. The simplest diffusion encoding requires a pair of matched, pulsed gradient fields (Stejskal–Tanner gradients; Ref. Stejskal and Tanner (1965)). This encoding is typically combined with the spin echo sequence to take advantage of the T_2 signal decay and is known as a pulsed gradient spin echo sequence (Fig. 2.14).

The first gradient field $\mathbf{G}$ with magnitude G is played for a duration denoted δ and this imparts additional dephasing (in addition to those described by T_2 dephasing above) to the transverse component of the magnetization. After a period of sensitivity to diffusion called the diffusion time and denoted Δ, a second gradient field of equal amplitude and duration is played, which imposes a rephasing to cancel the first

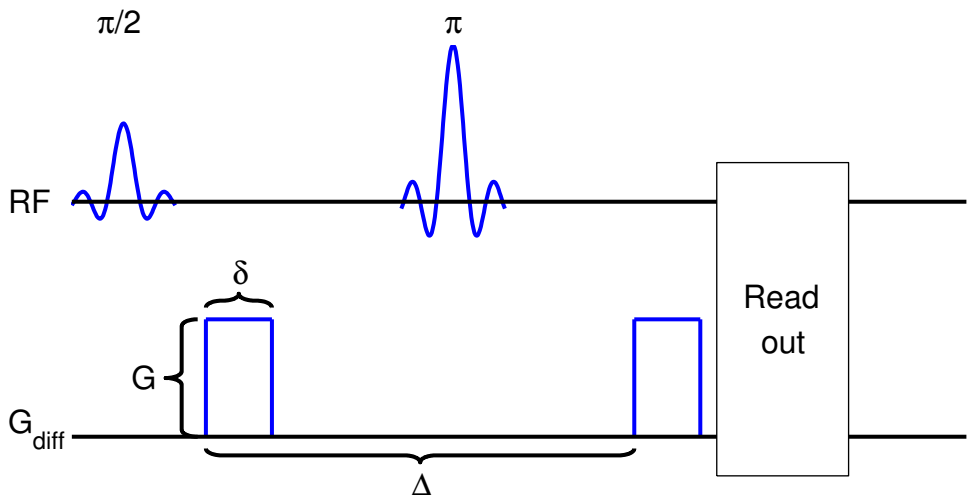


Figure 2.14: Schematic diagram of a pulsed gradient spin echo (PGSE) sequence showing Stejskal–Tanner diffusion gradients G_{diff}.

gradient field. During the period Δ, any random movement of the spins will result in imperfect rephasing and additional signal loss. In areas of free diffusion (e.g., ventricles) or along directions where there is high diffusivity (e.g., parallel to white matter tracts), there will be greater loss and more "diffusion contrast".

The amount of diffusion contrast is quantified by the b factor (Le Bihan et al., 1986) and for the above example is given by (Stejskal and Tanner, 1965)

$$b_{\text{PG}} = (\gamma G \delta)^2 (\Delta - \delta/3), \tag{2.9}$$

where $\delta/3$ corrects the diffusion time Δ for finite gradient lobe durations (Fordham et al., 1996) leading to $\Delta - \delta/3$ being termed the effective diffusion time. The signal attenuation after the gradient pair is given by

$$S = S_0 \exp(-bD), \tag{2.10}$$

where S_0 is the signal with no diffusion gradients applied and D is the (apparent) diffusion coefficient along the direction of the applied gradients. The b value is some-

times described in terms of a $\mathbf{q}$ vector

$$\mathbf{q} = \gamma \mathbf{G} \delta, \tag{2.11}$$

which has a magnitude proportional to the gradient lobe area (strength times duration) and sensitivity to diffusion and is independent of the effective diffusion time $\Delta - \delta/3$.

The total diffusion weighting in a scan actually includes contributions from all the imaging gradients before TE. The expression for the b value that accounts for all gradients until TE is (Le Bihan et al., 1991)

$$b = \gamma^2 \int_0^{\mathrm{TE}} \left[\int_0^t \mathbf{G}(t') dt' \right]^2 dt, \tag{2.12}$$

where $\mathbf{G}(t')$ is the time-varying diffusion gradient. In the case where the system is anisotropic, D is often written as a tensor (i.e., an eigenvalue system with diffusion coefficients along three orthogonal eigenvectors) (Basser et al., 1994a).

2.2.9 Diffusion MR Imaging Artefacts

This subsection will briefly describe some imaging artefacts to diffusion-weighted MR scans using the techniques listed above. More detailed descriptions can be found in Jones and Cercignani (2010).

2.2.9.1 Eddy Current Effects

Signal acquisition requires the manipulation of spin phase using precise phase encoding and readout gradients. However, they can experience interference in the form of previously applied gradient fields that have not yet returned to zero value. Due to the rapid switching of the diffusion-sensitising gradients, eddy currents occur in the wires producing the gradients, which produce additional magnetic fields that counter

the switching of the gradients. Thus, a gradient can persist for longer than intended and add to the image acquisition gradients and distort the image. This is especially detrimental for applications of large gradients such as diffusion encoding. Solutions at scan time include using smaller gradient amplitudes or including more time between the end of the last diffusion gradient and the image acquisition gradients. A post-acquisition solution is to use software, such as *eddy_correct* and *eddy* (Andersson et al., 2012; Andersson and Sotiropoulos, 2014), which are part of the FMRIB Software Library (Smith et al., 2004).

2.2.9.2 Susceptibility Effects

Images acquired using EPI readout are sensitive to magnetic field inhomogeneity. Areas near inhomogeneities will exhibit signal "pileup", a redistribution of the signal in affected voxels to neighbouring voxels. Inhomogeneities arise in areas with differences in magnetic susceptibilities, such as air–tissue interfaces found in the head such as the frontal sinus and the ear canals. These effects can be reversed by acquiring images using at least two unique phase encoding directions (e.g., Anterior $\rightarrow$ Posterior and Posterior $\rightarrow$ Anterior) and additional image processing. One such processing tool is *topup* (Andersson et al., 2003), which is also part of FSL.

2.2.9.3 Bulk and Pulsatile Motion

Over the course of long scans, subjects may move their heads and subsequent image volumes may be mis-registered with earlier ones. If this bulk motion occurs in the midst of k-space acquisition, k-space will be corrupted and the scan should be re-acquired. If it occurs between scans, the scan(s) after the motion can be registered to one(s) before using rigid body transformation tools, such as those already built into *eddy_correct*. Pulsatile motion is expected around large arteries and is largely confined in the brain to the brainstem (Tijssen et al., 2014). Thus, pulsatile motion

is not of concern to the experiments in this thesis.

2.3 Estimating Properties of White Matter with MR

There are many MR techniques to estimate the physical properties of white matter that are relevant to tissue function. This section divides them into diffusion-based and other techniques.

2.3.1 Diffusion-Based

Diffusion-weighted magnetic resonance imaging (DW-MRI) has enormous potential to non-invasively estimate the geometric properties of biological tissues. This remarkable capability is grounded in the sensitivity of the natural motion of water molecules to their microenvironment, which imparts a characteristic change to water diffusion. This altered diffusion provides a signature of the size and shape of the compartments to which it is confined (Tanner and Stejskal, 1968; Cory and Garroway, 1990; Callaghan et al., 1991). For example, in the brain, the diameter of axons in white matter alters the apparent diffusion coefficient of water depending on the time that molecules are allowed to explore the intra-axonal space (Stanisz et al., 1997; Assaf et al., 2008; Barazany et al., 2009; Alexander et al., 2010; Ong and Wehrli, 2010; Avram et al., 2013; Komlosh et al., 2013). With sufficiently accurate models for how this behaviour translates into a detectable change in the DW-MRI signal, one can infer geometric properties of the tissue microstructure. In the context of biological tissues, many of these geometric properties relate to tissue function and health (Johansen-Berg, 2010), making such a technique of great interest as a potential biomarker.

An alternative to this traditional approach of measuring the diffusion displacement

over a range of diffusion times is to consider the spectrum of translational motion of the diffusing molecules. This so-called diffusion spectrum $D(\omega)$ decomposes molecular movement into a range of temporal frequencies ω, resulting in a frequency-dependent diffusion coefficient.[1] Formally, $D(\omega)$ is defined as the Fourier transform of the velocity autocorrelation function $\langle \mathbf{v}(t) \cdot \mathbf{v}(0) \rangle$ of diffusing particles (Stepišnik, 1993). The velocity autocorrelation function describes how long particles continue in their current direction until they change direction or speed, either due to scattering off another particle or encountering a barrier. For a given particle, its velocity over time can be expressed in terms of a weighted sum of velocity at different temporal frequencies (i.e., a Fourier transform of the velocity time course). The diffusion spectrum is the equivalent decomposition of the expected (ensemble average) velocity autocorrelation. Equivalently, the diffusion spectrum is the velocity power spectrum of an ensemble of diffusing particles. This diffusion "power spectrum" relates to the geometry of the environment to which molecules are confined, and thus geometric properties of the environment can be estimated from $D(\omega)$, given an appropriate model.

In free diffusion, the velocity autocorrelation is a delta function at zero time because the particles' velocities will lose correlation instantly (Fig. 2.15, top left). In hindered and restricted diffusion, a small fraction of particles have a negative correlation near $t \approx 0$ due to (assumed) elastic collisions with boundaries (Fig. 2.15, centre and bottom left). Complete knowledge of $D(\omega)$ should contain all the information about moving particles, which in turn should describe the geometry of the environment completely. However, analytic expressions that relate $D(\omega)$ to geometry are complicated and only available for simple geometries (Stepišnik, 1993; Xu et al., 2009). An expression for $D(\omega)$ within impermeable cylinders exists and has been proposed as a model for the intra-axonal diffusion spectrum of white matter (Xu et al., 2009).

[1] The diffusion spectrum should not be confused with the unrelated technique of diffusion spectrum imaging, which aims to estimate the diffusion propagator.

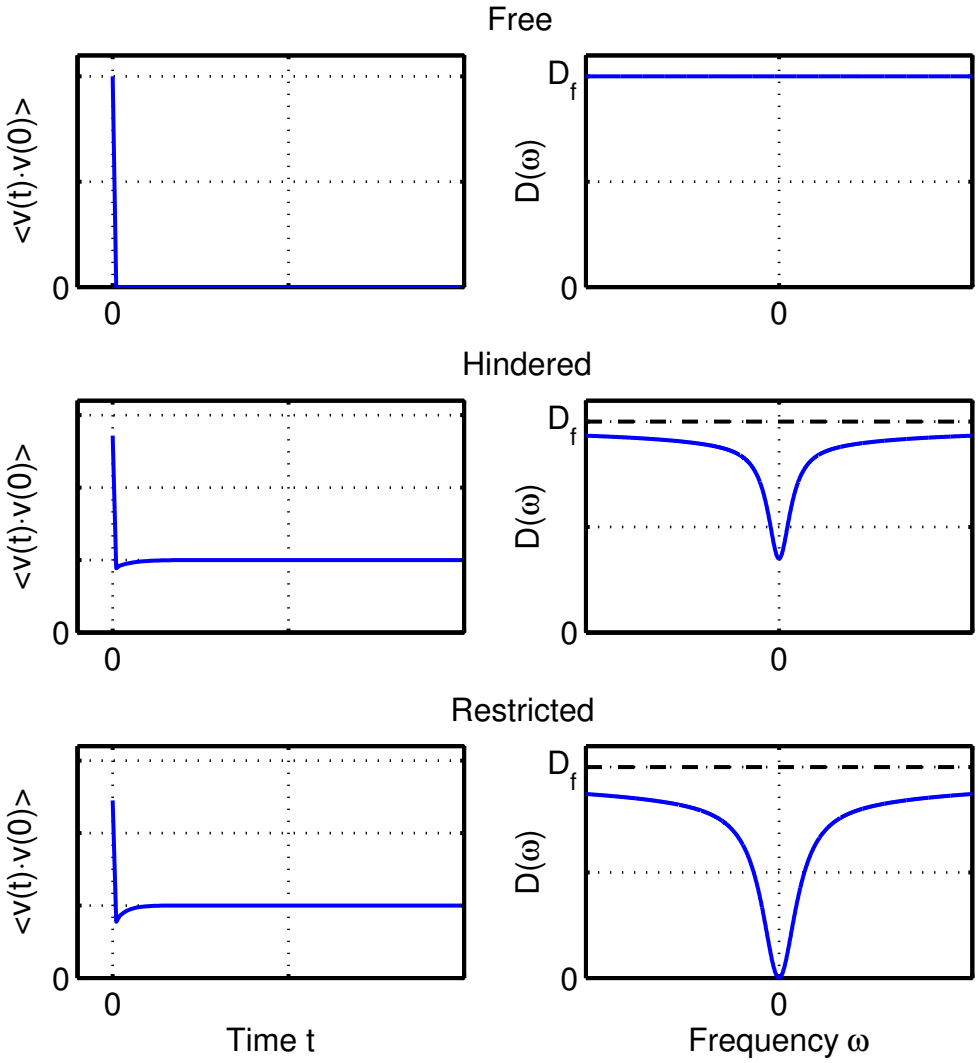


Figure 2.15: Velocity autocorrelation functions $\langle \mathbf{v}(t) \cdot \mathbf{v}(0) \rangle$ and diffusion spectra $D(\omega)$ for free, hindered, and restricted diffusion. In restricted diffusion, $D(\omega)$ is zero because particles must remain within the confining space. The velocity autocorrelation functions and diffusion spectra are related by the Fourier transform.

The spectrum for the interior of an impermeable (restrictive) cylinder approaches $D(\omega) = 0$ at low frequency and asymptotes to $D(\omega) = D_\mathrm{f}$ at high frequency with a sigmoidal transition between these two regimes (Fig. 2.15, bottom right). This behaviour directly follows from the fact that a constant or slowly varying velocity (low frequency) results in a large net displacement. Restrictive spaces like impermeable cylinders thus place limitations on velocity at low frequencies; in particular, $\omega = 0$ corresponds to mean velocity autocorrelation, and any non-zero mean velocity autocorrelation would eventually cause a particle to leave the compartment. Restrictive compartments are thus characterized by $D(\omega = 0) = 0$ and, more generally, a damping of mean velocity at low frequencies.

Unlike restricted geometries, molecules in hindered spaces like the EAS can displace an arbitrary distance given sufficient time. Based on this observation, EAS molecules have been argued to behave like a slower version of free diffusion with a non-zero diffusion coefficient at $\omega = 0$ (i.e., some average velocity; Fig. 2.15, centre right). This reduced diffusion coefficient is dictated by the tortuosity λ, the ratio of free to apparent (hindered) mean diffusion displacements, and in the context of diffusion spectra

$$\lambda = \sqrt{D_\mathrm{f}/D(\omega = 0)}, \tag{2.13}$$

This property holds at $\omega = 0$ by definition since a net displacement is associated with zero frequency. Although the diffusion spectrum of hindering geometries is known not to be spectrally flat (Stepišnik et al., 2001; Parsons et al., 2006), some previous models (Xu et al., 2009) have further assumed that this value holds at all frequencies resulting in a flat spectrum that is similar to free diffusion, but with a reduced diffusion coefficient.

Measurements of the diffusion spectrum require the use of oscillating gradients,

rather than the more conventional pair of gradient pulses (Stejskal and Tanner, 1965). These oscillating gradients cause a given water molecule to accrue a large positive (or negative) phase offset if a significant component of motion of the molecule along the direction of the gradient is positively (or negatively) correlated with the gradient waveform. Molecular motion at other frequencies will be orthogonal to the gradient waveform,[2] resulting in negligible phase offsets and making the MR signal insensitive to this motion. An ensemble of molecules, each with random phase offset at a given frequency, will thus accrue a distribution of phase offsets. This will in general lead to signal loss (similar to conventional diffusion weighting) and, under some circumstances, a coherent phase offset (de Swiet and Sen, 1994; Liu et al., 2004; Özarslan et al., 2008). Oscillating gradient measurements have been demonstrated for both in vivo (Does et al., 2003; Colvin et al., 2011; Van et al., 2014; Baron and Beaulieu, 2014) and ex vivo (Portnoy et al., 2012; Aggarwal et al., 2012) brain tissue. Most in vivo measurements have been made on pre-clinical scanners due to the difficulty of achieving sufficient diffusion weighting using clinical scanners (Gore et al., 2010).

2.3.1.1 Pulsed Gradient Spin Echo

The pulsed gradient spin echo (PGSE) technique was described in Section 2.2.8 above. It is the simplest diffusion sequence that allows explicit control of the diffusion sensitivity q (the magnitude of $\mathbf{q}$) and diffusion time Δ. The simplest models measure the ADC using one q and Δ value in multiple directions to compute an ADC tensor (Basser et al., 1994b). This has been used to infer the principle axon direction and fractional anisotropy in imaging voxels. However, for voxels with more than one nerve fibre, a single tensor gives insufficient flexibility to estimate the direction of each fibre. To estimate multiple fibre directions, multiple tensors (Tuch et al., 2002), cylinders (Assaf et al., 2004), and sticks (Behrens et al., 2007) have been proposed. More

[2] Approximately orthogonal for finite waveforms.

details for modelling multiple fibres can be found in literature (Alexander, 2005).

There is a technique known as q-space imaging (Callaghan et al., 1988), which can describe the directional hindrances to diffusion experienced by particles and thus also inform about the geometry of the microenvironment. This method estimates the diffusion propagator, which describes the conditional probability of a particle diffusing to any point in space in a time Δ and can be calculated from the Fourier transform of the diffusion attenuation vector given sufficient ADC measurements over a range of q values. However, this method is time consuming and requires large q values beyond those achievable with a clinical MR scanner (Ong and Wehrli, 2010).

There are techniques that aim, not to describe the shape of the microenvironment, but the populations of spins in intra- and extracellular compartments through models that describe the time-dependent population of spins. Some models characterize the residence times (Quirk et al., 2003; Meier et al., 2003; Lätt et al., 2009; Fieremans et al., 2010) of spins. Others describe the exchange using rate constants, which are related to membrane permeability (Stanisz et al., 1997). This technique has seen only limited use using clinical MR scanners possibly due to the higher b or Δ values required to estimate the model parameters.

The PGSE sequence, when used with high b values, has shown biexponential signal decay (Niendorf et al., 1996) with b and this has been interpreted in multiple ways. This has been claimed as evidence for fast and slow diffusion pools of water (Assaf and Cohen, 1998; Mulkern et al., 1999; Clark and Le Bihan, 2000), where the slow pool represents water molecules that are bound to membranes and other large molecules. There is more direct evidence of this from diffusion measurements that show the disappearance of one pool as tissue freezes (Dhital et al., 2011). A counterclaim explains this behaviour as arising from cells with a distribution of diameters, but the same diffusivity within each (Sehy et al., 2002; Yablonskiy et al., 2003). Both claims are plausible and both effects could occur simultaneously. Another proposed

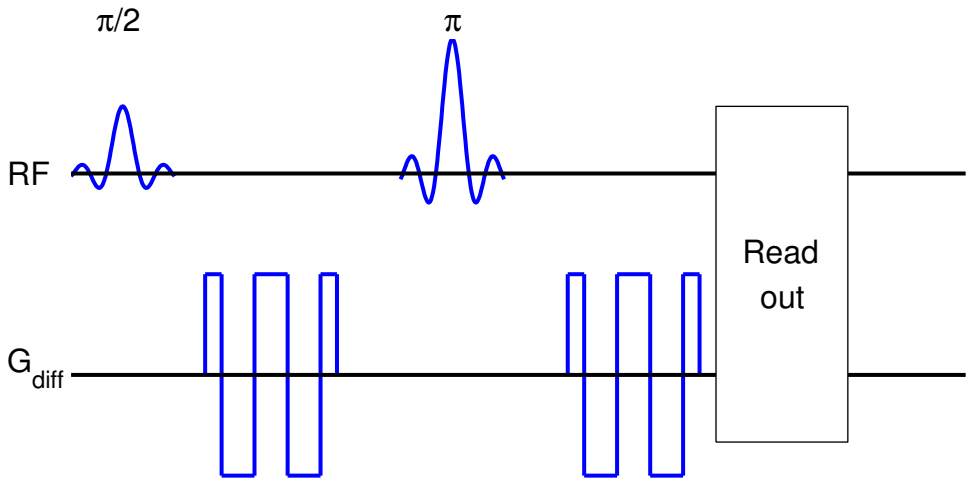


Figure 2.16: Schematic diagram of an oscillating gradient spin echo (OGSE) sequence with trapezoid-modulated cosine diffusion gradients G_{diff}, each with two cycles.

explanation is that the fast diffusion pool represents ICS water and the slow represents ECS. However, the measured volume fraction of the slow diffusion pool of 0.31 ± 0.04 in in vivo human white matter (Maier et al., 2001) does not support this.

2.3.1.2 Oscillating Gradient Spin Echo

The oscillating gradient spin echo (OGSE) technique takes advantage of the fact that the translational motion of diffusing particles can be described using a Fourier basis, which adds a degree of freedom compared to PGSE when describing particle motion. To measure $D(\omega)$ at a given frequency, the diffusion gradient lobes are cycled repeatedly between positive and negative amplitudes at the desired frequency along a given diffusion encoding direction in place of the single lobes in PGSE (Fig. 2.16).

The oscillating gradients define a spectral sampling function that weights a measurement of the diffusion spectrum (Stepišnik, 1993). The details of the gradient waveform (e.g., sine or cosine phase, sinusoidal or trapezoidal shape, the spacing between the two waveforms, etc.) define properties of the sampling function such as the primary frequency or frequencies sampled, sampling width, and magnitude of side

lobes. The sampling function is given by

$$\mathbf{F}(\omega) = \gamma \int_{-\infty}^{\infty} \int_{0}^{t} \mathbf{G}(t')dt' \exp(-i\omega t)dt. \tag{2.14}$$

The OGSE signal is given by

$$S = S_0 \exp\left[-\frac{1}{\pi}\int_{0}^{\infty} \mathbf{F}(\omega)\mathbf{D}(\omega)\mathbf{F}(-\omega)d\omega\right], \tag{2.15}$$

where $\mathbf{D}(\omega)$ is the diffusion spectrum tensor. The gradients in PGSE sequences can also be analysed from the diffusion spectrum sampling function viewpoint. They sample about zero frequency with a width that is inversely related to diffusion time. However, the sampled frequencies are not sufficiently high to measure the shape of $D(\omega)$ for white matter. $|\mathbf{F}(\omega)|^2$ for pulsed gradients and trapezoid-modulated sine and cosine gradients are shown in Fig. 2.17.

2.3.1.3 Multiple-Pulsed Field Gradient

MR pulse sequences consisting of two or more sets of pulsed diffusion gradients, where each set can have a unique direction and be separated from the last by a mixing time, can provide more information that a single set of pulsed gradients (Mitra, 1995). Such information includes descriptions of the following types of microscopic restricted compartments: isotropic restrictions and randomly oriented and aligned anisotropic restrictions (Özarslan, 2009) or apparent exchange rate between slow and fast diffusing pools of water (Lasič et al., 2011).

2.3.2 Non-Diffusion-Based

The severe implications and prevalence of dys- and demyelinating disease has led to great interest in techniques that can image myelin non-invasively (Laule et al., 2007). However, myelin contributes relatively little to diffusion-weighted signal in

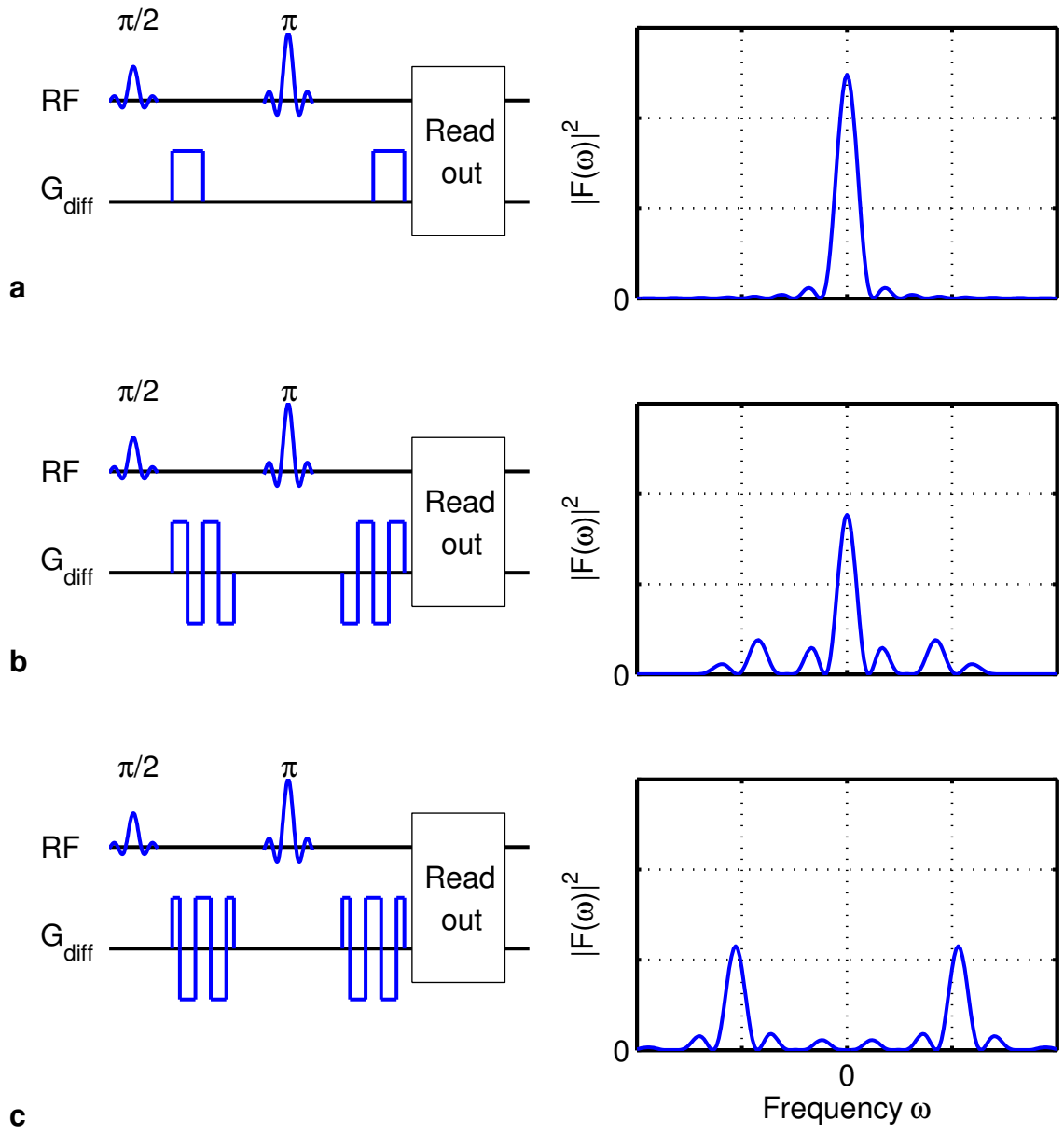


Figure 2.17: Schematic diagrams of a (**a**) PGSE, (**b**) trapezoid-modulated sine OGSE, and (**c**) trapezoid-modulated cosine OGSE sequences, each with the same b value, and their corresponding $|\mathbf{F}(\omega)|^2$ (all have the same scale). Sine OGSE is rarely used because it samples at both $\omega \approx 0$ (dominantly) and the frequency of the sinusoid. Measuring at two frequencies can be confounding and "wastes" the energy of the sampling function about $\omega \approx 0$, which can be accesses using PGSE. Increasing the number of oscillations will decrease the magnitude of the side lobes.

practice (Beaulieu and Allen, 1994). The techniques presented below focus on the measurement of myelin.

2.3.2.1 Quantitative T_2

Myelin has short T_2 (Table 2.1) and this can distinguish it from the intra- and extra-axonal spaces. Several techniques (Horch et al., 2011; Du et al., 2013) aim to estimate multiple T_2 values from within a single voxel, such that the amount of signal from each T_2 reflects its volume contribution and thus the fraction of the voxel that is myelin versus other tissue.

2.3.2.2 Magnetization Transfer

Magnetization transfer is a family of techniques whereby ^{1}H in a semi-solid, such as the cell membrane, is excited (at a different resonance frequency from that of water). Membrane-bound protons excited in such a manner can transfer their excitation to water protons, leading to a selective saturation of water molecules that are in exchange with membranes (Wolff and Balaban, 1989). This technique can be used to detect myelin water (water between layers of myelin rolled around an axon), where the MR effect is nine times stronger than in intra- and extra-axonal water (Stanisz et al., 1999).

2.3.2.3 T_1/T_2 Ratio

A technique that appears to image myelin using the ratio of T_1- to T_2-weighted images has been recently proposed (Glasser and Van Essen, 2011). The mechanism behind the apparent myelin contrast is unclear as myelin has a shorter T_2 than the echo time of the imaging sequence and should not give rise to any signal. Further investigation is warranted as the benefits of imaging myelin using clinical MR hardware are potentially valuable.

Chapter 3

A Model for Extra-Axonal Diffusion Spectra

3.1 Introduction

Microstructural characterization of tissue typically begins by assuming some simple geometry for which the diffusion spectrum has been derived and relating this to the DW-MRI signal in an oscillating gradient experiment. In the brain, cylinders are often used to model axons (Ford and Hackney, 1997; Hwang et al., 2003; Assaf et al., 2004). This is typically combined with a second compartment intended to account for the extra-axonal space (EAS). The diffusion spectrum of the EAS is known not to be spectrally flat (Stepišnik et al., 2001; Parsons et al., 2006) owing to the tortuous nature of the EAS (Nicholson and Syková, 1998). This has also been observed in non-oscillating gradient experiments (Shemesh et al., 2011). However, in certain models, the EAS diffusion spectrum has been approximated as a constant over all frequencies, which is only true for free diffusion, but using the lower apparent diffusion coefficient found about $\omega \approx 0$ (i.e., diffusion is slow, but the spectrum has no shape) (Xu et al., 2009). This approximation is valid at low frequencies, but will likely lead to biases

in fitting geometric parameters such as restricted volume fraction or axon diameter at higher frequencies, as will be demonstrated here through simulations.

The goal of the current work is to propose a model for the diffusion spectrum in the EAS with improved accuracy that may yield white matter microstructural information. Models of the intra-axonal space typically assume that water molecules strictly remain inside axonal cylinders over the time scale of a measurement ("restricted" diffusion). By comparison, an EAS model must describe a more complicated geometry outside tightly packed axons in which water molecules will tend to remain in the confining space between axons where they are at the beginning of a measurement, but will occasionally diffuse outside to an adjacent space. Closed-form solutions are unlikely to describe such complicated geometries, particularly biological systems with a distribution of confining space sizes and random packing. Instead, the proposed EAS model aims to retain much of the simplicity of previous work by considering the behaviour of EAS spins impinging on axons to be approximated by restricted diffusion, while encapsulating the behaviour of spins diffusing unhindered by axons with a component that is spectrally flat. This hybrid approach can be considered as a kind of temporal exchange model in which water molecules move between regimes of restriction and free diffusion and can be compared to the multi-pore diffusion diffraction pattern work of Callaghan et al. (1991). Versions of the model are presented for both periodically packed cylinders of uniform radius and randomly packed cylinders with a distribution of radii. The accuracy of these models is assessed through comparison with Monte Carlo simulations of these geometries at a range of spatial scales, demonstrating good agreement despite the simplified nature of this model. This work has been described previously in a manuscript published in *Magnetic Resonance in Medicine* (Lam et al., 2015).

3.2 Theory

In this section, we present a conceptual framework for the diffusion spectrum in the EAS. We begin with a description of the properties of the diffusion spectrum and then present simulations of diffusion in the EAS. Next, we build on this to present a new model for the EAS that aims to strike a balance between simplicity and explanatory power.

3.2.1 The Diffusion Spectrum

The diffusion spectrum $D(\omega)$ is the Fourier transform of the particles' average velocity autocorrelation; that is, the power spectrum of particle velocities. In the absence of barriers, diffusion is free and is driven simply by the scattering of molecules with each other. For example, the velocity autocorrelation for free diffusion is effectively instantaneous de-correlation (a delta function), which Fourier transforms to a constant diffusion spectrum.

This default shape of the diffusion spectrum is altered by the presence of any barriers that impede movement. This general property holds for both confining spaces from which particles cannot escape (restricted diffusion) and porous microstructure with communicating spaces (hindered diffusion). The primary difference between restriction and hindrance is that the latter enables molecules to displace an infinite distance given infinite time, although displacement rates are slower than for free diffusion.

As we will see, confining spaces (whether restrictive or hindering) correspond to a reduction of the apparent diffusion coefficient at low frequencies, while high frequencies are less affected. In restricting geometries, particles must have $D(\omega = 0) = 0$ in order for particles to remain inside the confining space; for hindering geometries, the diffusion spectrum is reduced, but non-zero, at $\omega = 0$. Reduced diffusion un-

der hindrance is often characterized by tortuosity, defined by the ratio of free and apparent diffusion coefficient at $\omega = 0$ (Eq. 2.13; Stepišnik et al. (2001)).

This leads to the general property that, in the presence of restricting or hindering barriers, the diffusion spectrum transitions from free diffusion behaviour at high frequencies ($D(\omega \to \infty) = D_{\mathrm{f}}$), the free diffusion coefficient) to reduced diffusion at low frequencies. The transition from $D(\omega = 0)$ to D_{f} is well studied for pure restriction, resulting in a known relationship between the length scale of the restrictions and the specific shape of the diffusion spectrum (Stepišnik, 1993; Xu et al., 2009). In contrast, the shape of the diffusion spectrum has received less attention for hindered geometries, which are more complicated and less suited to closed-form calculations.

3.2.2 Preliminary Simulations

Throughout this work, Monte Carlo simulations are used as a ground truth to establish the properties of the diffusion spectrum of water in the space surrounding different geometric configurations of cylinders representing the EAS. We present simulated geometries that range from regular lattices of cylinders with uniform radii to random packings with a distribution of radii. The full details of these can be found in the Monte Carlo simulations subsection. In the current section, we consider a preliminary set of simulations of the EAS to demonstrate the characteristic features of this space and motivate the EAS model that follows. The diffusion spectra for the intra- and extra-cylinder spaces of a simple square packing geometry are shown in Fig. 3.1.

Our Monte Carlo simulations (described in detail below) demonstrate that the EAS spectrum has a shape similar to the spectrum for an impermeable cylinder (intra-axonal), but with an elevated baseline. While diffusion for restrictive and hindering geometries deviates at low frequencies, they are observed to be convergent at high frequency. Diffusion at high frequency has been related to the surface-to-volume

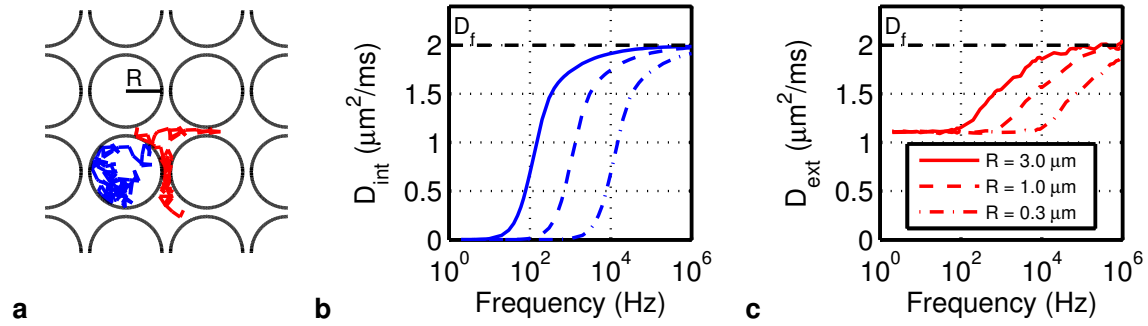


Figure 3.1: a: Square packed axons idealized as cylinders (axial view) of radius R with representative paths of diffusing intra- (blue) and extra-cylinder (red) particles. The corresponding diffusion spectra for the (**b**) intra- and (**c**) extra-cylinder spaces for three different cylinder radii (with a cylinder centre-to-centre separation to diameter ratio of 1.12). D_f is the free diffusion coefficient.

ratio S/V of the environment (Novikov and Kiselev, 2011). This property is similar to that of short diffusion time, pulsed-gradient measurements: for short diffusion time (or high oscillation frequencies), only molecules a very short distance from a reflecting surface experience altered diffusion behaviour, while all other molecules in the volume experience free diffusion.

The diffusion spectrum for a hindering extra-cylinder space, which is a compelling model for extra-axonal microstructure, to date remains impartially described. Previous models of the EAS spectrum are accurate for low (Stepišnik et al., 2001) and high (Novikov and Kiselev, 2011) frequency asymptotes. The transition between these extremes is the subject of the present work, which aims to present a simple model that approximates the entire spectrum.

3.2.3 Basic Exchange Model

The observed shape of the EAS spectrum shown in Fig. 3.1c is perhaps not surprising given what we know of the space between cylinders. For cylinders that are completely abutting, the EAS water is trapped in restrictive "pores", much like the water inside impermeable cylinders. For looser cylindrical packing (reduced tortuosity), gaps ap-

pear through which water can communicate between pores. The majority of the pore perimeter will be constituted by the cylinder walls and a minority by the gap between cylinders. Thus, EAS water will still tend to remain trapped in the pores, but will also occasionally diffuse between them. Thus, depending on the packing (tortuosity), water molecules can be considered to spend a variable fraction of their time behaving as restricted (trapped in pores) or free (moving between pores).

This description is at the heart of our proposed model, which expresses the EAS diffusion spectrum as a combination of free and restricted diffusion:

$$D_{\text{ext}}(\omega) = f_{\text{f}} D_{\text{f}} + (1 - f_{\text{f}}) D_{\text{r}}(\omega), \tag{3.1}$$

where f_{f} represents the fraction of the time a given particle is "free" (moving between pores), while for the remainder of time the particle is "restricted" to a pore.[1] The model assumes that, as molecules migrate between pores, during the migration period they are characterized by a flat spectrum and at all other times by a restricted spectrum. We can thus consider this to be a type of exchange model, in which a given molecule exchanges between different regimes of behaviour (rather than physical compartments).

The Kärger model (Kärger, 1969) is a two-compartment exchange model to which our model can be compared. This model assumes two compartments with unique diffusion coefficients and particle residence times in each. The signal attenuation from diffusion is derived from calculated apparent diffusion coefficients, which are based on the actual diffusion coefficients, particle residence times, and volume fractions of each compartment. The form of Eq. 3.1 is identical to that of the Kärger model for the case where particles show rapid exchange between the compartments, known as the fast exchange limit (FXL; Lee and Springer (2003)).

[1] Alternatively, f_{f} is the fraction of particles in the free regime, calling on the equivalence of long-time behaviour with ensemble behaviour; however, we prefer the temporal picture here since it can be more intuitively related to the microstructure, as we will see.

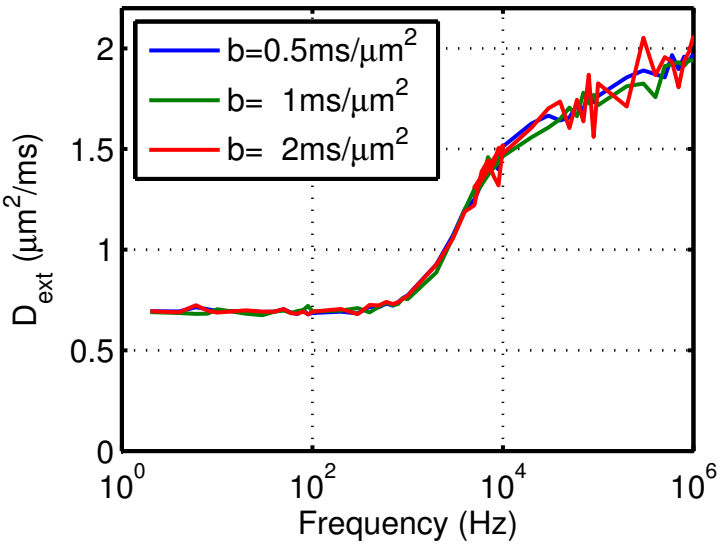


Figure 3.2: Simulated $D_{\text{ext}}(\omega)$ for the extra-cylinder space with $b = 0.5$, 1, and 2 ms/μm^2 (with a cylinder radius of 1 μm, a cylinder centre-to-centre separation to diameter ratio of 1.03, and $D_{\text{f}} = 2$ μm^2/ms). The number of particles was the same in all simulations and was optimized for the $b = 1$ ms/μm^2 case. It is slightly suboptimal for the $b = 2$ ms/μm^2 case where the plot shows increased noise.

Order of magnitude calculations indicate the simulated measurements are indeed in the FXL. Calculations in Appendix 3.A support the FXL assumption. Further, simulations of spins in the EAS around cylinders with $b = 0.5$, 1, and 2 ms/μm^2 yield the same diffusion spectrum (Fig. 3.2), reinforcing that the system is in the FXL (confirmed for both square and random cylinder packings).

We are now ready to consider the form that the restricted and free components of Eq. 3.1 should take. Given that $D_{\text{r}}(0) = 0$, we can combine Eqs. 2.13 and 3.1 to determine that

$$f_{\text{f}} = 1/\lambda^2 \tag{3.2}$$

This states that the more tortuous the EAS (large λ), the less time molecules spend freely diffusing between pores.

The form that the restricted component should take is less obvious given the com-

plicated geometry of the EAS (i.e., the space between cylinders shown in Fig. 3.1a). One useful analysis is to isolate the restricted component by subtracting $f_{\mathrm{f}} D_{\mathrm{f}}$ from a simulated EAS spectrum (Fig. 3.3a). It is clear that the shape of the restricted spectrum is similar to that of an impermeable cylinder $D_{\mathrm{r}}(\omega)$ given by (Stepišnik, 1993)

$$D_{\mathrm{r}}(\omega) = \sum_k B_k \frac{a_k D_{\mathrm{f}} \omega^2}{(a_k D_{\mathrm{f}})^2 + \omega^2}, \tag{3.3}$$

where

$$B_k = \frac{2\left(R/\mu_k\right)^2}{\mu_k^2 - 1}, \tag{3.4}$$

$$a_k = \left(\mu_k / R\right)^2, \tag{3.5}$$

μ_k is the k^{th} root of $J_1'(\mu) = 0$, and J_1 is a Bessel function of the first kind. In fact, comparing the spectrum of the EAS to that of a cylinder with the same total volume as the EAS gives a surprisingly reasonable prediction (dashed green line) of $D_{\mathrm{r}}(\omega)$.

However, this simple model for the restricted component (a cylinder of matched volume) does deviate significantly from the simulated spectrum in the transition region. Were we to use this model, we would expect a significant bias in any fit to data. Comparing simulated $D(\omega)$ to those calculated analytically for spins within impermeable cylinders at a range of radii (not shown), it is clear that no single radius accurately captures the shape of the restricted component of the EAS spectrum in the transition region. In particular, the EAS spectrum approaches the D_{f} asymptote more slowly than $D(\omega)$ for spins within the impermeable cylinder. This difference is likely due to the deviation of the shape of the EAS from a cylinder. While one might hope to derive a complicated expression for the geometry external to uniformly

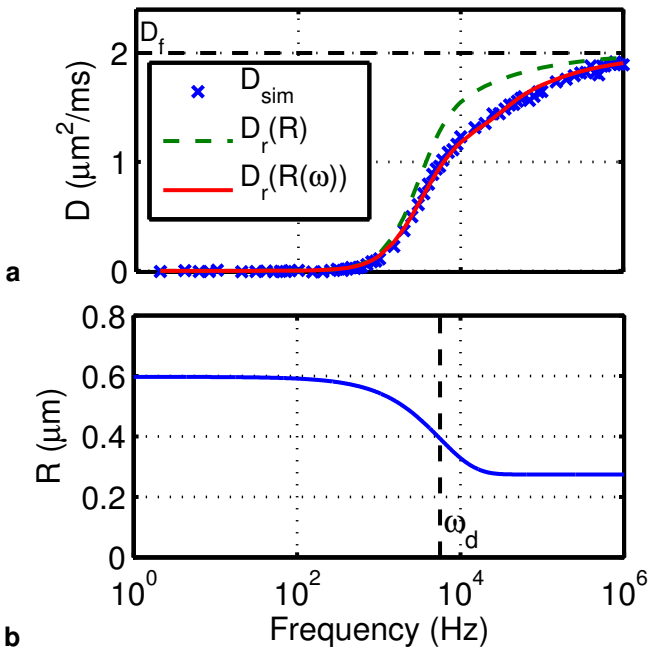


Figure 3.3: a: The "restricted component" of a simulated EAS spectrum ($\times$) calculated by subtracting $f_\mathrm{f} D_\mathrm{f}$ from the EAS spectrum of square packed cylinders. Overlaid are the diffusion spectra of a cylinder of radius R (dashed green line) calculated to yield the same volume as the EAS and that of the proposed variable radius model (solid red line). **b:** The variable radius corresponding to $R(\omega)$ in a. ω_d is defined in Eq. 3.7.

packed abutting cylinders, such a model would further need to capture the change in geometry with looser packing to be useful. We instead take the approach of extending the cylinder model, which has the benefit of both simplicity and similarity to the EAS.

3.2.4 Improved Exchange Model with Variable Radius

The agreement of the model with the simulated spectrum can be improved by allowing the radius of the cylinder to vary with frequency according to

$$R(\omega) = (R_0 - R_\infty)e^{-\omega/\omega_\mathrm{d}} + R_\infty \tag{3.6}$$

$$\omega_\mathrm{d} = 2\pi\frac{2D_\mathrm{f}}{R_0^2}, \tag{3.7}$$

in which R_0 and R_∞ are the radii at $\omega = 0$ and $\omega = \infty$, respectively, and ω_d describes an exponential rate of decay between the two values. The expression for ω_d is adapted from the equation for mean diffusion displacement (Eq. 2.1). That is, $2\pi/\omega_\mathrm{d}$ corresponds to the diffusion time, which is the time required for one standard deviation of diffusing particles to displace by $x = R_0$. At $\omega \ll \omega_\mathrm{d}$, particles have diffusion displacements consistent with those within a cylinder of radius R_0. At $\omega \approx \omega_\mathrm{d}$, particles have displacements consistent with those within a cylinder with a radius between R_0 and R_∞.

The improvement in model agreement is demonstrated in Fig. 3.3a (solid red line), suggesting that the EAS can be described by a restrictive component with an effective radius that depends on frequency. The dependence of R on frequency is plotted in Fig. 3.3b.

To model the EAS diffusion spectrum for randomly packed cylinders, we consider R_0 to be a distribution and perform a weighted sum of the diffusion signal attenuation

of each pore to yield the total diffusion signal attenuation:

$$E_{\text{ext}}(\omega) = \int A(R_0) \exp\{-b[f_{\text{f}} D_{\text{f}} + (1 - f_{\text{f}}) D_{\text{r}}(R_0, \omega)]\} dR_0 \tag{3.8}$$

$$A(R_0) = \frac{F_{\text{ext}}(R_0) R_0^2}{\int R_0^2 dR_0}, \tag{3.9}$$

where $F_{\text{ext}}(R_0)$ is the distribution of R_0 and b is the diffusion weighting. Note again that completely parallel cylinders are assumed. In the case of any orientation distribution, this equation will need to be modified to account for the projections along the gradient direction. We can then convert to an effective diffusion spectrum for all the pores:

$$D_{\text{ext}}(\omega) = -\frac{1}{b} \ln(E_{\text{ext}}(\omega)). \tag{3.10}$$

As will be demonstrated in the Results section, Eqs. 3.1–3.10 closely match the simulated $D_{\text{ext}}(\omega)$ for regularly and randomly packed cylinders.

3.2.5 Interpretation of Model

For square and hexagonally packed uniform cylinders and randomly packed cylinders with a gamma distribution of radii, we empirically found the following relations to agree with all simulated spectra across a wide range of cylinder sizes and packing densities and configurations (i.e., square, hexagonal, and random) as will be shown in the Results section.

$$R_0 = R_{\text{pore}} \left(1 - \frac{1}{\lambda^2}\right) p^2 \tag{3.11}$$

$$R_\infty = 3(S/V)^{-1} \left(1 - \frac{1}{\lambda}\right) p, \tag{3.12}$$

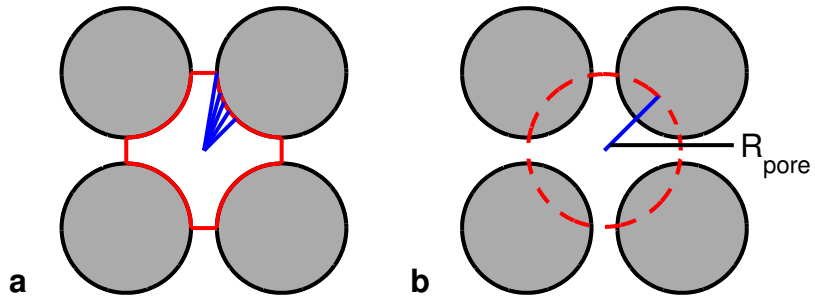


Figure 3.4: a: Square packed axons idealized as cylinders (axial view) with one pore outlined in red. The mean distance from the pore centroid to axon walls (indicated by blue lines) is R_{pore}. **b:** The same axons with a circle (dashed red line) of radius R_{pore}, which represents the restricted component of the EAS model. Note that the restricted component is not a physical compartment.

where the effective pore radius R_{pore} is the mean distance between the centre of the pore and the walls of the cylinders (Fig. 3.4) and p is the fractional separation between adjacent cylinders.[2] R_{pore} is likely related to the cylinder radii, but this will be examined in Chapter 4. We define the fractional separation as

$$p = \sqrt{f_{\text{int,max}}/f_{\text{int}}}, \tag{3.13}$$

where $f_{\text{int,max}}$ is the maximum cylinder volume fraction for a set of cylinders with a given radius distribution and packing type (e.g., square, hexagonal, and random) and f_{int} is the cylinder volume fraction.

$p \geq 1$ in general with $p = 1$ for abutting cylinders. $f_{\text{int,max}}$ is $\pi/4 \approx 0.7854$ for square packed uniform cylinders; $\pi/(2\sqrt{3}) \approx 0.9069$ for hexagonally packed uniform cylinders; and can be determined numerically for randomly packed cylinders with a distribution of radii (≈ 0.8433 for the distribution used in this work). For the

[2]When cylinders are abutting, $R_0 = R_{\text{pore}}$ and $R_\infty = 3(S/V)^{-1}$. The former logically relates to the area between the cylinders, which is covered by spins given a long time to diffuse. The latter bears some explanation. R_∞ relates to the pore surface-to-volume ratio as spins have a short time to diffuse. Hypothetically modelling the EAS as infinite cylinders of radius R yields $S/V = (2\pi R)/(\pi R^2) = 2/R$. A factor of 3 instead of 2 was found to match the simulated data better. This corresponds to modelling the EAS as a sphere of radius R, but there is no obvious reason why this should be so. The remaining factors in Eqs. 3.11–3.12 are purely empirical, although it is logical that both R_0 and R_∞ should vary somehow with fractional cylinder separation p.

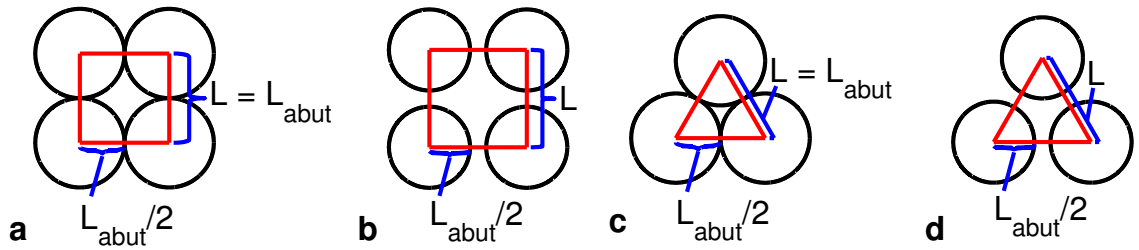


Figure 3.5: Axial view of (**a**) abutting and (**b**) non-abutting square packed cylinders with centre-to-centre separation L and abutting centre-to-centre separation L_{abut} labelled. **c, d:** As a and b, but for hexagonally packed cylinders.

two cases of regular packing, p is also equivalent to the ratio of cylinder centre-to-centre separation to cylinder diameter, which we denote as L and L_{abut}, respectively (Fig. 3.5). L and L_{abut} are not defined for randomly packed cylinders. λ and p are not independent. They both depend on f_{int}; however, it is not trivial to explicitly write λ as a function of f_{int} as the form of λ depends on the packing arrangement (e.g., square, hexagonal, random, etc.)

The behaviour of the model parameters (normalized by a factor R_{min} proportional to the size of the EAS) and their subfactors as a function of p is plotted in Fig. 3.6. R_{min} is the radius of a cylinder with the same volume as the EAS volume for abutting cylinders (Fig. 3.7). The remainder of this section gives a qualitative explanation of Eqs. 3.11 and 3.12.

The R_0 parameter represents the effective radius of the restricted component when particles have had sufficient time to thoroughly sample the EAS (at low frequencies). When the cylinders are abutting, $R_0 = R_{\text{pore}}$. When the cylinders are slightly non-abutting, R_{pore} overestimates R_0 because particles within the narrow "gaps" between cylinders experience a more restricted space. However, as the gap between adjacent cylinders becomes greater, these gaps decrease in significance and the value of R_0 becomes increasingly driven by R_{pore}. This transition occurs at the value of p where R_0 for non-abutting and abutting cylinders are equal, which we denote as p_0 (Fig. 3.8). Indeed, for square and hexagonally packed cylinders, p_0 corresponds within 6% to

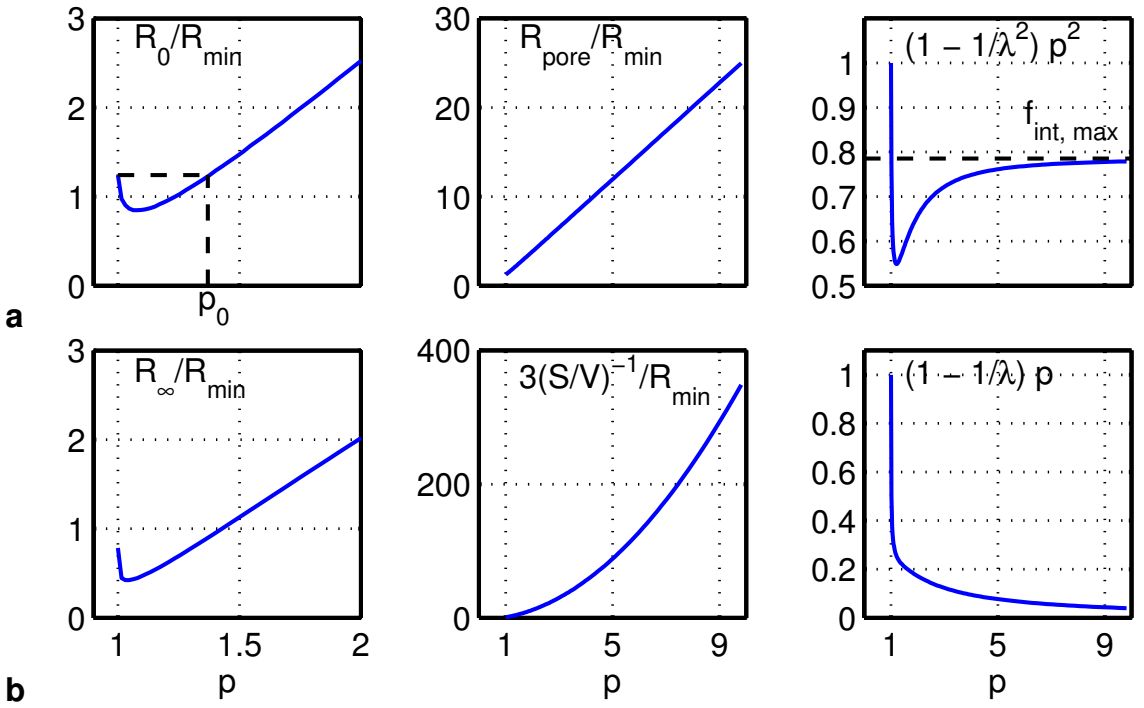


Figure 3.6: Plots of the model parameters (**a**) R_0 and (**b**) R_∞ and their subfactors (normalized to $R_{\min}$, an equivalent radius for the EAS area for abutting cylinders – see Fig. 3.7) as a function of fractional separation p for square packed cylinders of the same size. The value of p (denoted p_0), when R_0 for abutting ($p = 1$) and non-abutting ($p > 1$) cylinders are equal, and the abutting cylinder volume fraction $f_{\text{int,max}}$ are indicated. The curves for hexagonal packing (not shown) are similar.

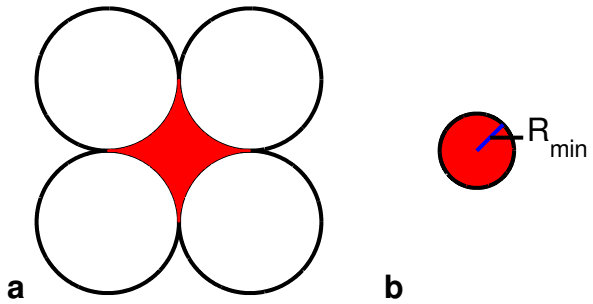


Figure 3.7: **a:** Abutting square packed axons idealized as cylinders (axial view) with the pore area shaded in red. **b:** A circle with the same area and radius $R_{\min}$.

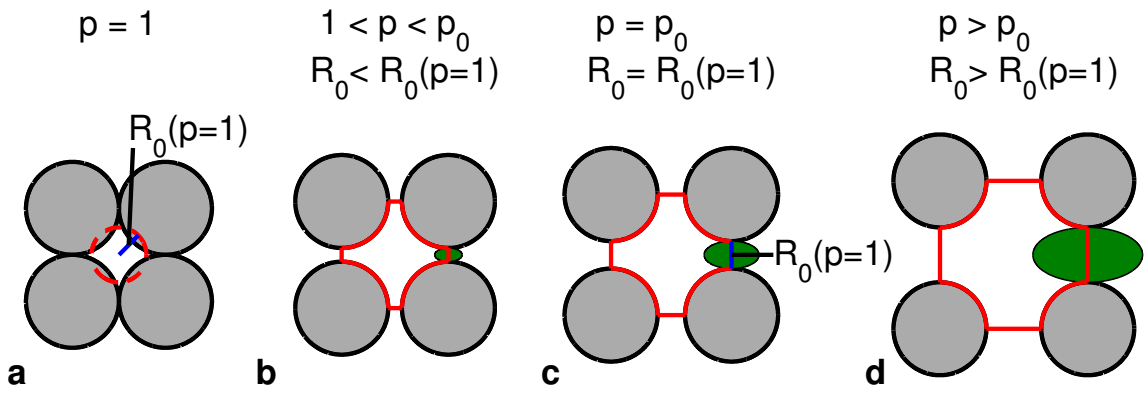


Figure 3.8: This figure explains why R_0 is less than $R_0(p = 1)$ when $1 < p < p_0$ and greater than $R_0(p = 1)$ when $p > p_0$. Square packed axons idealized as cylinders (axial view) are shown for (**a**) $p = 1$, (**b**) $1 < p < p_0$, (**c**) $p = p_0$, and (**d**) $p > p_0$. The (virtual) restricted compartment is indicated by the dashed red line and the pores by the solid red lines. In a, $R_0(p = 1)$ is simply equal to R_{pore} according to Eq. 3.11 (the two other factors are unity for abutting cylinders). In b, the width of the gap between adjacent cylinders is less than $R_0(p = 1)$ and particles in the green highlighted area will tend to bias R_0 to a value less than $R_0(p = 1)$. In c, the gap between adjacent cylinders is exactly $R_0(p = 1)$ and $R_0(p = p_0)$ is equal to $R_0(p = 1)$ again. In d, the width of the gap between adjacent cylinders is greater than $R_0(p = 1)$ and particles in the highlighted area will tend to bias R_0 to a value greater than $R_0(p = 1)$.

the packing density at which the gap between adjacent cylinders is equal to R_0 for abutting cylinders (i.e., $L - L_{\text{abut}} = R_0(p = 1)$; noted as p_0 in Fig. 3.6a). For randomly packed cylinders, R_{pore} varies with each pore leading to a distribution of R_0, but these general principles otherwise hold.

The R_∞ parameter represents the effective radius of the restricted component at high frequencies, reflecting short time periods during which particles only sample the EAS close to their initial position. This overall pattern is indicated in Fig. 3.6b.

We would like to emphasize that the combination of our improved model with frequency-dependent radius on the one hand and Eqs. 3.11–3.13 on the other serve two purposes. The frequency dependence allows us to have a good description of simulated spectra at all frequencies and across a broad range of geometries. The empirically derived relationships described in Eqs. 3.11–3.13 relate this frequency dependence to

the underlying geometry, and appear to be valid for pore sizes spanning three orders of magnitude, as will be clear in the Results section.

3.3 Methods

3.3.1 Monte Carlo Simulations

The diffusion spectrum for spins surrounding cylinders was simulated using Monte Carlo techniques to represent the EAS. Simulations were conducted for a broad range of geometries, cylinder sizes and packing densities for comparison to the proposed EAS model. Periodically packed cylinders provide a useful test bed because model parameters are more straightforward to relate to the cylinder geometry (packing type, cylinder radius, and cylinder separation). Randomly packed cylinders were chosen to more realistically approximate axon bundles and test the applicability of this model with more complex geometries. MR signal attenuation was simulated in Camino (Cook et al., 2006; Hall and Alexander, 2009) for square, hexagonal, and random packing.

For square and hexagonally packed cylinders, cylinder radii were chosen to yield a useful range of EAS cross-sectional areas ("EAS areas") under the abutting case. That is, the cylinder radii were chosen such that abutting EAS areas had specific target radii R_{min} (Fig. 3.7). R_{min} is related to L_{abut} for square and hexagonally cylinders as

$$L_{\text{abut,sq}} = 2\sqrt{\pi/(4-\pi)} \cdot R_{\text{min}} \tag{3.14}$$

$$L_{\text{abut,hex}} = 2\sqrt{\pi/(\sqrt{3}-\pi/2)} \cdot R_{\text{min}}, \tag{3.15}$$

respectively. All combinations of $R_{\text{min}} \in \{0.05, 0.1, 0.5, 1, 5\}$ μm and $p \in \{1.00, 1.03, 1.06, 1.09, 1.12, 1.25, 1.50, 2.00\}$ were simulated.

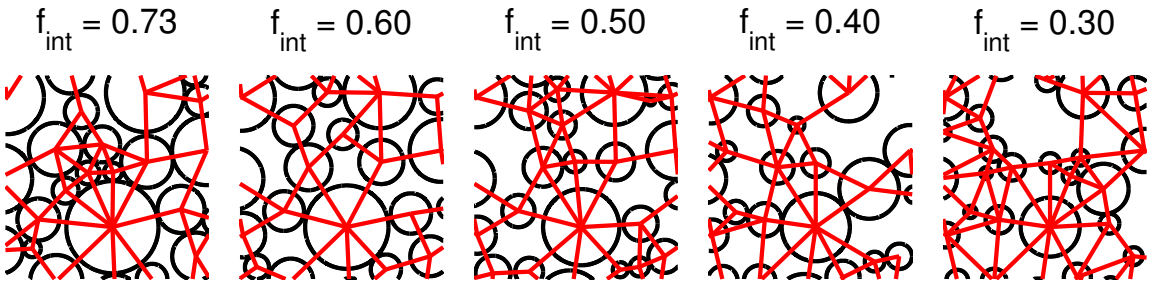


Figure 3.9: Axial view of randomly packed cylinders with gamma-distributed radii and various cylinder volume fractions f_{int} (only 4% of each tile of cylinders is shown). Segmentation of the EAS is indicated by straight lines.

For randomly packed cylinders, the cylinder radii were chosen to have a gamma distribution corresponding to the genu of the human corpus callosum (Aboitiz et al., 1992) as well as gamma distributions with twice and three times the cylinder radii. Simulations were performed with cylinder volume fractions of $f_{\text{int}} \in \{0.73, 0.6, 0.5, 0.4, 0.3\}$ by varying the cylinder spacing while keeping the cylinder distributions constant (Figs. 3.9). In total, the diffusion spectra for fifteen randomly packed geometries (three distributions at each of the five volume fractions) were simulated. Each simulation consisted of 500 cylinders in a base voxel, which was then tiled. Particles diffusing across any given edge of a tile reappear at the opposite edge, which enables an efficient and accurate simulation of a large-scale geometry based on a smaller-scale representation.

Diffusion gradient frequencies were chosen to simulate as much of the dynamic range of the diffusion spectra as possible with the available computational power. Apodized cosine oscillating gradients (Does et al., 2003) were used to minimize the encoding spectrum side lobes and were simulated at frequencies of 2, 4, ..., 10, 20, ..., 100, 200, ..., 1,000, 2,000, ..., 10,000, 20,000, ..., 100,000, 200,000, ..., 1,000,000 Hz. The duration of the oscillating gradient waveforms was chosen to sample narrowly about the target frequency, with a sampling width of 500 ms (2 Hz FWHM) for frequencies below 10,000 Hz and 4 ms (250 Hz) for higher frequencies.

Gradient Frequency (Hz)	Gradient Duration (ms)	Number of time steps	Walkers
2–10,000	500	8,000,000 ($R_{\min} = 0.05$ μm), 2,000,000 ($R_{\min} = 0.1$ μm), 250,000 ($R_{\min} \geq 0.5$ μm and random packing)	10,000 ($p \leq 1.12$), 30,000 ($p \geq 1.25$), 100,000 (random packing)
5,000–1,000,000	4	400,000	10,000 ($p \leq 1.12$), 30,000 ($p \geq 1.25$), 100,000 (random packing)

Table 3.1: Monte Carlo simulation parameters. In the first frequency range, more time steps were required for small $R_{\min}$ (periodic packing only) to keep the walker displacement per step much less than the distance between cylinders. Otherwise, $D_{\text{ext}}(\omega \approx 0)$ would be underestimated. In the second frequency range, the gradient duration was reduced due to computer memory constraints. $D_{\text{ext}}(\omega)$ was comparable where the frequency ranges overlapped. The number of walkers was increased for large p (periodic packing only) to compensate for the decreased signal of the restricted component.

The gradients were applied perpendicular to the cylinder axes. The peak amplitude of each waveform was chosen to produce a b value of 1 ms/μm^2.

The other simulation parameters are summarized in Table 3.1. $D_{\text{f}} = 2$ μm^2/ms (free water at room temperature) was used and no noise was added. Simulations were run in parallel on a computing cluster of Intel Xeon X5647 processors. The run times for simulations of 10,000 walkers each were approximately 12, 60, and 120 h of processor time for 250,000, 2,000,000, and 8,000,000 time steps, respectively.

The signal attenuation S/S_0 at each frequency was converted to a corresponding point in the diffusion spectrum $D(\omega)$ via $S = S_0 \exp(-b(\omega)D(\omega))$, where $b(\omega) = 1$ ms/μm^2 in our simulations. Particles within impermeable, uniform cylinders ("intra-axonal") were also simulated to verify that the simulated diffusion spectrum matched the known expression (Stepišnik, 1993).

3.3.2 Forward Model Comparison to Simulations for Regular Packing

The primary goal of this chapter is to compare the simulated EAS diffusion spectra to the forward model using the known properties of the simulated microstructure. The model for the EAS diffusion spectrum is calculated for each of the square and hexagonal packing simulated cases and compared to the simulated diffusion spectra. Forward modelling was not performed for randomly packed cylinders as analytic interpretations relating R_0 and R_∞ to R_{pore}, λ, and p could not be found. Although values for R_{pore}, λ, and p could be calculated numerically, they were not deemed sufficiently rigorous to compare to the forward model. However, the numerically determined values will be used for fitting as described in the subsection below.

3.3.3 Model Fitting

Fitting for the model parameters from the simulated $D_{\text{ext}}(\omega)$ data was used to determine whether parameter values can uniquely describe the geometries considered. Bayesian fitting with the Metropolis–Hastings algorithm was performed on the simulated $D_{\text{ext}}(\omega)$ of regular and random packings with uninformative, uniform priors and with the fit initialized by the result of non-linear least squares. For the non-linear least squares analysis, the initial value of lambda was given by $\sqrt{D_{\text{f}}/D(\omega = 0)}$ for all cases; the initial values of R_0 and R_∞ were arbitrarily set to 10 and 1 nm, respectively, for regular packing; and the initial values of the R_0 mean, R_0 standard deviation, and R_∞ were 1 μm, 10 nm, and 500 nm, respectively, for random packing.

For regular packing, the simulated $D_{\text{ext}}(\omega)$ spectra were fitted for λ, R_0, and R_∞. These three parameters were also calculated from analytical expressions for λ, R_{pore}, S/V, and p and compared with the fitted values to ascertain whether there is a one-to-one correspondence, which is required for the model to unambiguously describe

the microstructure. For random packing, the $D_{\text{ext}}(\omega)$ curves were fitted for λ, the mean and variance of a gamma distribution used to describe R_0, and R_∞. D_{f} was assumed to be that used in the simulations.

3.3.4 Describing the Microstructure

The fitted model parameters were used to calculate the ground truth values that describe the microstructural environment of the EAS. For square and hexagonal packing, λ was calculated numerically from p using existing expressions (Perrins et al., 1979; Sen and Basser, 2005a). Then, the cylinder centre-to-centre separation L and diameter L_{abut} (both only defined for regularly packed cylinders; Fig. 3.5) were calculated using Eqs. 3.11 and 3.12 in combination with the expressions for R_{pore} and S/V in Appendix 3.B.

While analytical calculation of R_{pore} can be performed for regular packings, this is not generally possible for random packings. Instead, the EAS of the simulated randomly packed cylinders was segmented into extra-cylinder pores using a custom algorithm (Fig 3.10). The resulting distribution for R_{pore} was compared to the mean value of the fitted R_0 distribution.

All segmentation and fitting were performed in MATLAB (R2011b, The MathWorks, Natick, MA).

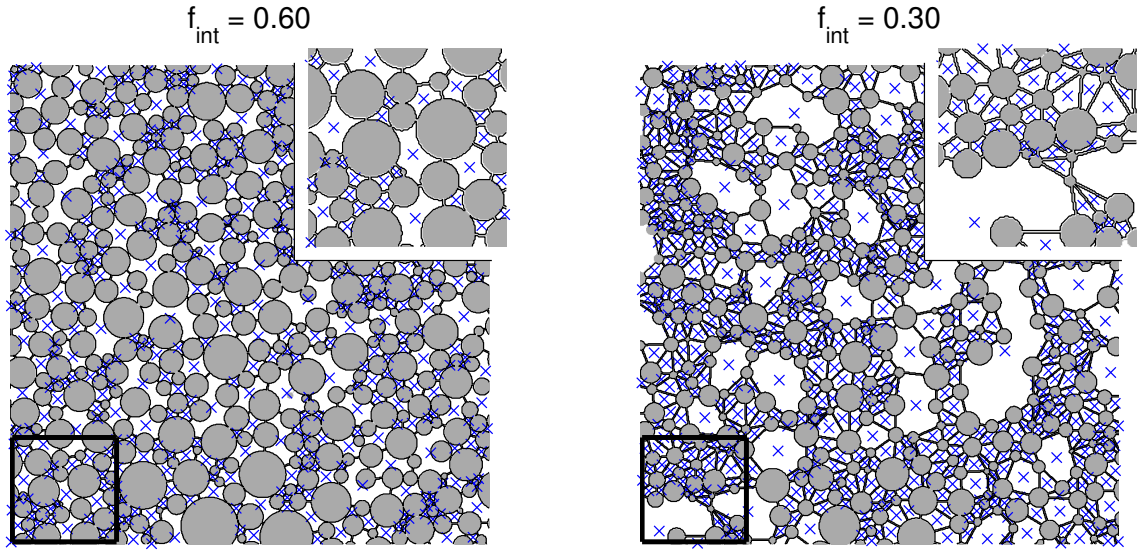


Figure 3.10: EAS pore segmentation for randomly packed cylinders with gamma-distributed radii for cylinders volume fractions $f_{\text{int}} = 0.60$ and 0.30. Pore centroids are indicated by $\times$. Inset are magnified views of the boxed regions. Note that simulated spins are only in the EAS.

3.4 Results

We begin by assessing the overall ability of the model to predict simulated diffusion spectra across a wide range of square and hexagonal cylinder packing geometries, including packing densities and spatial scales. We then assess the uniqueness of the model parameters λ, R_0, and R_∞ when fitted to diffusion spectra under ideal (noiseless) conditions. Finally, we compare the fitted parameters to physically meaningful geometrical values (L_{abut} and L for square and hexagonal packing and the mean R_{pore} for random packing).

3.4.1 Forward Model Comparison to Simulations for Regular Packing

Simulated and predicted EAS spectra are shown in Fig. 3.11 for square and hexagonal packing. The model matches the simulations well over a broad range of geometries. The quality of model agreement can be best appreciated by examining the residuals

(simulated spectra subtracted from model) found in Fig. 3.12. Overall, the residuals are very small, although there is a negative deviation from zero for square packed cylinders with relatively tight packing ($1 < p < 1.12$). This deviation occurs near the frequency of the initial rise in $D_{\text{ext}}(\omega)$, determined by the parameter R_0. It is worth noting that the residuals in these regions of the spectrum are particularly sensitive to differences between the simulations and predictions since this is where the spectrum is changing most rapidly. Put another way, the residuals measure the vertical difference between model and simulation, which can be large in regions of rapid change, even for curves that exhibit only subtle differences by eye. Hexagonal packings do not show this feature in the residuals, indicating a better overall model prediction (i.e., residuals that are generally very close to zero).

Simulated and predicted EAS spectra are shown in Fig. 3.13 for random packing. The simulated and modelled $D_{\text{ext}}(\omega)$ also match well over a broad range of geometries. The residuals, shown in Fig. 3.14, have smaller absolute values than those for regular packing, but also exhibit a consistency in the form of disagreement between model and simulation (under-estimating the spectrum at the low frequency end of the transition and over-estimating at the high frequency end).

3.4.2 Model Fitting

The tortuosity parameter is straightforward to interpret and is compared to analytically calculated values (Perrins et al., 1979; Sen and Basser, 2005a) for square and hexagonally packed cylinders in Fig. 3.15a and d, respectively. The agreement between the fitted and theoretical values is very good in all cases.

The abstract model parameters R_0 and R_∞ are crucial to evaluate because they only have an empirical relationship to parameters of the simulated geometries. Thus, it is important to establish that these parameters (a) capture the expected relationships with λ, R_{pore}, S/V, and p as indicated in Eqs. 3.11–3.13 and (b) exhibit an

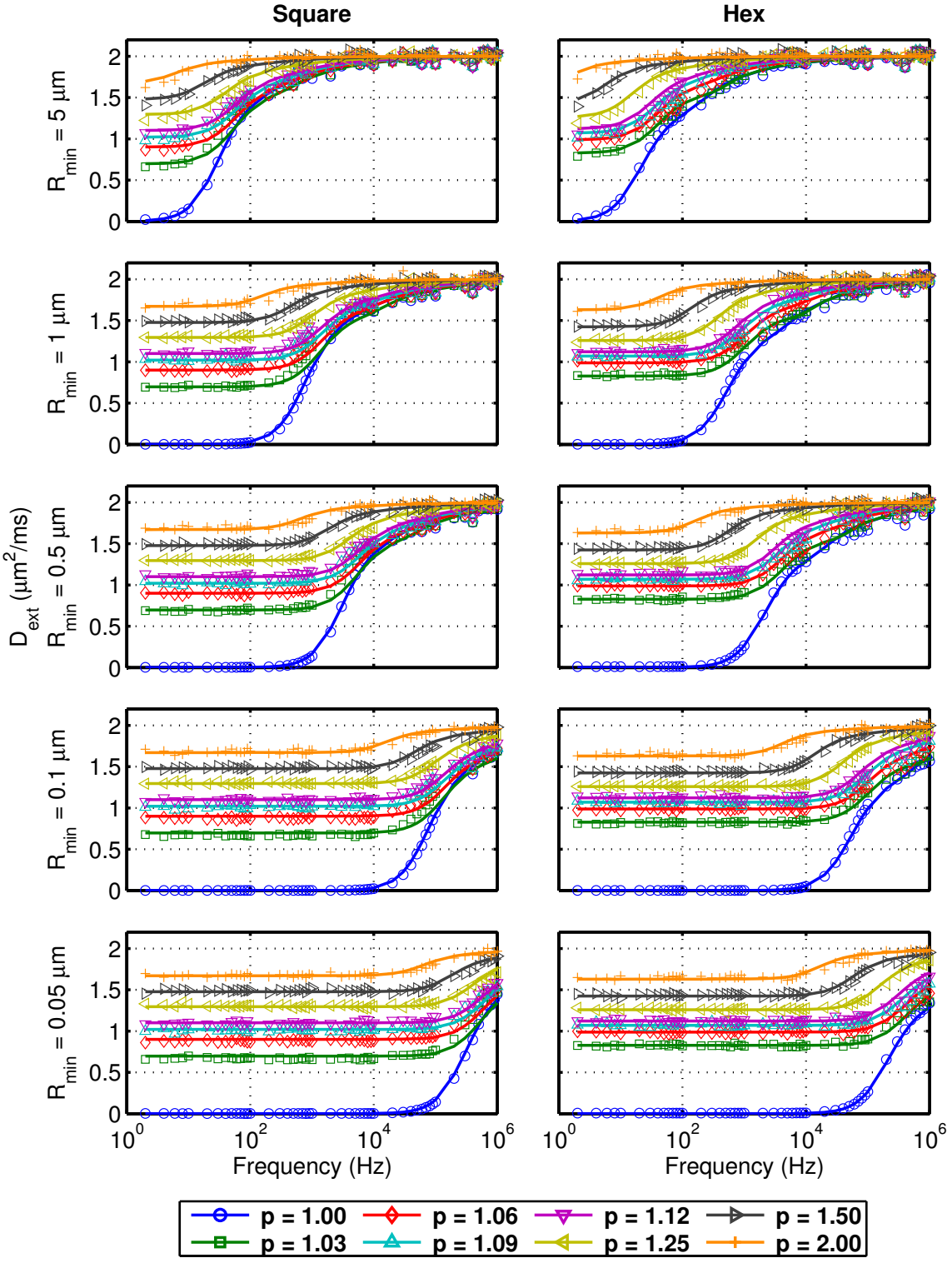


Figure 3.11: Simulated (markers) and predicted (lines) EAS diffusion spectra $D_{\text{ext}}(\omega)$ for square and hexagonally packed cylinders.

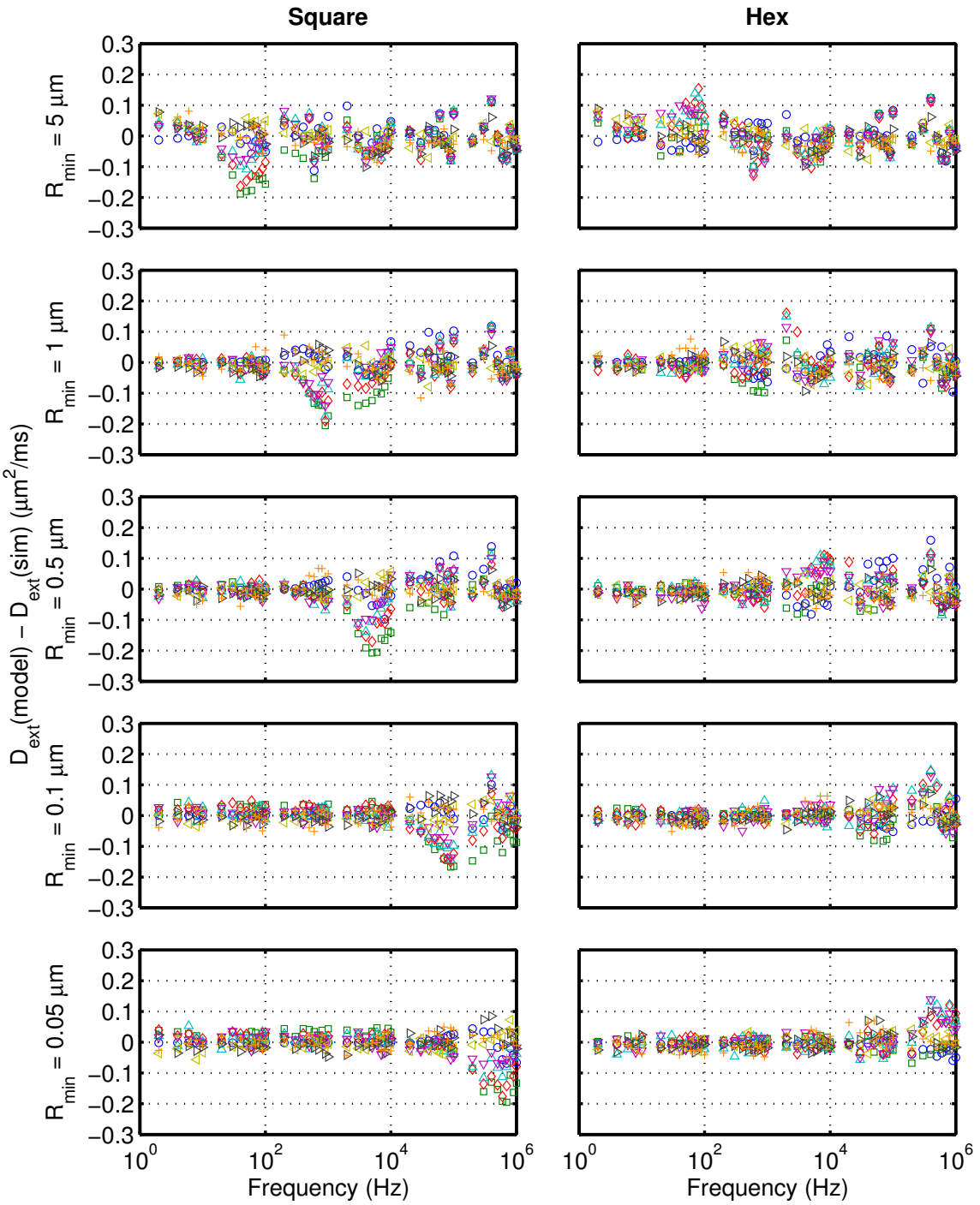


Figure 3.12: Residuals between simulated and predicted EAS diffusion spectra $D_{\text{ext}}(\omega)$ for square and hexagonally packed cylinders. The markers are as in Fig. 3.11.

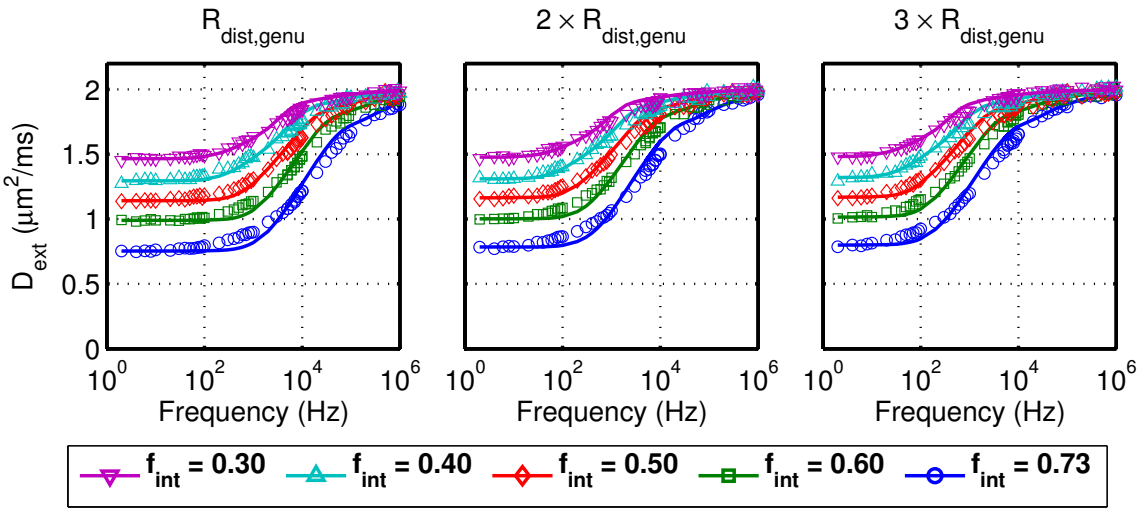


Figure 3.13: Simulated (markers) and predicted (lines) EAS diffusion spectra $D_{\text{ext}}(\omega)$ for randomly packed cylinders over a range of five cylinder volume fractions f_{int} and cylinders with gamma-variate radius distributions that are one, two, and three times those of axons in the genu (left to right), i.e., the scale parameter of the distribution was changed, but not the shape.

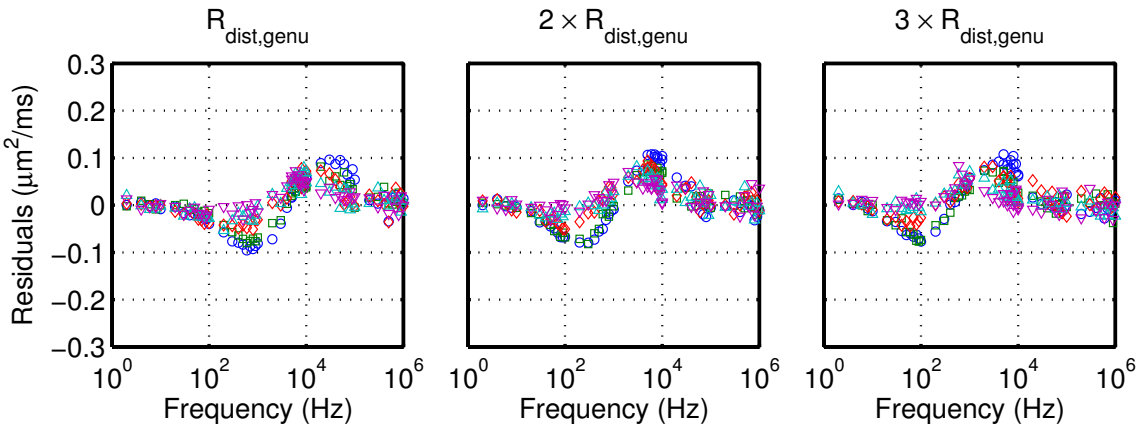


Figure 3.14: Residuals between simulated and predicted EAS diffusion spectra $D_{\text{ext}}(\omega)$ for randomly packed cylinders. The markers are as in Fig. 3.13.

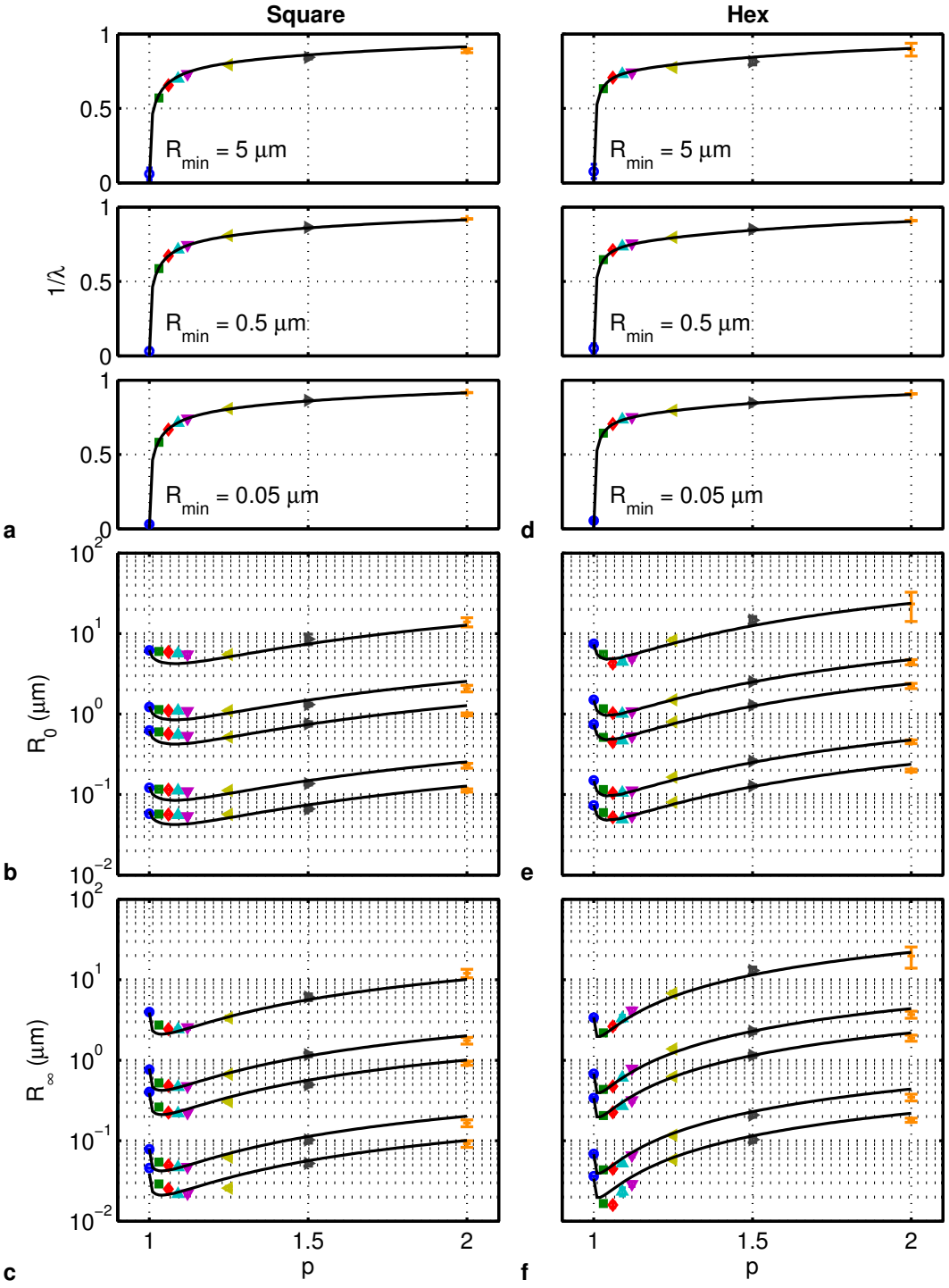


Figure 3.15: Fitted (mean ± SD; markers) and predicted (lines) model parameters (**a**) $1/\lambda$ ($R_{\min} = 1$ and 0.1 µm are similar and not shown), (**b**) R_0, and (**c**) R_∞ for square packed cylinders. The curves in b and c denote $R_{\min} = 5, 1, 0.5, 0.1, 0.05$ µm (top to bottom). **d, e, f**: As a, b, and c, but for hexagonally packed cylinders. $1/\lambda$ is plotted instead of λ in order to show the abutting case ($p = 1$). The markers are as in Fig. 3.11.

(approximately) one-to-one mapping with microstructural geometry. If there were no unique mapping, the estimation of the microstructural geometry would be highly problematic without introducing prior knowledge. In the absence of a way to relate R_0 and R_∞ to a distribution of randomly packed cylinders, the regular packings play a crucial role in these goals. Model fits to simulated data show that the radius parameters are in reasonable agreement with calculated values for square and hexagonal packing as shown in Fig. 3.15b, c, e, and f. For square packing, the fitted values of R_0 (markers) overestimate the expected R_0 (lines) for small values of p, although the general trends are in good agreement. One possible cause of disagreement in simulated and expected R_0 for small p is the presence of straight paths between cylinders, which are parallel to the diffusion encoding direction and are not accounted for in the calculation of R_{pore} (and in general represent a non-realistic aspect of square packings). The fitted values of R_∞ generally match the model well. The parameters R_0 and R_∞ appear to give a unique mapping to all the combinations of EAS length scales and packing densities simulated.

For square and hexagonal packing, the calculated values for L_{abut} and L from R_0 and R_∞ versus true values are presented in Fig. 3.16. The estimates match the simulated values over a wide range of spatial scales. The accuracy is high despite our relatively simple cylinder representation of the complicated EAS geometry, which effectively combines a variety of spatial scales by including small channels as well as large central pores.

For randomly packed cylinders, the model using a distribution of R_0 fits well to the diffusion spectra (Fig. 3.13; residuals, which are smaller than those for the regular packing $D(\omega)$, are shown in Fig. 3.14). The single R_0 model used for regular packing did not fit the random packing data well (not shown), which indicates the need for an R_0 distribution (a gamma distribution was used here, but other positive-valued distributions may be applied as well). The R_0 distributions from fitting and from

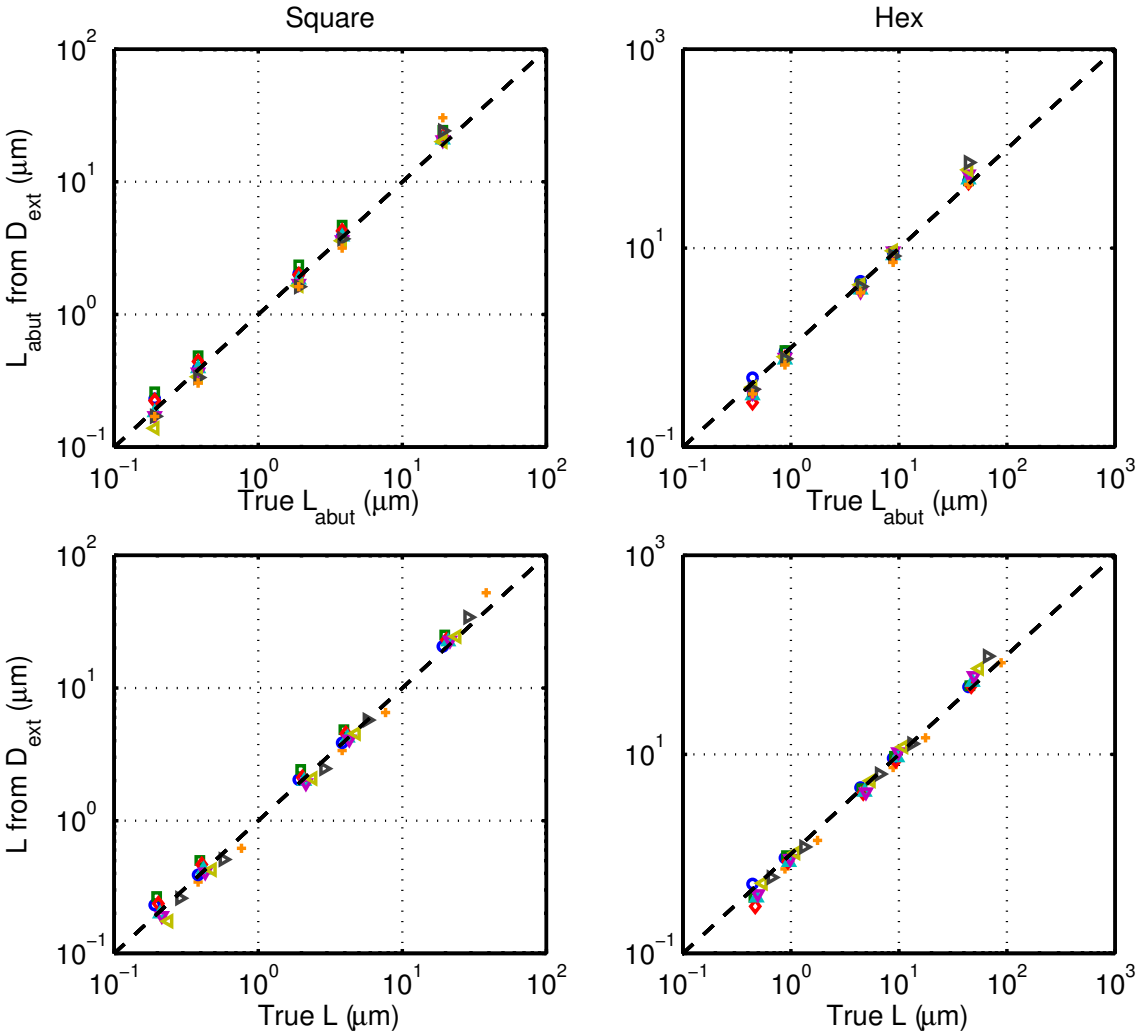


Figure 3.16: Abutting cylinder separation L_{abut} and cylinder separation L for square and hexagonally packed cylinders calculated from the fitted values of λ, R_0, and R_∞. The markers are as in Fig. 3.15.

the EAS segmentation algorithm, when weighted by the volume of each pore, are shown in Fig. 3.17a. At high packing densities ($f_{\text{int}} \geq 0.6$), they broadly match, but at low densities a bimodal distribution is evident. The random placement of cylinders by Camino is likely the cause of the bimodality. At low f_{int}, the cylinders exhibit "clumping" from random placement (Fig. 3.10) that could be characterized by a bimodal distribution. An alternative arrangement of cylinders with the same f_{int}, but more even spacing, should yield a more unimodal distribution. At high f_{int}, Camino spaces the cylinders more evenly in order to minimize the amount of EAS, which would automatically yield a unimodal distribution. The volume weighting of the R_0 distribution is likely needed for the fitting because without volume weighting there was an even stronger bimodal distribution at all f_{int} (not shown). The means of the distributions from fitting and segmentation closely match (Fig. 3.17b). The fitted values of R_∞ match the model quite well (Fig. 3.17c).

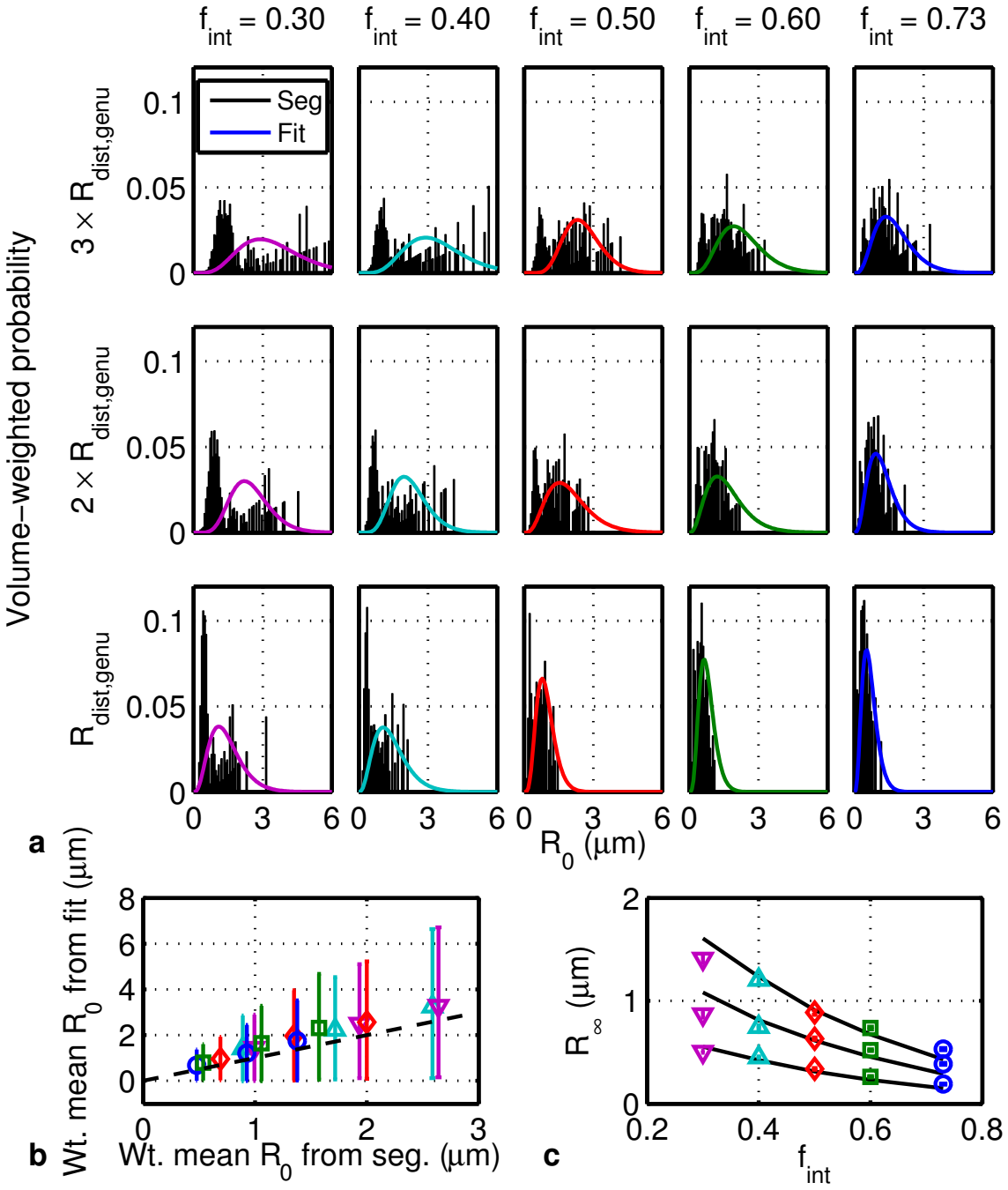


Figure 3.17: **a:** Distributions from segmentation (bars) and prediction (lines) for model parameter R_0 weighted by cylinder volume fraction. **b:** The mean and standard deviations of the volume-weighted R_0 distributions from fitting versus segmentation corresponding to those in a. **c:** Fitted (mean $\pm$ SD; markers) and predicted (lines) model parameter R_∞ for randomly packed cylinders. The curves denote radius distributions that are three, two, and one times those of axons in the genu (top to bottom). The markers are as in Fig. 3.13.

3.5 Discussion

In this chapter we present an analytical model for the diffusion spectrum of the EAS that is applicable to square, hexagonally, and randomly packed cylinders. While an idealized representation (axons are neither perfectly cylindrical nor impermeable, and glia are ignored), this kind of simulation has nevertheless been very powerful for gaining insights into diffusion in white matter (Cook et al., 2006; Hall and Alexander, 2009). Proper modelling of the EAS diffusion spectrum will aid in the correct interpretation of oscillating gradient diffusion measurements. Although the diffusion spectrum of the EAS is known not to be spectrally flat (Stepišnik et al., 2001; Parsons et al., 2006), our empirical model is to our knowledge the first to predict the EAS diffusion spectrum across the entire frequency range. The model is able to accomplish this with parameters that have a one-to-one correspondence to the microstructure of idealized cylinders. Below we discuss alternative models and considerations when acquiring and analysing real data.

3.5.1 Alternative Models

Our model is the simplest we could devise that described all of the simulated data and provided a reasonable degree of biophysical interpretability. For example, a model that describes EAS diffusion with one free and two restricted components with fixed radius across frequencies also provides good agreement with our simulations. However, such a model would entail four parameters (e.g., tortuosity, volume fraction of one restricted component, and two radii) instead of three with our proposed model, while not giving improved accuracy. Figure 3.18 shows simulated data from a representative case of square packed cylinders ($\times$) along with two model fits (lines): two restricted populations of cylinders coupled (bimodal model, left) and the model introduced in this chapter (right).

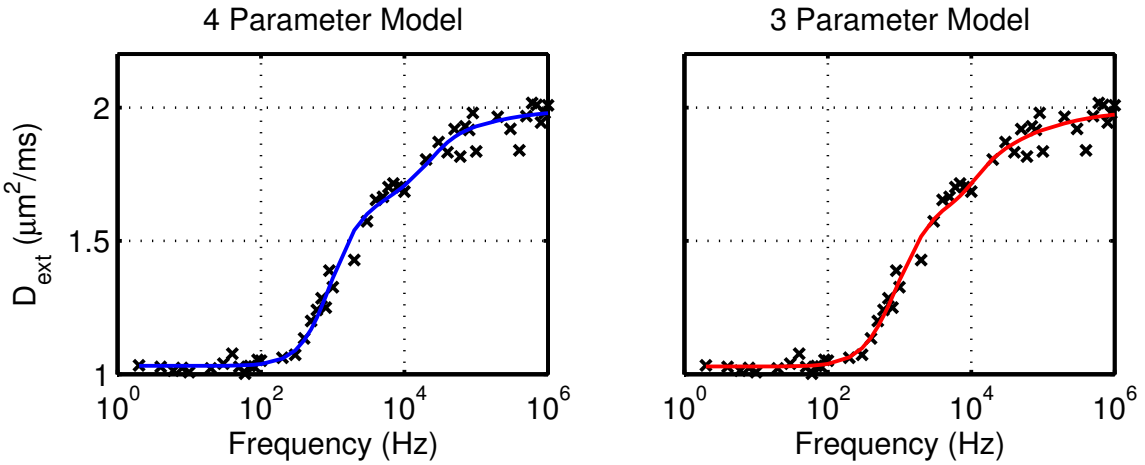


Figure 3.18: Comparison of fitting to $D_{\text{ext}}(\omega)$ using a bimodal axon radius distribution (left) and the model from this chapter (right). Both fit the data, but the former has four parameters and the latter three.

The absolute value of the residuals (Fig. 3.19) between each of the models above and the data are comparable and do not justify the addition of a fourth parameter. This can be quantified by the Bayesian information criterion (BIC; Schwarz (1978)), which penalizes the likelihood of a model by the number of parameters, and is given by

$$\text{BIC} = n \ln \left[\frac{1}{1-n} \sum_{i=1}^{n} (x_i - \hat{x}_i)^2 \right] + k \ln(n) \tag{3.16}$$

where n is the number of data points, x the observed data, $\hat{x}$ the predicted data, and k the number of parameters. The BIC for the model presented in this chapter (BIC $=$ -314) is lower than that of the bimodal model (BIC $=$ -306), which again does not justify the addition of a fourth parameter.

Alternative formulations for $D_{\text{ext}}(\omega)$ have been proposed. The closest to the one presented in this chapter is that of Lasič et al. (2009). Their model also uses Eq. 3.1, but for the purpose of characterizing the exchange of water molecules between microscopic water droplets. The restricted diffusion attenuation is modelled as a sum of diffusion spectra weighted by droplet volume and size distribution as well (cf. Eq. 3.8).

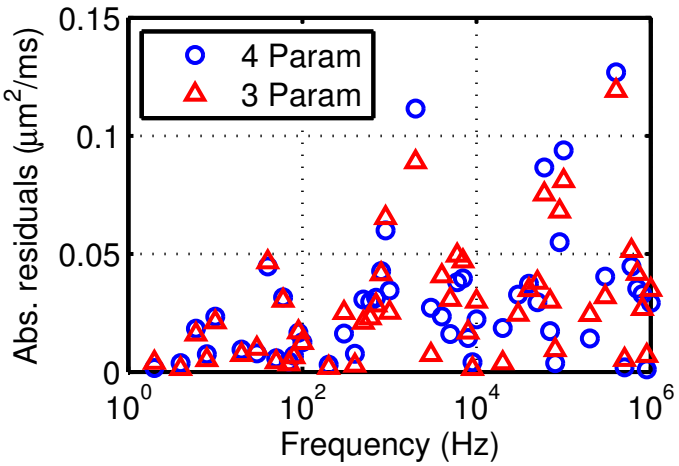


Figure 3.19: Absolute residuals of fitting to $D_{\text{ext}}(\omega)$ using a bimodal axon radius distribution (circles) and the model from this chapter (triangles).

However, in their model, the pore size does not vary with frequency. Furthermore, the motivation for our model differs in that we seek to describe the microstructure of the EAS.

Parsons et al. (2006) found a relationship between the estimated pore size around tightly packed beads and the bead size from a model similar to that described by Eq. 3.1. However, the restricted component of their model, like that of Lasič et al. (2009), also uses a constant pore size over all frequencies, which describes the intermediate frequency regions of $D_{\text{ext}}(\omega)$ well, but results in less accuracy at high frequencies. Our model describes $D_{\text{ext}}(\omega)$ with good accuracy at all frequencies and applies to tight as well as sparse packing.

Complementary to the frequency domain diffusion spectrum models above, there exists a large body of literature that considers the apparent diffusion coefficient in the time domain as a function of diffusion time Δ measured with pulsed gradients. Latour et al. (1993, 1994) used a Padé approximant to interpolate $D(\Delta)$ and extract tortuosity and pore size. Our model empirically models $D(\omega)$ to estimate similar parameters. There is also much work on the calculation of tortuosity for many geometries (in two dimensions with cylinders (Transvalidou and Sotirchos, 1996; Novikov and Fieremans,

2012) and random shapes (Chen and Nicholson, 2000) and in three dimensions (Jiang et al., 2001; Hrabe et al., 2004; Tao et al., 2005; Nandigam and Kroll, 2007; Jin et al., 2008)) and relating it to microstructure. Our work, which aims instead to relate the whole of $D(\omega)$ to microstructure, can provide more information than tortuosity would alone.

Alternate pulse sequences have also been proposed for increased sensitivity to axon diameter. Oscillating gradient sequences with variable waveform periods (Kiruluta, 2008; Shemesh et al., 2013) and time-varying direction (Lundell et al., 2014) have been proposed. As well, numerically optimized pulsed gradient sequences have also been proposed (Drobnjak et al., 2010; Drobnjak and Alexander, 2011). However, measurement of the extremely small length scales of the EAS will pose significant challenges.

3.5.2 Practical Considerations

There are practical considerations to be noted when attempting to measure the diffusion spectrum (typically with an oscillating gradient spin echo sequence (Parsons et al., 2003)) including the T_2 signal decay, hardware constraints, and peripheral nerve stimulation (PNS) of the subject. Measurements at low frequencies are governed by T_2 decay, which limits the gradient waveform duration and thus the minimum frequency. Measurements at high frequencies are limited by the diffusion contrast achievable and by PNS. Sufficient diffusion contrast requires a large number of gradient oscillations (also limited by T_2 decay) and/or high gradient amplitude (limited by hardware). The former is a limiting factor for low frequencies and the latter for high frequencies. PNS could also be problematic at higher frequencies, which require high gradient slew rates. This could potentially be alleviated by the use of head-only gradient coils, which can achieve higher slew rates before the onset of PNS (Zhang et al., 2003; Wong, 2012).

MR system	Max. frequency (Hz)	b (s/mm^2)	Reference
Human	50	300	Baron and Beaulieu (2014)
Human	63	200	Van et al. (2014)
Animal	150	700	Aggarwal et al. (2012)
Animal	250	400	Xu et al. (2012)
Microscopy	1,000	3,200	Portnoy et al. (2012)

Table 3.2: Recent oscillating gradient experiments in literature.

Table 3.2 lists typical maximum frequencies for various types of MR systems and shows that current clinical systems are insufficient for probing $D_{\text{ext}}(\omega)$ of white matter (cf. Fig. 3.13). Animal systems can probe the frequencies at which $D_{\text{ext}}(\omega)$ begins to change and microscopy systems can access a significant portion of the spectrum.

Although our interest in white matter led us to simulate cylinders on the scale of axons, technological limitations severely limit the measurement of $D(\omega)$ at sufficiently high frequencies. Information about the size of the extracellular space is primarily reflected in the transition region of the diffusion spectrum, meaning that accurate estimation of compartment sizes requires sampling at frequencies up to the maximum gradient in the transition. Assuming a characteristic "extracellular radius" of 0.1 μm, frequencies of approximately 60 kHz (see Fig. 3.13) will be required to measure the diffusion spectrum for $D_{\text{f}} = 2$ μm^2/ms (in vivo) and 6 kHz for $D_{\text{f}} = 0.2$ μm^2/ms (fixed tissue, calculation not shown). The larger length scale of the rat sciatic nerve (≈ 1 μm axon and pore radii) potentially allows estimation of parameters using animal scanners with a maximum gradient amplitude of 750 mT/m (allowing a b value of 0.6 ms/μm^2) at frequencies up to 300 Hz. This could be useful for tracking the progression of experimental autoimmune neuritis (Assaf et al., 2002) and diabetic nerve regeneration (Malysz et al., 2010). Moreover, there may be other cellular microstructures of interest outside of the nervous system characterized by a sufficiently large length scale for this model to be of interest.

3.5.3 Model Considerations

The model presented in this paper is a highly idealized picture of the EAS, and several factors that may contribute to measurements of the diffusion spectrum of white matter have been neglected. For instance, measurements will also have contribution from the intra-axonal space, and separating the two compartments using diffusion spectrum measurements is challenging. Other complications include non-parallel and/or non-cylindrical axons, exchange between different compartments, and the presence of other cellular processes, such as glial cells, which may also contribute to the measured shape of the diffusion spectrum.

Finally, in order for our model to be deployed in real tissue, it will be necessary to account for both intra- and extracellular spaces. This non-trivial problem is the topic of Chapter 4.

3.6 Conclusions

We have presented an empirical model for the diffusion spectra of particles in the extra-axonal space. This model was able to predict the spectra from extensive Monte Carlo simulations. We demonstrated the estimation of tortuosity, pore size, and surface-to-volume ratio for parallel cylinders with a variety of packing geometries and a wide range of spatial separations. This model can potentially be used to estimate the geometric properties of cylindrical structures such as those found in white matter.

3.A Calculations to Support the Fast Exchange Limit Assumption

Lee and Springer (2003) define a measurement of exchange between two compartments to be in the fast exchange limit (FXL) when $|q^2(D_\mathrm{r} - D_\mathrm{f})| \ll \tau_\mathrm{r}^{-1} + \tau_\mathrm{f}^{-1}$, where the

subscripts r and f reflect the restricted and free components in our model, respectively, and τ is the mean residence time of particles in a compartment. Below we approximate the conditions of an OGSE experiment and show it would be in the FXL.

We will consider the left hand side $|q^2(D_\mathrm{r} - D_\mathrm{f})|$ at low and high frequencies separately. At 30 Hz, taking $q^2 = 0.03$ $\mu\mathrm{m}^{-2}$ (corresponding to a cosine OGSE waveform with a single oscillation, duration of 30 ms, and b value of 0.6 ms/μm^2 and achievable with animal scanners) and $(D_\mathrm{r} - D_\mathrm{f}) = 1$ $\mu\mathrm{m}^2$/ms, $|q^2(D_\mathrm{r} - D_\mathrm{f})|$ is approximately 0.03 ms^{-1}. At high frequencies, $D_\mathrm{r} \approx D_\mathrm{f}$ and $|q^2(D_\mathrm{r} - D_\mathrm{f})|$ approaches zero.

Now we calculate the right hand side $\tau_\mathrm{r}^{-1} + \tau_\mathrm{f}^{-1}$. To approximate the residence time in a pore τ_r, we calculate the time required for e^{-1} ($\approx 37\%$) of a population of particles to remain within a distance R_pore with an apparent diffusion coefficient of $D_0 = D_\mathrm{f}/\lambda^2$. We assume Gaussian diffusion, but account for the hindrance by the cylinder walls using the reduced diffusion coefficient D_0. With $R_\mathrm{pore} = 0.1$ μm and $D_0 = 1$ $\mu\mathrm{m}^2$/ms, this yields $\tau_\mathrm{r} \approx 0.2$ ms.

To calculate the residence time in the free diffusion regime τ_f, we calculate the time required for one standard deviation of particles to diffuse the distance between two pores (taken as 1 μm) with free diffusion coefficient 2 $\mu\mathrm{m}^2$/ms. This yields $\tau_\mathrm{f} \approx 0.25$ ms.

Thus, the right hand side of the FXL condition, $\tau_\mathrm{r}^{-1} + \tau_\mathrm{f}^{-1}$, is approximately 9 ms^{-1}.

Therefore, for the geometries examined and realistic q values, measurements are within the FXL regime (0.03 ms^{-1} $\ll$ 9 ms^{-1}). These should be seen as order of magnitude calculations given that residence times are rough approximates.

3.B Geometric Quantities for Periodically Packed Cylinders

3.B.1 Effective Pore Radius

The effective pore radius R_{pore} is defined to be the mean distance from the pore centroid to boundary in a plane perpendicular to the cylinders. For square packed cylinders, it is given by

$$R_{\text{pore}} = \frac{L_{\text{abut}}}{2(\pi - 2\phi)} \int_{\frac{3}{4}\pi+\phi}^{\frac{7}{4}\pi-\phi} \sqrt{(\cos\theta + p)^2 + (\sin\theta + p)^2} d\theta \tag{3.17}$$

$$\phi = \sin^{-1}\left(\frac{1}{\sqrt{2}p}\right) \tag{3.18}$$

and, for hexagonally packed cylinders,

$$R_{\text{pore}} = \frac{L_{\text{abut}}}{2(\pi - 2\phi)} \int_{\pi+\phi}^{2\pi-\phi} \sqrt{(\cos\theta)^2 + \left(\sin\theta + \frac{2p}{\sqrt{3}}\right)^2} d\theta \tag{3.19}$$

$$\phi = \sin^{-1}\left(\frac{\sqrt{3}}{2p}\right), \tag{3.20}$$

where 2ϕ represents the angle blocked by a cylinder with respect to the pore centre.

3.B.2 Pore Surface-to-Volume Ratio

For square packed cylinders, the ratio of surface area to pore volume S/V is given by

$$\frac{S}{V} = \frac{4\pi}{L_{\text{abut}}\left(4p^2 - \pi\right)} \tag{3.21}$$

and, for hexagonally packed cylinders,

$$\frac{S}{V} = \frac{4\pi}{L_{\text{abut}}\left(2\sqrt{3}p^2 - \pi\right)}. \tag{3.22}$$

Chapter 4

Measurements of Diffusion Spectra

4.1 Introduction

In the previous chapter, we used Monte Carlo simulations of extra-axonal diffusion spectra in a variety of geometric configurations and showed excellent agreement with our analytic model. The goal of this chapter is to test the performance of our model against real experimental data.

In a first experiment, we measure diffusion spectra in a physical phantom (Fieremans et al., 2008b) made of parallel, solid (non-hollow) fibres in order to validate the extra-axonal space (EAS) model described in Chapter 3. In a second experiment, we measure diffusion spectra in biological specimens (pig corpus callosum). Fitting a model to this second set of data requires an extension of our model to include intra-axonal space (IAS), which makes up approximately 75% of white matter (Nicholson, 2001).

In the following, we first describe the phantom experiment in detail. We then return to the model and propose an extension that accounts for intracellular space. A description of the second experimental results then follows.

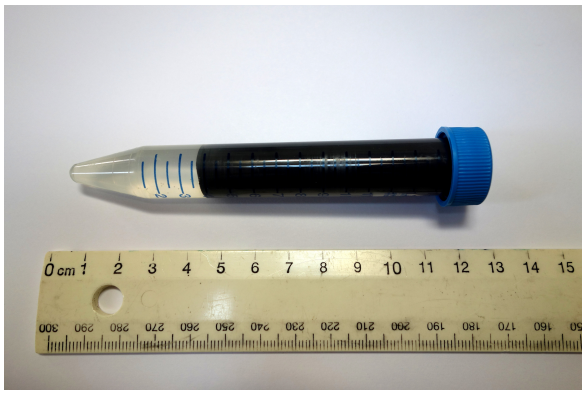


Figure 4.1: Fibre phantom. The Dyneema fibres are encased in the black heat-shrink tubing within the water-filled conical centrifuge tube.

4.2 Fibre Phantom Experiment

In order to test the predictions of the EAS model presented in Chapter 3, the diffusion spectrum for an extra-cylindrical phantom was measured using OGSE. A phantom was chosen because its geometry yields signal from only the extra-cylindrical compartment and the material composition can be optimized. The composition was optimal because of relatively large fibre radius (yielding relatively large EAS pores, which sets the transition region of the diffusion spectrum at accessible frequencies) and low surface T_2 relaxivity (allowing longer TE) due to the phantom being hydrophobic and reasonably susceptibility matched to water. It consisted of approximately 50,000 parallel, solid Dyneema fibres (SK75 1760 dTex, DSM Dyneema B.V., Urmond, The Netherlands) and was made by collaborators in the USA based on their published procedures (Fieremans et al., 2008b). These fibres (each 17 $\pm$ 2.6 μm in diameter and approximately 8 cm long) were encased in heat-shrink tubing (approximately 1 cm in diameter after shrinkage) and placed in a 15-mL conical centrifuge tube filled with tap water (Fig. 4.1). In addition to scanning the phantom, we also performed Monte Carlo simulations of an in silico version of the real phantom.

4.2.1 Methods

4.2.1.1 Experiment

All scans were performed on a 9.4T scanner (400-MR, Varian, Inc., Yarnton, United Kingdom) using a 26-mm diameter birdcage radiofrequency coil (RAPID Biomedical GmbH, Rimpar, Germany) in collaboration with colleagues at University College London. Although each gradient was rated up to an amplitude and slew rate of 1000 mT/m and 200 μs, respectively, they were only run up to 750 mT/m if necessary and 180 μs, respectively, to reduce eddy current effects and bore heating. The fibre phantom was allowed to equilibrate to room temperature before being placed in the magnet. The surface temperature of the conical tube was continuously monitored by fibre optic sensor (SA Instruments, Inc., Stony Brook, NY) and was (18 ± 1) °C.

The phantom was placed in the magnet with fibres parallel to the bore (and the field) to minimize any susceptibility effects. A Carr–Purcell–Meiboom–Gill (CPMG) sequence (number of slices = 1; field of view = 20 mm × 20 mm; slice thickness = 5 mm; TR = 10,000 ms; TE = 16, 32, ..., 2048 ms; matrix = 64 × 64; readout bandwidth = 1562 Hz/px; averages = 2) was used to measure the proton densities and T_2 decay constants of the bulk water and fibre voxels. The proton density measurement was used to calculate the fibre volume fraction by comparing signals within and outside of the fibres (Fieremans et al., 2008a).

Axial diffusion-weighted images were acquired using a 2D DTI sequence with single-line readout. PGSE was used to sample the diffusion spectrum at zero frequency and OGSE at higher frequencies. Trapezoid-modulated apodized cosine gradients were used in order to achieve higher diffusion weighting compared to non-modulated sinusoidal gradients (Ianuş et al., 2013). The diffusion gradient waveforms before the refocusing pulse were approximately 40 ms in duration with zero padding at the end, which was chosen by an iterative algorithm to minimize the amplitude

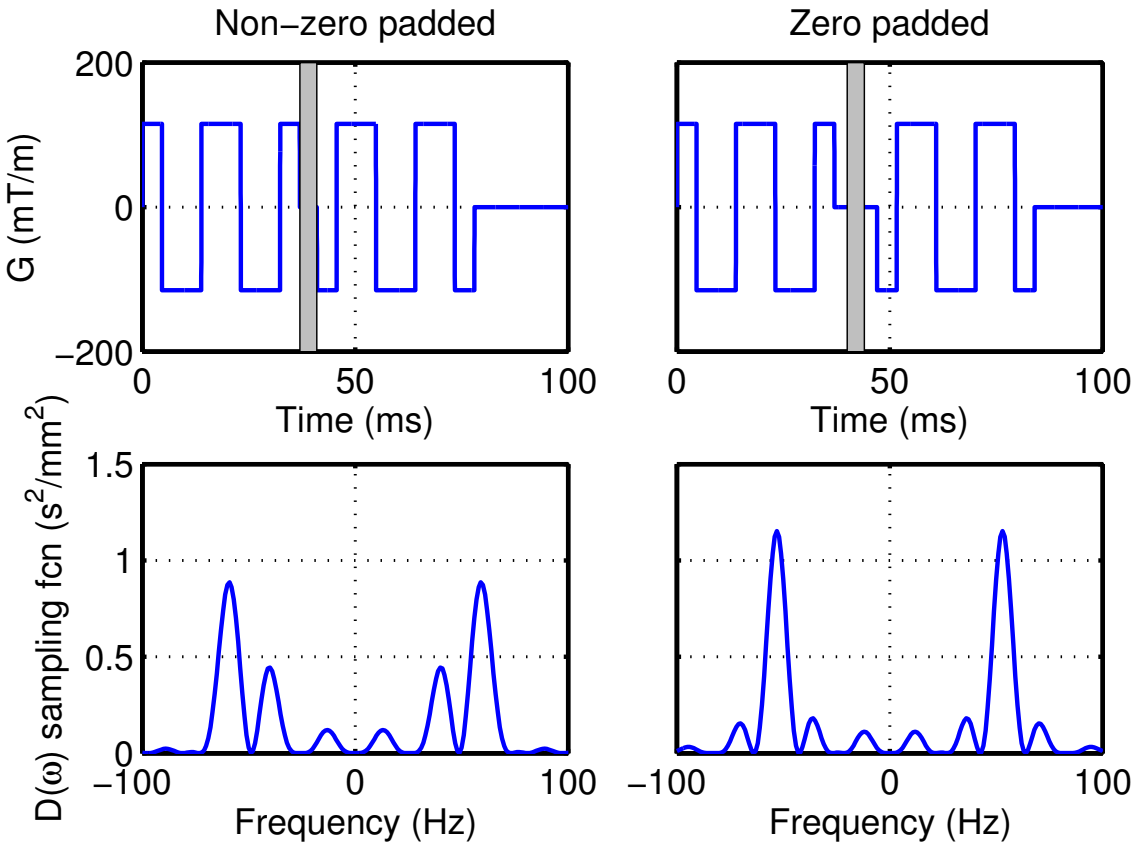


Figure 4.2: OGSE gradient waveforms with two cycles per waveform without (top left) and with (top right) zero padding to illustrate the difference in the $D(\omega)$ sampling function (bottom). The zero-padded version is preferred because most of the spectral density of the sampling function is narrowly centred on the desired frequency. The 4 ms allocated to the refocusing pulse is indicated by the shaded area. Note that the amplitudes of the non-zero padded and zero padded waveforms are slightly different in order to achieve the desired b value of 0.5 ms/μm^2.

of the side lobes of the sampling function (Fig. 4.2). The optimal spacing between the gradient waveforms to reduce side lobes is an integer or integer-plus-0.5 multiple of the waveform period when the waveform after the refocusing pulse is of inverse or same polarity, respectively (Van et al., 2014). The waveform after the refocusing pulse was a time-reversed version of the first and, for selected frequencies, was of inverse polarity also to reduce side lobes (Van et al., 2014). The refocusing pulse and crusher gradients had a total duration of 4 ms. The diffusion gradients sampled about the target frequencies with a FWHM of 10–12 Hz.

Gradient scheme	Cycles per waveform N	Zero padding (ms)	Invert second waveform?	Frequency (Hz)	TR (ms)
PGSE	-	0	N	0	2000
OGSE	1	0	Y	22	2000
	2	3.0	N	53	2300
	3	1.5	N	77	2700
	4	2.7	Y	107	3100
	5	0	N	125	3500
	6	1.3	Y	154	3900
	7	0.8	Y	178	4300
	8	0.5	Y	202	4700
	9	0.2	Y	226	5000
	10	0	Y	249	5400
	11	0.6	N	279	5800
	12	0.4	N	303	6200
	13	0.2	N	327	6600
	14	0.1	N	350	7000

Table 4.1: Diffusion gradient parameters used for the fibre phantom.

A b value of 0.5 ms/μm^2 was chosen in order to achieve a maximum frequency of 350 Hz (given the TE and gradient amplitude constraints), which preliminary simulations showed was necessary to characterize the diffusion spectrum. A PGSE sequence with $\Delta = 79$ ms and $\delta = 1$ ms was used to sample around zero frequency. The diffusion gradient parameters and TR, which was set approximately proportional to duty cycle to prevent bore heating, are given in Table 4.1. At each frequency, a $b = 0$ scan was followed by scans with diffusion weighting in the readout, phase encoding, and slice selection directions. The other scan parameters are as follows: number of slices = 1, field of view = 20 mm × 20 mm, slice thickness = 5 mm, TE = 90 ms, matrix = 64 × 64, readout bandwidth = 1953 Hz/px, and averages = 2. The OGSE scans were ordered such that the mean duty cycle of adjacent scans varied as little as possible (i.e., the order was $N = 1, 14, 2, 13, 3, 12, 4, 11, 5, 10, 6, 9, 7, 8$, where N is the number of cycles per waveform).

A set of scans with TE = 110 ms was also performed to investigate eddy current effects on the readout. The TE = 90 ms scans had no dead time between the end of

the second gradient waveform and the readout; the TE = 110 ms scans had 10 ms before the first and after the second waveforms.

4.2.1.2 Analysis

Raw data from the scanner was reconstructed by fast Fourier transform and region-of-interest masks were created manually using FSLView (Smith et al., 2004). Bayesian fitting to the model with the Metropolis–Hastings algorithm was performed, with the fit initialized by the result of non-linear least squares. The non-linear least squares analysis initial values for $1/\lambda$, $\mu_{R,0}$, $\sigma_{R,0}$, and R_∞ were set to $\sqrt{D(0)/D_\mathrm{f}}$, 1 μm, 0.01 μm, and 0.5 μm, respectively. D_f was assumed to be the diffusivity measured parallel to the fibres. All image reconstruction and fitting were performed in MATLAB (R2011b, The MathWorks, Natick, MA).

4.2.1.3 Simulations

Monte Carlo simulations were performed in Camino (Cook et al., 2006; Hall and Alexander, 2009) in order to confirm that the diffusion spectra of the phantom could be generated with known geometry and diffusivity free from any systematic bias (e.g., from hardware non-ideality) or noise. In addition, these simulations allow us to generate data across the entire spectrum without hardware limitations. The fibre phantom was represented by infinitely long, parallel cylinders with a gamma distribution of radii (mean ± SD: 17.4 ± 2.6) with the same mean and standard deviation as those of the fibres (Burcaw et al., 2013). The approximate fibre volume fraction was 0.60, which is similar to that measured from the phantom 0.587 ± 0.004 using a CPMG sequence (see Results section). The simulator placed the fibres randomly, following a specified distribution of radii, but the volume fraction was not controlled directly. Ten trials were run with different seeds to decrease any bias in the results. For example, two of the trials were discarded because the cylinder placement algorithm failed to

place many of the smaller cylinders, which resulted in an abnormally skewed radius distribution.

Diffusion gradients were applied perpendicular to the cylinder axes. Gradient amplitudes were calculated to yield a b value of 1 ms/μm^2 in order to give sufficient contrast in the simulations. A PGSE sequence with $\Delta = 800$ ms and $\delta = 1$ ms was used to sample around zero frequency. Apodized cosine oscillating gradients (Does et al., 2003) were used to minimize the encoding spectrum side lobes and were simulated at frequencies of 2, 4, ..., 10, 14, ..., 100, 150, ..., 400 Hz each with waveform durations of 500 ms. The diffusion gradients sampled narrowly about the target frequencies with a FWHM of 2 Hz. Each simulation used 250,000 time steps and 100,000 walkers and no noise was added. As the pore spaces of the phantom are within the range of sizes of the simulated EAS in Chapter 3, these parameters were assumed to be sufficient.

4.2.1.4 Forward Modelling

For forward modelling of $D_{\text{ext}}(\omega)$ using Eqs. 3.1–3.13, the fibre volume fraction $f_{\text{int,max}}$ under maximal packing density is a required parameter, but an analytic expression to calculate it for randomly packed fibres does not exist. $f_{\text{int,max}}$ is the value of f_{int} at which $1/\lambda = 0$. However, the tightest packing under random packing that Camino can simulate is much less than $f_{\text{int,max}}$ as the simulator is under the constraint that the cylinder arrangement be tile-able. To allow estimation of $f_{\text{int,max}}$, a set of simulations consisting of only PGSE scans was performed over a range of fibre fractions in the range 0.0500–0.6146 (the values are determined by the random distribution of fibre radii and the specified size of the tiled voxel) and the value of f_{int} at which $1/\lambda = 0$ was extrapolated.

Simulations were run in parallel on a computing cluster of Intel Xeon X5647 processors. The run times for the PGSE and OGSE simulations were approximately

8.5 and 42 h, respectively, at each diffusivity and tortuosity. Similar to work in Chapter 3, the signal attenuation S/S_0 at each frequency was converted to a corresponding point in the diffusion spectrum $D(\omega)$ via $S = S_0 \exp(-b(\omega)D(\omega))$, where $b(\omega) = 1$ ms/μm^2 in our simulations.

4.2.2 Results

4.2.2.1 Experiment

Images from the TE = 90 ms scan are shown in Fig. 4.3. The SNR of the $b = 0$ scans (two averages each) ranged from 64 at the shortest TR to 71 at the longest.

The signal for a region of interest containing pure water as well as another containing only the fibre bundle is plotted semi-logarithmically as a function of the TE from the CPMG experiment in Fig. 4.4. The curves show monoexponential decay as expected. The effective T_2s for pure water and the water around the fibre bundle are 774 ± 1 and 596 ± 5 ms, respectively, and f_{int} is 0.587 ± 0.004. These values are in line with the expected values (Siow et al., 2012; Fieremans et al., 2008b).

The diffusion spectra, measured with the gradients along each scanner axis, of a voxel containing pure water and another containing only the fibre bundle for TE = 90 and 110 ms are shown in Fig. 4.5.

For pure water voxels, the diffusion spectrum is constant across all frequencies. For fibre bundle voxels, 1) the diffusion spectrum measured parallel to the fibres (Slice) is similar to that of water since diffusion is expected to be free and 2) the spectra measured perpendicular to the fibres (Read and Phase) show a frequency dependence, and are similar to each other as expected for a cylindrically symmetric phantom. The ADC values measured in the slice select direction at 107, 178, 202, and 250 Hz for all scans are outliers. These frequencies could be mechanical resonances inherent to the scanner. The ADC values measured in the readout direction at the highest four frequencies are also outliers. The magnitude of these outliers is reduced

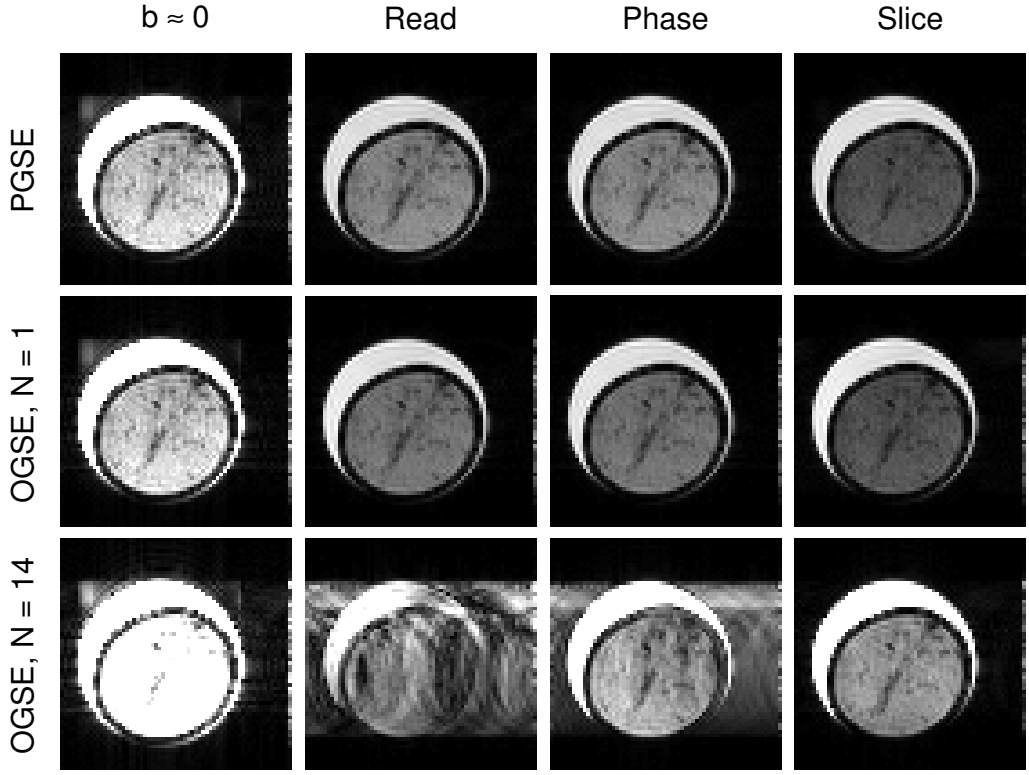


Figure 4.3: Axial images of the fibre phantom showing the water around the circular fibre bundle for three representative TE = 90 ms scans. Note the artefacts, which are consistent with eddy current artefacts (see text), in the readout and phase encoding images at the highest frequency (bottom), which used the strongest diffusion gradients. The axons run perpendicular to the page (parallel to the slice select gradient) and thus the signal attenuation is greatest for diffusion weighting along the slice select gradient. The region of interest for the fibre bundle was drawn to exclude the dark areas in the centre, which are of unknown origin. The window and level values for all images are the same.

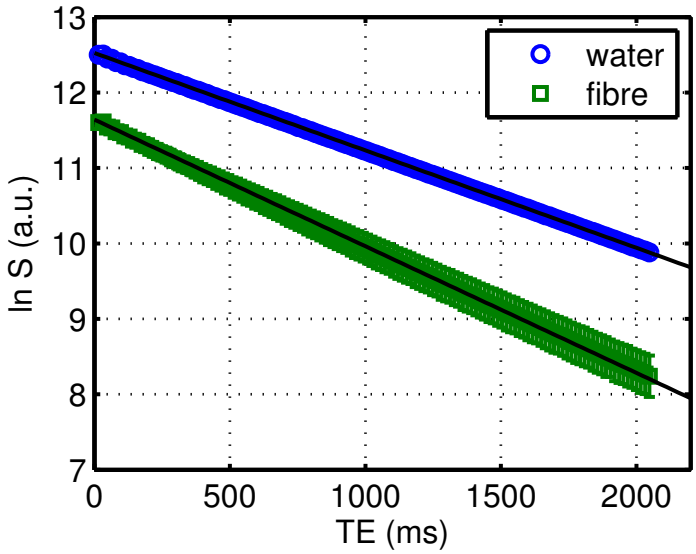


Figure 4.4: Logarithm of the measured signal (mean ± SD) from a region of interest in the fibre phantom containing pure water (circles) and only the fibre bundle (squares) using a CPMG sequence and the fitted line as a function of TE.

in the TE = 110 ms scan, which introduced an additional 10 ms between the second diffusion waveform and the readout. Although this is not proof that these outliers are driven by eddy currents that extend the diffusion gradient into the readout, the fact that they are lessened by longer TE is consistent with this hypothesis.

For forward modelling, the fibre volume fraction $f_{\text{int,max}}$ under maximal packing density is a required parameter in the model. It was extrapolated from simulations by plotting inverse tortuosity $1/\lambda$ versus fibre volume fraction f_{int} (red diamonds in Fig. 4.6). $f_{\text{int,max}}$ is the x-intercept of the curve and, for random packing, is estimated to be greater than 0.6 and less than that for square packing ($\pi/4 \approx 0.7854$). Here we assume it to be 0.7.[1] For comparison, $1/\lambda$ for hexagonally and square packed cylinders with constant radius and the low-density packing approximation given by the Maxwell–Garnett equation (Sen and Basser, 2005a) are also shown.

Figure 4.7 shows model fits and predictions (forward model with no fitting) for

[1]It is interesting to note that "randomly packed" is not easily defined. Randomly packed cylinders, if arranged in a hexagonal lattice except for one errant cylinder, will have $f_{\text{int,max}}$ much closer to that of hexagonal packing than cylinders with no resemblance to a hexagonal lattice.

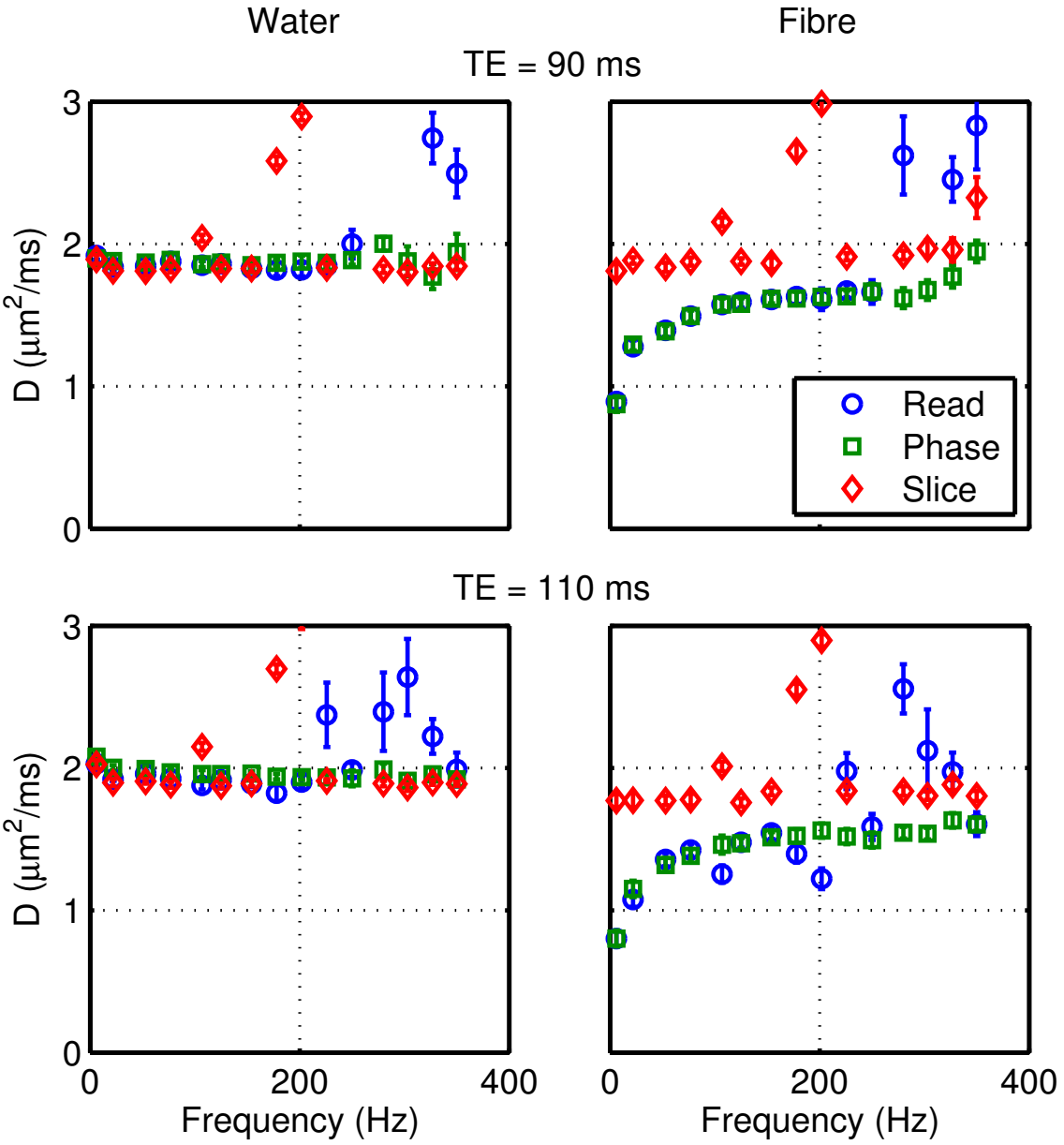


Figure 4.5: Measured $D(\omega)$ (mean $\pm$ SD) of the fibre phantom for a voxel containing pure water and another containing only the fibre bundle for TEs of 90 and 110 ms. The diffusion gradient directions (readout, phase encoding, and slice selection) are noted. The readout and phase encoding directions are perpendicular to the fibres and that of the slice selection is parallel. The same points that show outlier behaviour at TE = 110 ms are off these axes for TE = 90 ms.

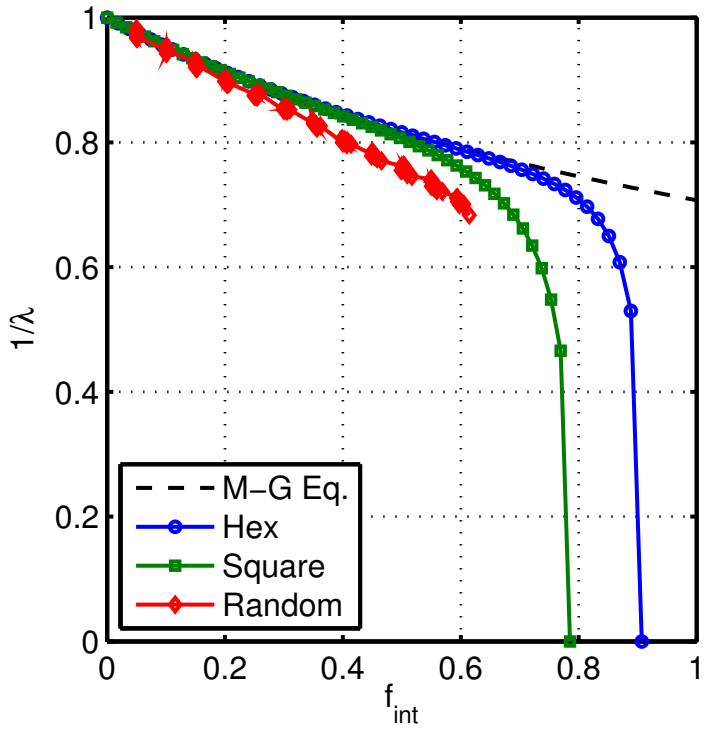


Figure 4.6: The inverse tortuosity $1/\lambda$ of hexagonally (circles) and square (squares) packed uniform cylinders and of randomly (diamonds) packed cylinders with a gamma-variate radius distribution (same mean and standard deviation as the fibres in the phantom) versus the fibre volume fraction f_{int}. The low-density packing approximation (black dashed line) given by the Maxwell–Garnett equation (Sen and Basser, 2005a) is also shown. $1/\lambda$ is plotted instead of λ in order to show the abutting case ($1/\lambda = 0$).

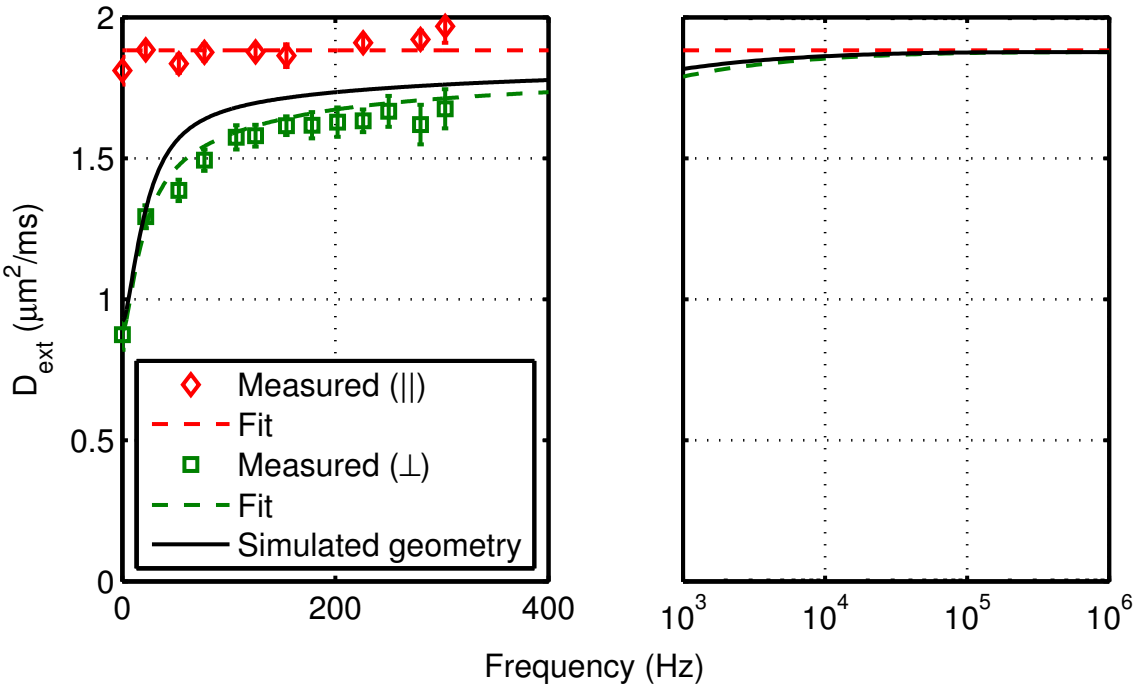


Figure 4.7: $D(\omega)$ (mean ± SD) measured parallel (diamonds) and perpendicular (squares) to the fibres in the phase encoding direction. The four outliers in the measurements parallel to the fibres were excluded to improve the fit. Overlaid are the model fits (dashed lines) and forward model prediction (solid line) from the model in Chapter 3.

the diffusion spectrum for the case with TE = 90 ms and the gradient applied along the phase encoding direction (with reduced eddy current effects). Qualitatively, the model fits the data extremely well.

The forward model (using the mean inverse tortuosity $1/\lambda = 0.70$ calculated directly from simulations and $f_{\text{int,max}} = 0.7$ extrapolated from Fig. 4.6) predicts a diffusion spectrum with slightly larger values than the measurement, which indicates that the extra-cylindrical spaces in the phantom are slightly smaller than expected.

4.2.2.2 Simulations

The placement of cylinders and radius histogram for one representative simulation and the mean simulated diffusion spectrum of the fibre phantom are shown in Fig. 4.8. The histogram shows the correct mean and standard deviation and reasonable symmetry

	$1/\lambda$	$\mu_{R,0}$ (µm)	$\sigma_{R,0}$ (µm)	R_∞ (µm)
Fit to experimental data (diffusion along phase encoding direction)				
TE = 90 ms	0.69 ± 0.02	8.1 ± 1.9	4.4 ± 2.5	3.9 ± 0.2
TE = 110 ms	0.67 ± 0.02	7.1 ± 2.2	5.1 ± 2.5	3.5 ± 0.2
Fit to mean of eight simulation runs				
	0.70 ± 0.01	9.9 ± 0.1	4.5 ± 0.2	6.3 ± 0.1
From segmentation of simulated geometry (assuming $1/\lambda = 0.7$ and $f_{\text{int,max}} = 0.7$ to calculate R_∞)				
	-	8.2 ± 0.2	6.0 ± 0.4	5.6 ± 0.1

Table 4.2: Simulated and fitted values (mean ± SD) of the model parameters for the fibre phantom. $1/\lambda$ was calculated from $D(0)$ and fixed before fitting the remaining parameters.

about the mean. The spectrum appears as expected with a small standard deviation at each frequency.

The values of the model parameters $1/\lambda$, $\mu_{R,0}$, $\sigma_{R,0}$, and R_∞ estimated from 1) fitting the measured data, 2) fitting the simulated data, and 3) segmentation of the simulated axon geometry to give $\mu_{R,\text{pore}}$ and $\sigma_{R,\text{pore}}$, the S/V and f_{int} ground truth, and calculating $1/\lambda = 0.7$ from the simulated diffusion spectrum and $f_{\text{int,max}} = 0.7$ from the x-intercept of Fig. 4.6 are listed in Table 4.2. The values show a good match across all three estimation techniques, except those for R_∞. This could be due to the dependence of R_∞ on high frequencies, which are poorly sampled in this experiment.

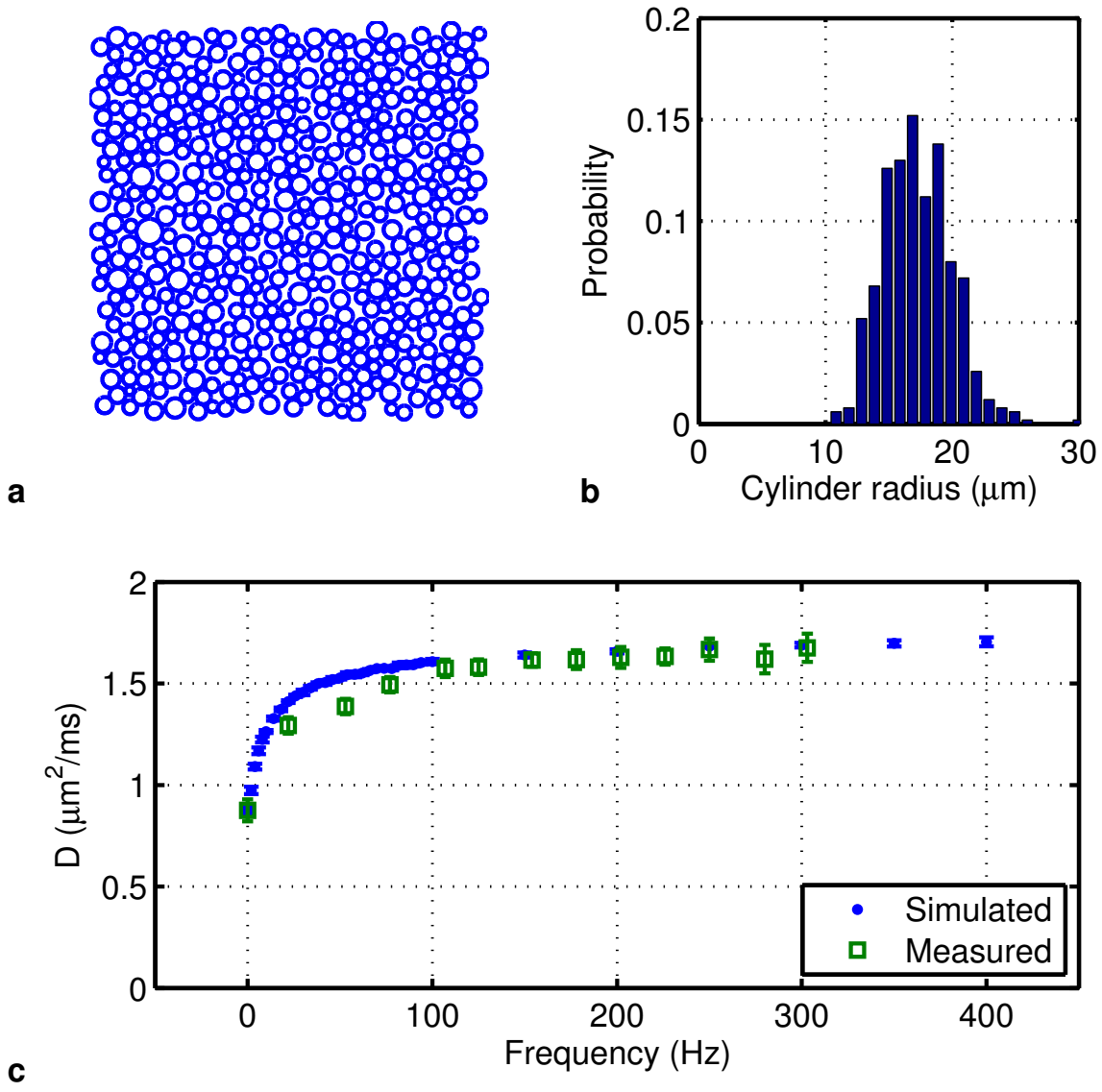


Figure 4.8: **a:** Placement of cylinders in one simulation of the fibre phantom (side length is 895 μm). **b:** The radius histogram. **c:** Simulated (mean of eight trials assuming $D_f = 1.8$ μm^2/ms) and measured diffusion spectra (mean ± SD) of the fibre phantom.

4.3 An Extra- and Intra-Axonal Space Model

In order to estimate the microstructural parameters of tissue from OGSE measurements, the significant contribution to the signal from the IAS must be included. In this section, we extend the conceptual framework introduced in Chapter 3 to include the contribution of the IAS in a two-compartment model. First, we simply add the contribution of the IAS as an additional, independent compartment to give a full model. Next, we attempt to simplify this model by relating the parameters used to describe the IAS to those used for the EAS. We expect this to be possible since a complete description of one space completely describes the other. It is also desirable to remove redundant parameters to make the model fitting more robust. Finally, this model is compared to the simulated data and microstructural parameters are estimated from fitting.

4.3.1 Full Model

This section will describe a signal model that combines the IAS and EAS diffusion spectra presented in Chapter 3. This model assumes no exchange between the IAS and EAS.

The IAS is here modelled as a collection of infinite cylinders (representing axons) with a parametric distribution of radii. The diffusion attenuation spectrum is the volume-weighted mean over the distribution of R_{int} calculated from the diffusion spectrum $D_{\text{r}}(R_{\text{int}}, \omega)$ for a single cylinder (Eq. 3.3):

$$E_{\text{int}}(\omega) = \int A(R_{\text{int}}) \exp\{-bD_{\text{r}}(R_{\text{int}}, \omega)\} dR_{\text{int}} \tag{4.1}$$

$$A(R_{\text{int}}) = \frac{F_{\text{int}}(R_{\text{int}}) R_{\text{int}}^2}{\int R_{\text{int}}^2 dR_{\text{int}}}, \tag{4.2}$$

where $F_{\text{int}}(R_{\text{int}})$ is the distribution of axon radii. We choose to use a gamma distri-

bution with unknown mean $\mu_{R,\text{int}}$ and variance $\sigma^2_{R,\text{int}}$ as the shape broadly matches that of the axon radius distribution in the corpus callosum (Assaf et al., 2008).

The EAS diffusion attenuation spectrum is given by Eq. 3.8.

Finally, we weight the IAS and EAS diffusion attenuation spectra by the IAS volume fraction f_{int} and arrive at the effective diffusion spectrum

$$E(\omega) = f_{\text{int}} E_{\text{int}}(\omega) + (1 - f_{\text{int}}) E_{\text{ext}}(\omega) \tag{4.3}$$

$$D(\omega) = -\frac{1}{b} \ln(E(\omega)). \tag{4.4}$$

Here, we highlight the differences between the IAS and EAS models. The IAS model is a summation of diffusion spectra for restricted diffusion within cylinders. The diffusion spectra assume a constant radius across all frequencies for each cylinder. The EAS model on the other hand is a linear combination of diffusion spectra for restricted diffusion within extra-axonal "pores" (see Chapter 3) and the free diffusion coefficient, which is constant across all frequencies. The extra-axonal pores have a frequency-dependent radius for each cylinder. The free diffusion coefficient accounts for the unrestricted nature of the EAS.

We expect this model to be over-parameterized due to the fact that the IAS and EAS compartments coexist in the same space and, in this simplified model, are the only compartments. It will be interesting to see in the next section whether three of the parameters above (f_{int}, $\mu_{R,\text{int}}$, and $\sigma_{R,\text{int}}$) will be sufficient to describe both compartments.

4.3.2 Simplified Model: Relation between Axon and Pore Radii

In this subsection, we relate the parameters used to describe the IAS to those used for the EAS in order to reduce the number of independent parameters in the model.

Ideally, we would seek to derive a generic, one-to-one relationship between, e.g., the characteristic radii of each compartment given the volume fraction. It is trivial to derive such relations in the case of regular packing such as square or hexagonal; however, we are not aware of such an analytic relationship in the general case of randomly distributed cylinders. Therefore, we here use simulations to explore empirical relationships between EAS and IAS.

Similar to the approach in Chapter 3, extensive Monte Carlo simulations using Camino (Cook et al., 2006; Hall and Alexander, 2009) were conducted to define the ground truth for different spectra over a wide range of geometries, but now spins were allowed to diffuse in both the IAS and EAS (but not exchange between them). IAS diffusion spectra were simulated from randomly packed, parallel, impermeable cylinders with the axon radius distributions of the genu as given by Aboitiz et al. (1992) as well as the identical geometry scaled up by factors of two and three. The EAS simulations in Chapter 3 were re-used.

The parameters f_{int}, $\mu_{R,\text{int}}$, $\sigma_{R,\text{int}}$, $\mu_{R,\text{pore}}$, and $\sigma_{R,\text{pore}}$ from the segmentation of the simulated geometry are plotted against each other in Fig. 4.9 and show their correlations. As one might expect given that the geometry was generated by specifying three parameters (f_{int} and the mean and standard deviation of R_{int}), it is apparent that from three parameters the remaining two can be arrived at through analytic relations.

When the signal attenuations from the two compartments were summed using Eq. 4.3, the following relations were found to agree well with simulated spectra.

$$\mu_{R,\text{pore}} = 0.63p \cdot \mu_{R,\text{int}} \tag{4.5}$$

$$\sigma_{R,\text{pore}} = p \cdot \sigma_{R,\text{int}}, \tag{4.6}$$

where p is the fractional separation between adjacent cylinders and given by Eq. 3.13.

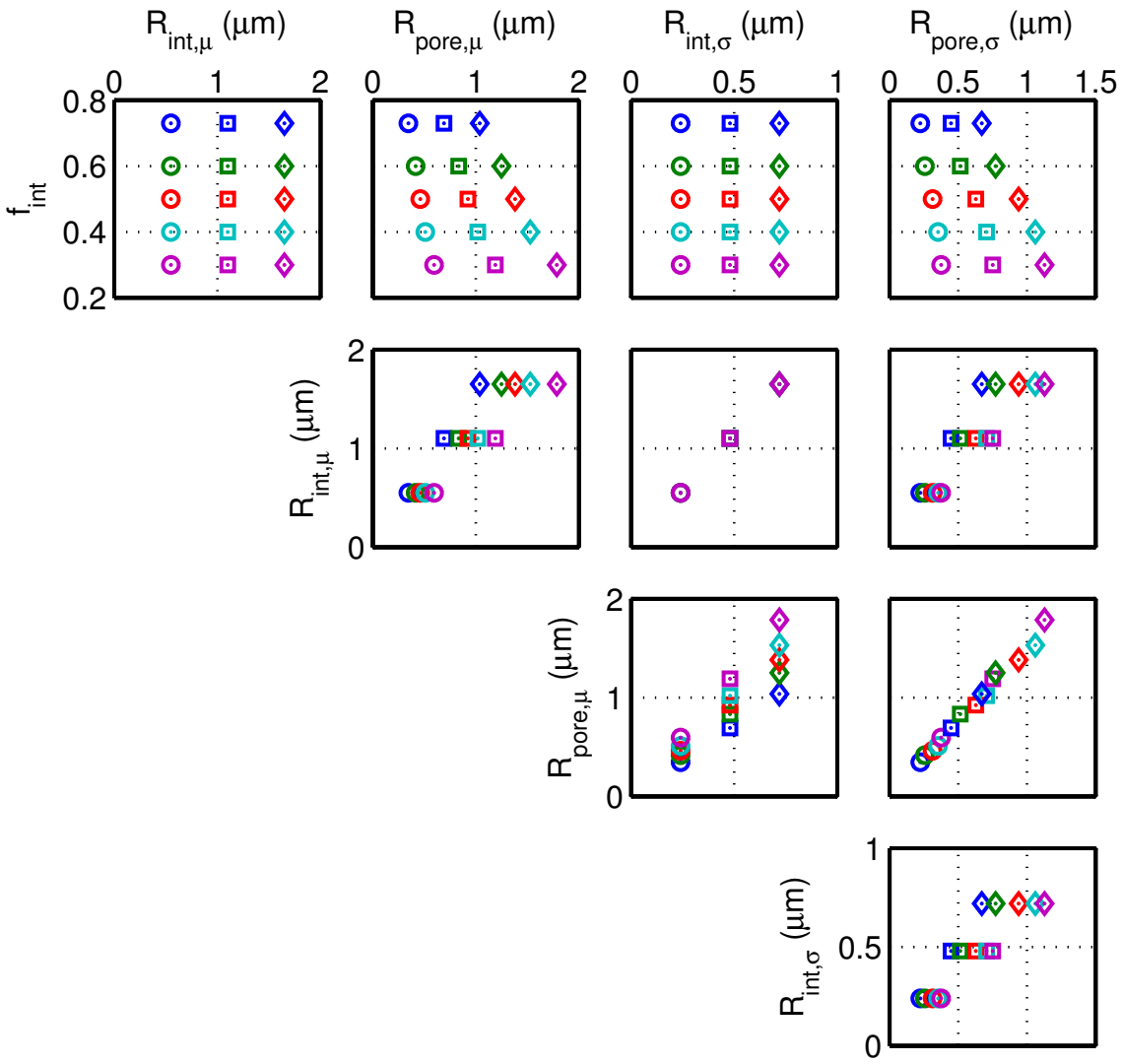


Figure 4.9: The parameters of the IAS and EAS models plotted against each other. The marker colours represent different IAS volume fractions f_{int}. The marker shapes in each subfigure, from left to right, correspond to the axon radius distributions of the genu as given by Aboitiz et al. (1992) as well as the identical geometry scaled up by factors of two and three, respectively. The marker colours in each subfigure, from top to bottom, correspond to the different f_{int}.

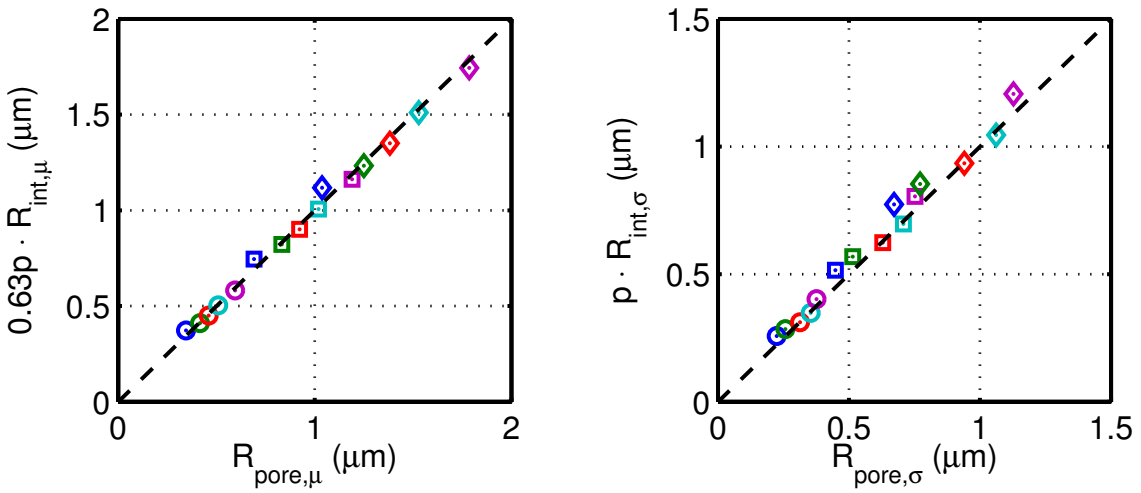


Figure 4.10: Plots of the proposed expressions for the mean and standard deviation of R_{int} as functions of R_{pore}. The markers are as in Fig. 4.9

The proposed expressions for the mean and standard deviation of R_{pore} are plotted versus those of R_{int}, respectively, in Fig. 4.10. They show good agreement.

In the EAS model presented in Chapter 3, there was no straightforward way to relate the pore surface-to-volume ratio S/V to the axon radii, which is a more meaningful quantity. However, this is possible in the combined IAS and EAS model. The pore surface area is equivalent to the axon surface area and the pore volume is the axonal volume scaled by $(1 - f_{\text{int}})/f_{\text{int}}$. Thus, S/V expressed in terms of the model parameters is given by

$$\frac{S}{V} = \frac{2}{\mu_{R,\text{int}}} \frac{1}{1/f_{\text{int}} - 1}. \tag{4.7}$$

Under the EAS model, the parameters R_0 and R_∞ could only be related to the abstract R_{pore} and difficult to interpret S/V, respectively. Now, with the combined IAS and EAS model, R_0 and R_∞ can both be related to readily interpretable parameters R_{int} and f_{int}. This combined model has potential to be more useful than either EAS or IAS model in isolation, provided data can support the estimation of the proposed model parameters.

4.3.3 Comparison of Simplified Model to Simulations

In the first subsection (4.3.1), a simple combination of an existing IAS model with the EAS model was proposed. In the previous subsection (4.3.2), geometries with specific parameters that specify the IAS (f_{int} and R_{int}) were generated and expressions were proposed to relate these to the observed EAS parameters (R_{pore}). These relations did not concern diffusion spectra, only geometry. In the current subsection, diffusion spectra of those geometries will be simulated to test whether those relations are sufficient to drive the combined IAS and EAS model for an accurate description of the entire diffusion spectrum.

4.3.3.1 Methods

This subsection compares the simplified IAS and EAS diffusion spectrum model to simulated data. This model uses 1) three fitted parameters: the axonal volume fraction f_{int} and radius distribution mean $\mu_{R,\text{int}}$ and standard deviation $\sigma_{R,\text{int}}$, 2) two directly measured parameters: $D(0)$ and the free diffusivity D_{f}, and 3) one numerically estimated parameter: the abutting cylinder volume fraction $f_{\text{int,max}}$.

Diffusion spectra with volume-weighted contributions from the IAS and EAS were calculated using Eq. 4.4 for each of the simulated cases (four values of f_{int} and three spatial scales) and were compared to the forward model predictions. Further, the estimated values of the model parameters from Bayesian fitting using the Metropolis–Hastings algorithm were compared to those derived from the geometries to assess whether it is likely to be feasible to estimate these parameters in real data.

4.3.3.2 Results

The forward model predictions of the simulated geometries are plotted in Fig. 4.11. They show excellent agreement over all simulated geometries.

The fitted values for the model parameters f_{int}, $\mu_{R,\text{int}}$, and $\sigma_{R,\text{int}}$ are displayed

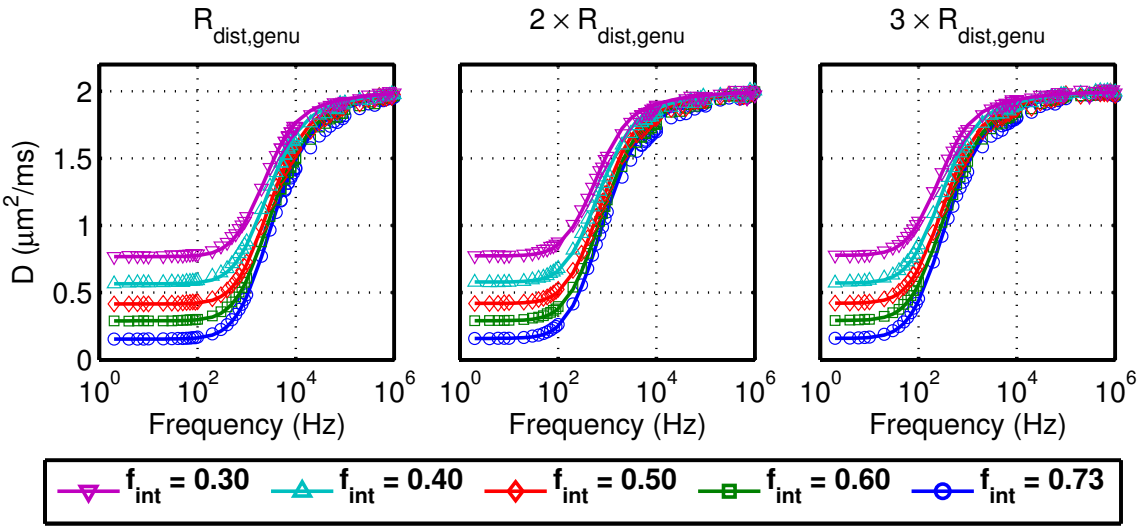


Figure 4.11: Simulated (markers) and predicted (lines) $D(\omega)$ for randomly packed cylinders over a range of five cylinder volume fractions f_{int} and cylinders with radius distributions that are one, two, and three times those of axons in the genu (left to right).

in Fig. 4.12. All of the fitted parameters show a consistent bias. The percentage misestimations (mean $\pm$ SD) are 17 $\pm$ 4%, -14 $\pm$ 9%, and 11 $\pm$ 2%, respectively.

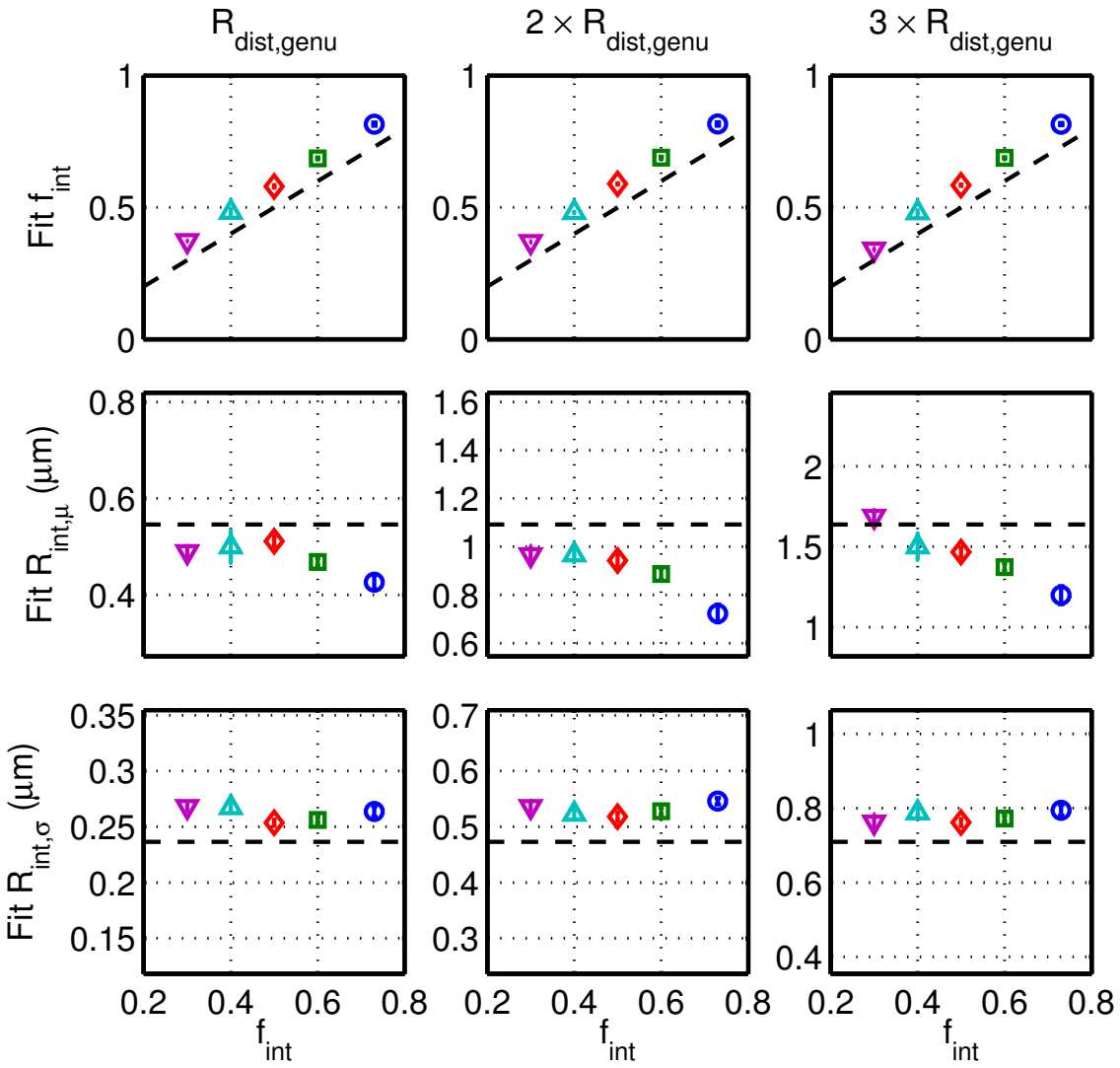


Figure 4.12: Fitted values for f_{int}, $\mu_{R,\text{int}}$, and $\sigma_{R,\text{int}}$. The dashed lines indicate the expected values calculated from the underlying geometry using the model. The y-axis limits for $\mu_{R,\text{int}}$ and $\sigma_{R,\text{int}}$ are $\pm$ 50% of the expected values.

4.4 Brain Specimen Experiment

This section presents comparisons of the model to measurements made on an extracted brain tissue sample to determine whether the model can be used to extract microstructural parameters from real tissue. Potential challenges include tissue structural complexity, eddy currents, susceptibility artefacts, sample heating, and limited b value and oscillating gradient frequencies.

4.4.1 Methods

4.4.1.1 Experiment

Cuboidal pieces ($\approx$ 1 mL each) containing the genu, mid body, and splenium of the corpus callosum were excised by a neuropathologist from a porcine brain perfusion fixed with formalin. The specimens were wrapped in gauze and placed into individual 15-mL conical centrifuge tubes filled with phosphate buffered saline (PBS) for 13 h; the gauze prevented movement within the tubes. The PBS increases the T_2 decay constant of the specimen to physiological values by replacing the fixative, which has short T_2 (D'Arceuil et al., 2007), and allows longer TE to be used. Gadolinium (sometimes added to decrease the T_1 decay constant and improve SNR efficiency) was not added since there would have been less than 5% SNR efficiency improvement while T_2 would fall significantly from $\approx$ 35 ms to $\approx$ 30 ms, assuming 1 mM gadolinium and a TR of 2000 ms (D'Arceuil et al., 2007).

The PBS was then replaced by Fluorinert (FC-3283, 3M Specialty Materials, St. Paul, Minnesota, USA). Fluorinert is a liquid that does not generate ^{1}H MR signal and is susceptibility matched to tissue. It is used to displace free PBS and air bubbles in the specimen. PBS would reduce the dynamic range of the receiver available for the tissue signal and air bubbles would cause susceptibility artefacts. Fluorinert is also a low viscosity fluid, which allows more thorough penetration of the specimen than

higher viscosity proton-signal-free liquids also found in literature such as Fomblin (Solvay S.A., Brussels, Belgium).

The genu and mid body specimens were placed in the magnet with fibres parallel to the bore (and the field); the splenium specimen was placed with fibres perpendicular due to positioning constraints of the specimen in the conical tube. A CPMG sequence (number of slices = 1; field of view = 20 mm × 20 mm; slice thickness = 1 mm; TR = 3000 ms; TE = 5.5, 11, ..., 174 ms; matrix = 128 × 128; readout bandwidth = 1628 Hz/px; averages = 1) was used to measure the T_2 decay constant of the genu.

Diffusion-weighted images were acquired using a similar diffusion gradient sequence as for the fibre phantom. The waveforms before the refocusing pulse were approximately 30 ms in duration (due to a smaller T_2 value than the phantom) and the diffusion gradients sampled about the target frequencies with a FWHM of 14 Hz.

A b value of 0.6 ms/μm^2 was chosen to achieve sufficient diffusion contrast given the TE and gradient amplitude constraints. A PGSE sequence with $\Delta = 59$ ms and $\delta = 1$ ms was used to sample around zero frequency. At the highest frequency, $b = 0.52$ ms/μm^2 was used due to gradient amplitude constraints. The diffusion gradient parameters and TR, which was set proportional to duty cycle to prevent bore heating, are given in Table 4.3. Scans with $b = 0$ were unexpectedly found to have lower signal that those with $b = 0.6$ ms/μm^2 for unknown reasons. The signal from the $b = 0$ scan was compared with those from PGSE scans with $b = (0.06, 1.5, 6, 13.5, 24) \times 10^{-3}$ ms/μm^2 (Fig. 4.13). All of the low, non-zero b-value scans were found to have higher signal than the $b = 0.6$ ms/μm^2 scan as expected. Thus, at each frequency, the $b = 0$ scan was replaced by an attenuated ($b = 0.0015$ ms/μm^2) version of each diffusion-weighted scan applied along the slice selection direction. Each $b = 0.0015$ ms/μm^2 scan was followed by scans with diffusion weighting in the readout, phase encoding, and slice selection directions.

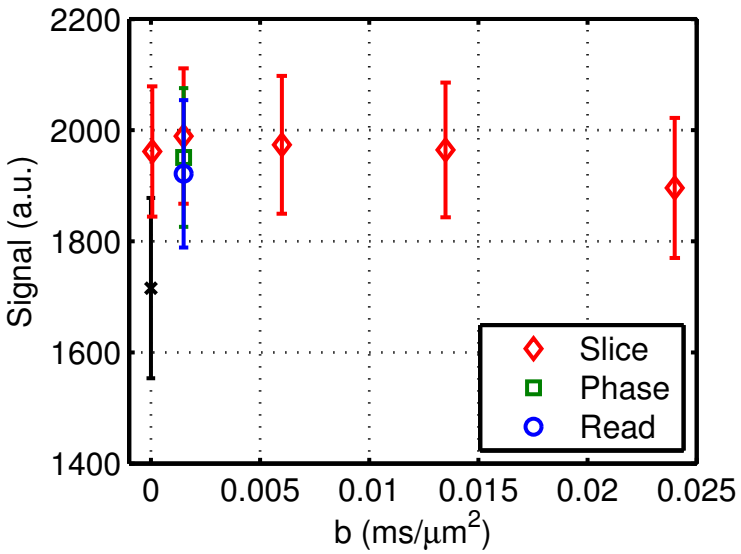


Figure 4.13: Signal from $b = 0$ and $b = (0.06, 1.5, 6, 13.5, 24) \times 10^{-3}$ ms/μm^2 PGSE scans of the splenium sample showing anomalously low at $b = 0$ (black ×), but not at other small b values (other markers). In order to avoid this anomaly when measuring diffusion spectra, the $b = 0$ scan was replaced by a $b = 0.0015$ ms/μm^2 scan applied along the slice selection direction.

The other scan parameters are: number of slices = 1, field of view = 20 mm × 20 mm, slice thickness = 1 mm, TE = 74 ms, matrix = 64 × 64, readout bandwidth = 98 Hz/px, and averages = 3 (each set of scans was repeated three times giving effectively nine averages). The TE was chosen to be approximately twice the T_2 value measured by the CPMG sequence in order to increase the amount of time available for the diffusion gradients, which is important for measuring at low frequencies and achieving higher b values. The OGSE scans were also ordered such that the mean duty cycle of adjacent scans varied as little as possible (i.e., the order was $N = 9, 1, 8, 2, 7, 3, 6, 4, 5$).

4.4.1.2 Analysis

The image reconstruction and model fitting methods were those used for the fibre phantom with the addition of one additional fitted parameter $D(0)$. This additional parameter increases the robustness of the f_{int} fit value against inaccuracies in the measured $D(0)$ to which f_{int} is very sensitive. The initial values for f_{int}, $D(0)$, $\mu_{R,\text{int}}$,

Gradient scheme	Cycles per waveform N	Zero padding (ms)	Invert second waveform?	Frequency (Hz)	TR (ms)
PGSE	-	0	N	0	1200
OGSE	1	0	Y	29	1200
	2	2.0	N	69	1625
	3	0.6	N	101	2050
	4	0	N	132	2475
	5	0.8	Y	172	2900
	6	0.4	Y	203	3325
	7	0	Y	234	3750
	8	0.6	N	273	4175
	9	0.3	N	304	4600

Table 4.3: Diffusion gradient parameters used for the specimens.

and $\sigma_{R,\mathrm{int}}$ were set to 0.7, 1.5 times the measured $D(0)$, 1 µm, and 0.5 µm, respectively. $f_{\mathrm{int,max}}$ was determined numerically for the distributions reported in literature (Aboitiz et al., 1992) that correspond to the specimens. D_{f} was assumed to be the mean across all three specimens of $D(\omega)$ measured parallel to the fibres at the highest frequency to avoid the influence of hindered diffusion at lower frequencies. This is a strong assumption, to which we will return in the Discussion section.

4.4.2 Results

Images from the genu, mid body, and splenium scans are shown in Figs. 4.14–4.16, respectively, and are generally artefact free. The SNR of the $b = 0$ scans (nine averages each) calculated from manually drawn regions of interest in the corpus callosum ranged from 159 at the shortest TR to 224 at the longest.

The signal for a region of interest containing the genu is plotted semi-logarithmically as a function of the TE from the CPMG experiment in Fig. 4.17. The curve shows biexponential decay as expected. Fitting a biexponential to the data yields a component with a signal fraction of 92% and $T_2 = 28$ ms and the balance of the signal fraction with $T_2 = 108$ ms. The relative values of these signal fractions are compara-

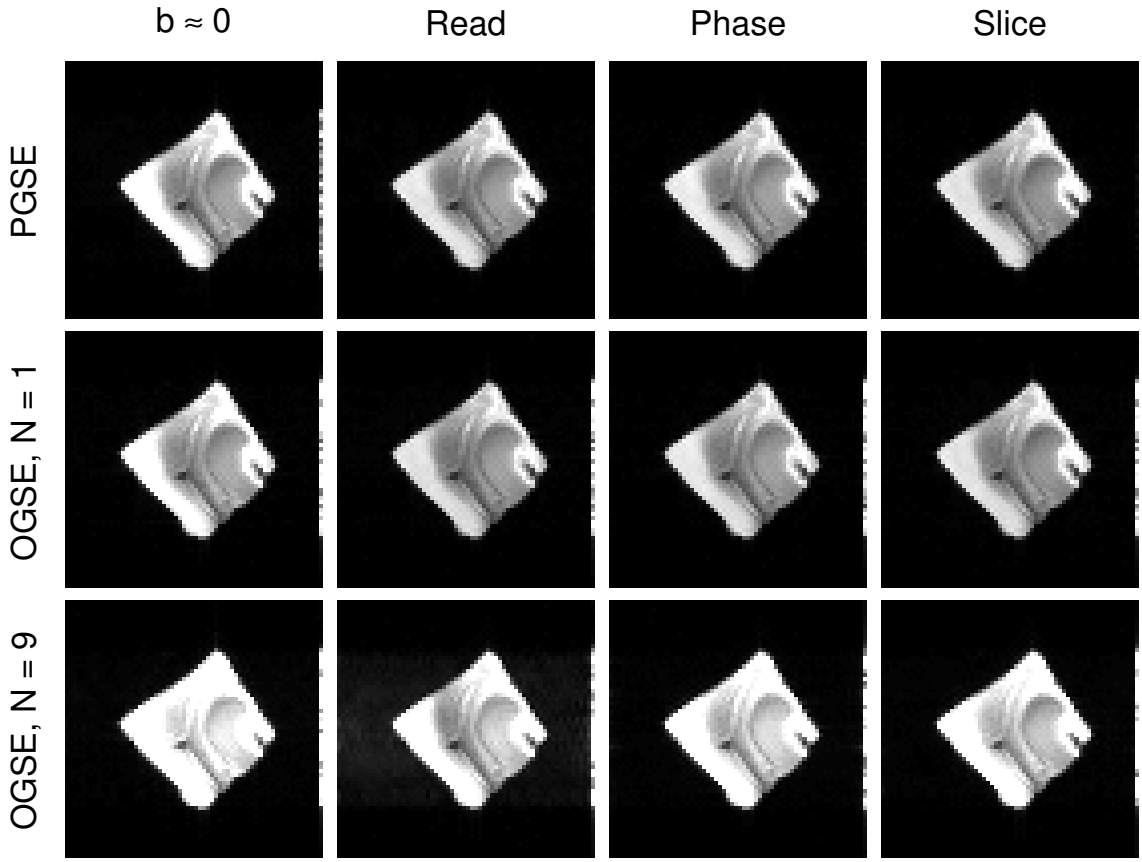


Figure 4.14: Axial images of the genu specimen for three representative scans. The axons run perpendicular to the page (parallel to the slice select gradient). The signal attenuation is less obvious than for the fibre phantom because the diffusivity of the specimens is an order of magnitude less. The window and level values for all images are the same.

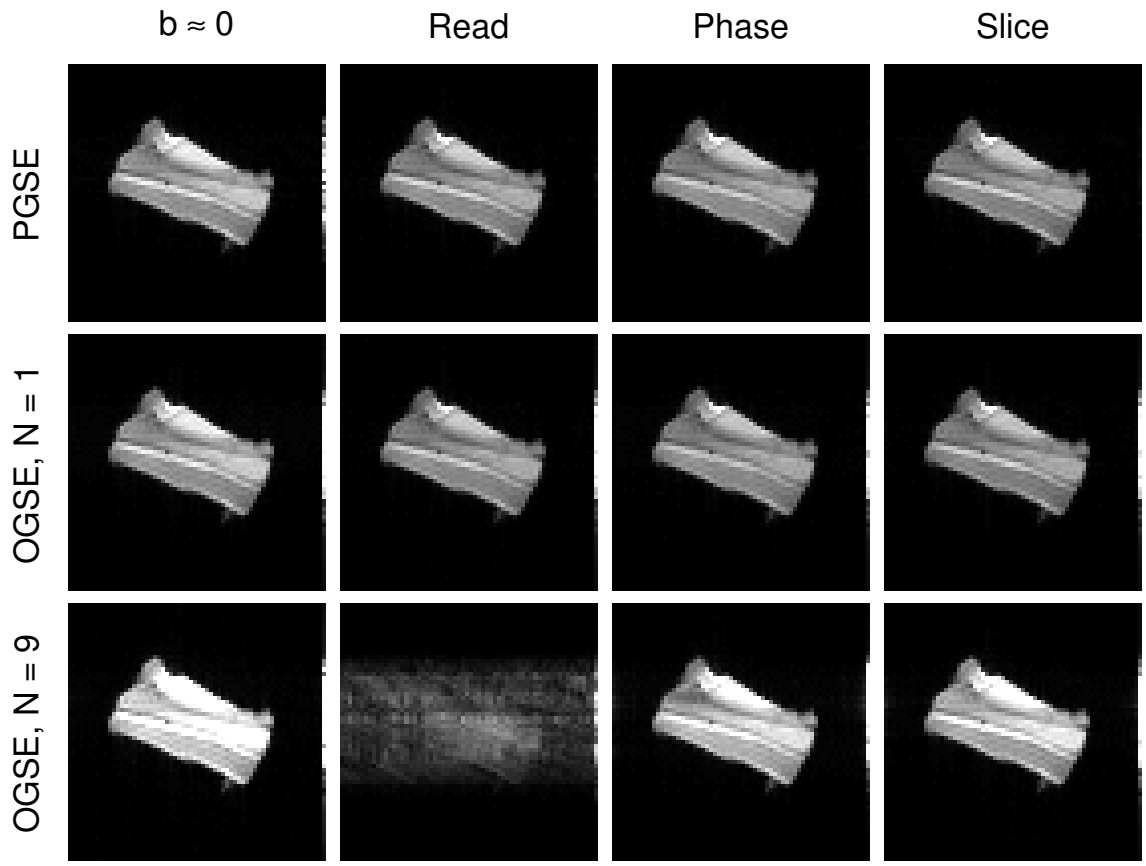


Figure 4.15: As Fig. 4.14, but for the mid body specimen.

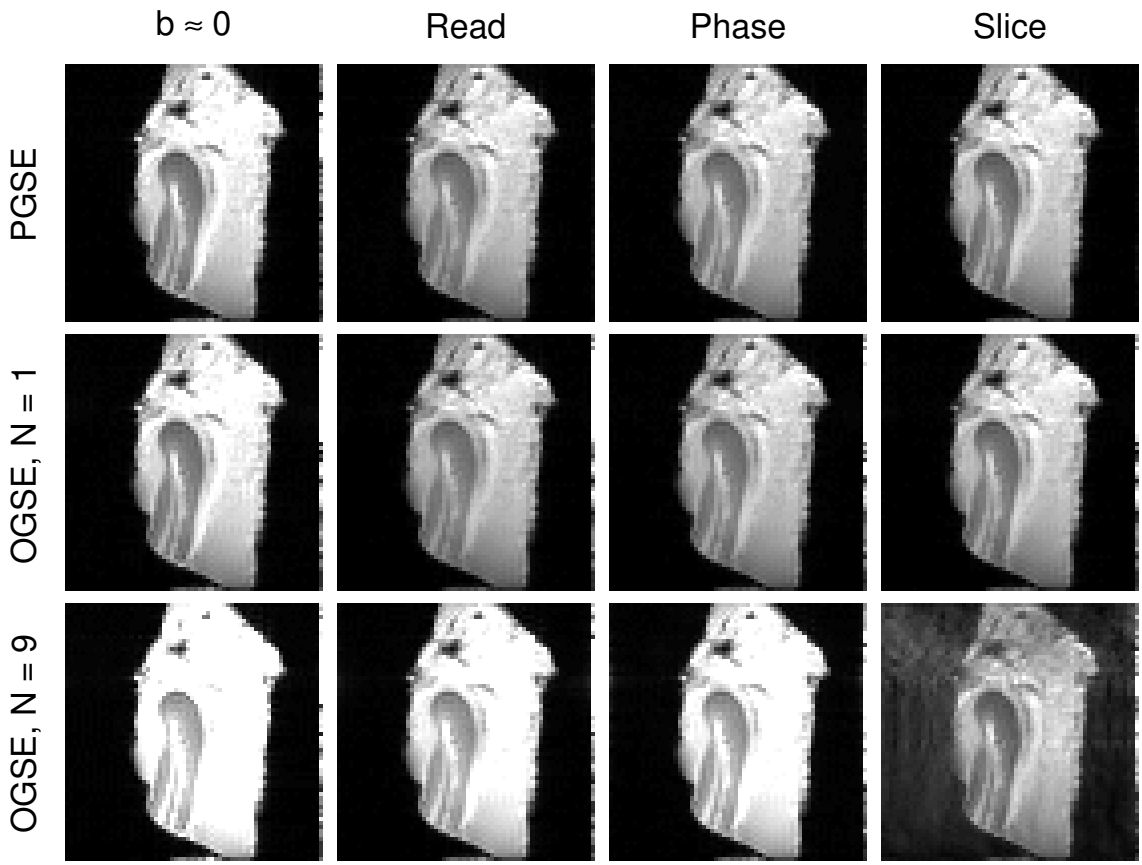


Figure 4.16: As Fig. 4.14, but for the splenium specimen.

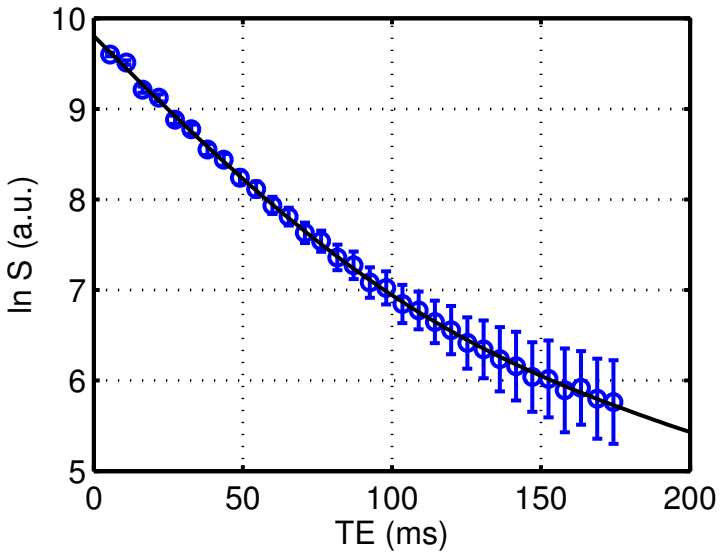


Figure 4.17: Logarithm of the measured signal (mean ± SD) using a CPMG sequence from the genu specimen and the fitted biexponential as a function of TE.

ble with those of the 1) IAS and EAS and 2) cerebrospinal fluid (CSF), respectively, measured in healthy volunteers at 1.5 T (upper left subfigure in Fig. 2 of MacKay et al. (1994)). Although there is no CSF in our specimens, this compartment could be areas of PBS experiencing free diffusion. This reference also measures a component due to myelin, but our measurement is not sensitive to that signal fraction because our TE is much longer than the T_2 of myelin. The effective T_2 matches the expected value (D'Arceuil et al., 2007).

The diffusion spectra measured with the gradients on each scanner axis for the three specimens are shown in Fig. 4.18. The diffusion spectra measured in the slice selection direction (parallel to the axons for all specimens) have unexpected frequency dependence; they were hypothesized to be frequency independent and have a value of D_f. This is indicative of hindrances to diffusion and could possibly be caused by structures in the axoplasm, the axon narrowing at the nodes of Ranvier, or the glia. For the splenium specimen, which was the only sample with axons perpendicular to the magnetic field, the spectrum measured in the slice selection direction (parallel to the axons) is not monotonically increasing. The susceptibility-mismatch induced

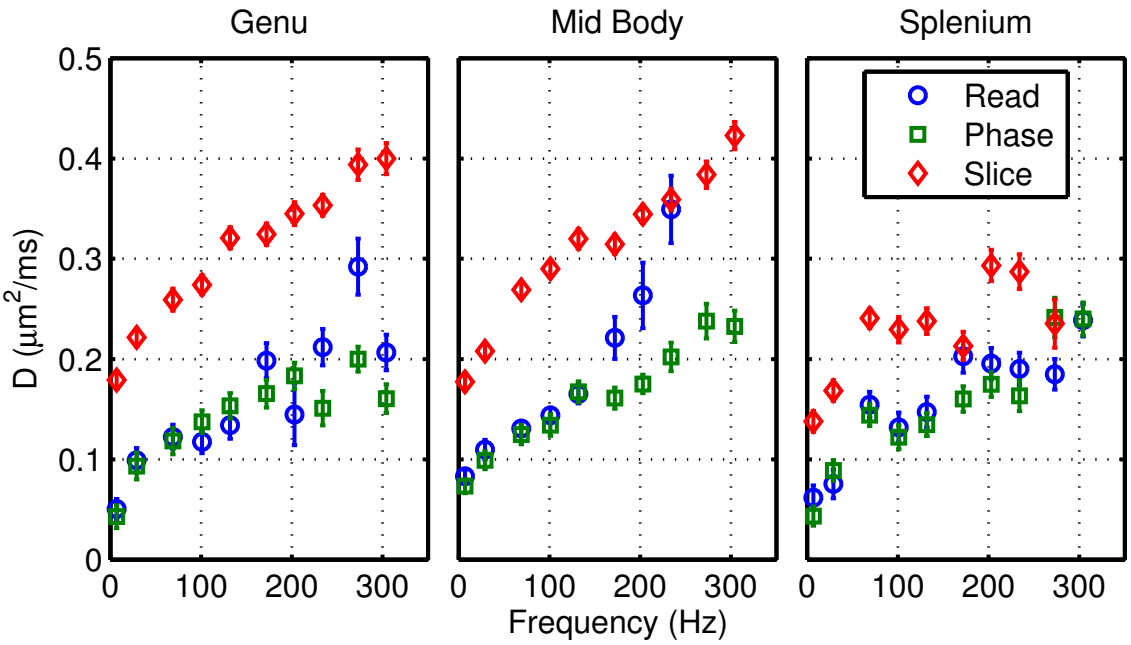


Figure 4.18: Measured $D(\omega)$ of the specimens. The diffusion gradient directions (readout, phase encoding, and slice selection) are noted. The slice selection direction was parallel to the axons for all specimens.

gradients created by the myelin at an angle to the magnetic field could possibly cause increased field inhomogeneity and the non-monotonic diffusion spectrum (Lee et al., 2010). The other two specimens have axons parallel to the field and do not show this anomaly. D_f will be calculated from the mean of the measured $D(\omega)$ at the highest frequency of the genu and mid body specimens, which are uncorrupted.

For the mid body specimen, the spectrum measured in the readout direction (perpendicular to the axons) increases dramatically at the two highest frequencies to values beyond even those in the spectrum measured parallel to the fibres. The reason for this is unclear.

The model fits for the diffusion spectrum perpendicular to the fibres are shown in Fig. 4.19 for the case with the gradient applied along the phase encoding direction to reduce eddy current effects. Qualitatively, the model fits the data well. The fitted values of f_int, λ, $\mu_{R,\mathrm{int}}$, and $\sigma_{R,\mathrm{int}}$, and R_∞ are given in Table 4.4 and reasonably match those found in literature.

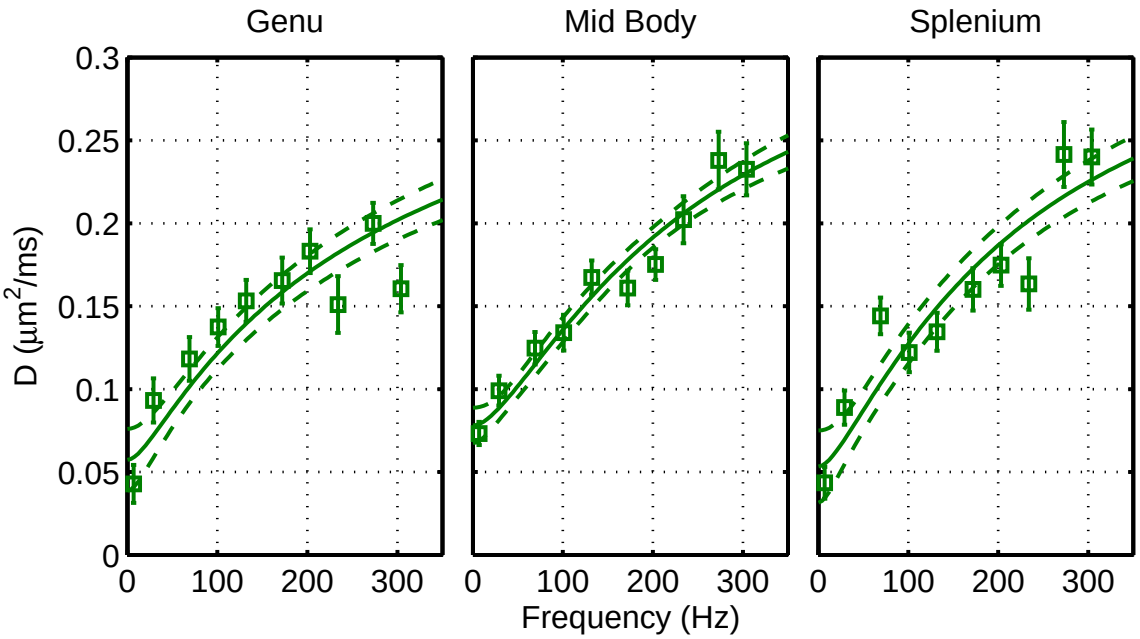


Figure 4.19: $D(\omega)$ (mean ± SD) measured (markers) perpendicular to the axons in the specimens. Overlaid are the means of the Markov Chain Monte Carlo fitted posterior distributions (solid lines) and their standard deviations (dashed lines).

	f_{int}	λ	$\mu_{R,\text{int}}$ (μm)	$\sigma_{R,\text{int}}$ (μm)
Genu				
Fitted	0.78 ± 0.07	2.1 ± 1.8	0.33 ± 0.21	0.30 ± 0.06
From literature	0.74 ± 0.01	1.8 ± 0.2	0.55	0.24
Mid body				
Fitted	0.74 ± 0.04	1.2 ± 0.1	0.62 ± 0.22	0.31 ± 0.08
From literature	0.74 ± 0.01	-	0.72	0.42
Splenium				
Fitted	0.80 ± 0.08	2.7 ± 2.2	0.56 ± 0.29	0.34 ± 0.10
From literature	0.74 ± 0.01	2.0 ± 0.2	0.63	0.28

Table 4.4: Fitted (mean ± SD) and literature values (Nicholson, 2001; Aboitiz et al., 1992) of the model parameters for the specimens. $D(0)$ is measured perpendicular to the axons and fitting was performed for the diffusion spectrum along the phase encoding direction to minimize eddy current effects.

4.5 Discussion

In this chapter, we present the experimental verification of the EAS diffusion spectrum model from Chapter 3 with a fibre phantom, extend this model to include the IAS, and test it with experiments on ex vivo specimens. The extended model continues to assume that axons are perfectly cylindrical, parallel, and impermeable and ignores glial cells. Note that the EAS diffusion spectrum may be sufficient to infer the microstructural geometry. However, the extended model is necessary because signal from the IAS and EAS are measured simultaneously. Below we discuss alternative models, insights gleaned from our experiments, and further experiments that should avoid the limitations of our current experiments.

4.5.1 Alternative Models

There exist models that use pulsed diffusion gradients to estimate axon diameter. Our model recovers a distribution of axon radii. Likewise, the AxCaliber model also assumes a gamma distribution of axon diameters and has been successfully applied to fixed nerve specimens (Assaf et al., 2008) and the brain in vivo (Barazany et al., 2009). Another model (Alexander et al., 2010) estimates an axon size index that is the mean axon diameter weighted by the cross-sectional area of axons. This model is comprised of IAS, EAS, and CSF compartments. A CSF compartment would be straightforward to add to our model as a third compartment and would help account for partial volumes containing CSF, which may be significant in non-corpus callosum voxels.

There also exist diffusion spectrum-based models. For instance, the analytic expression for the diffusion spectrum of spins between parallel plates (Stepišnik, 1993) has been used as a one-compartment model to fit data from rat hippocampal specimens (Portnoy et al., 2012). Also, a two-compartment model assumes cylindrical

axons, but a flat EAS diffusion spectrum has been proposed (Xu et al., 2009). The work in this chapter uses a more complicated two compartment model, using our novel description of the EAS compartment, to estimate the axonal volume fraction and size distribution, but ignoring exchange between the IAS and EAS.

4.5.2 Insights from Experiments and Future Work

This subsection will highlight several unexpected effects found during the experiments and ways in which they can be further investigated. First, the reasons for hindered diffusion parallel to axons will be considered. Second, the difference in measured and fitted $D(\omega = 0)$ will be briefly discussed. Third, the unexpected shape of the diffusion spectrum measured parallel to the axons will be examined with special consideration of the noisy spectrum (of the splenium specimen) acquired with axons perpendicular to the main magnetic field.

4.5.2.1 Hindered Diffusion "Parallel" to Axons

$D(\omega)$ parallel to the fibres is expected to be constant across all frequencies as no hindered or restricted diffusion is expected. However, in the case that $D(\omega)$ measured parallel to the fibres is frequency dependent (red diamonds in Fig. 4.18). However, with the fanning of axons, even in the corpus callosum and internal capsule (Mikula et al., 2012), there is hindrance to diffusion even in the "parallel" direction. This is potentially the physical basis for the frequency-dependent diffusion spectra measured parallel to the corpus callosum axons in this work and in literature (Aggarwal et al., 2012; Baron and Beaulieu, 2014). Instead of making D_f into a model parameter, which would introduce fitting instability due to measurements at insufficiently high frequency that very weakly constrain the value of D_f, D_f was assumed to be $D(\omega)$ measured parallel to the fibres at the highest frequency, which should be the least affected by hindered diffusion.

4.5.2.2 Mismatch between Measured and Fit $D(0)$

f_{int} is very sensitive to $D(0)$ as f_{int} is mainly driven by the EAS attenuation, which is dominated by $D(0)$. Fitting only the three parameters f_{int}, $\mu_{R,\text{int}}$, and $\sigma_{R,\text{int}}$ while using directly measured values of $D(0)$ yielded abnormally low f_{int} values (≈ 0.5–0.6). However, fitting for $D(0)$ in addition to these three parameters yielded much more reasonable f_{int} values (≈ 0.75). It is unknown why $D(0)$ might have an erroneous value. It is possibly due to exchange between the IAS and EAS since the diffusion time of the PGSE scan, 59 ms, is half of the estimated EAS water residence time of ≈ 120 ms (but still far below that of IAS water of ≈ 550 ms; Quirk et al. (2003)). Longer residence times in the IAS should lead to $D(0)$ being biased lower than the model fits as seen in Fig. 4.19. In contrast, the lowest frequency OGSE scan has a waveform period of 30 ms and should be less sensitive to exchange effects.

There is another more remote possibility for the difference in the measured and fit $D(0)$. It could be due to the non-negligible width (14 Hz FWHM) of the diffusion spectrum sampling function of the PGSE scan. The frequency of the PGSE scan was taken to be 7 Hz (the frequency of the sampling function barycentre) instead of 0 during fitting to better account for this width, although this difference in frequency assignment is likely negligible. Further, if the barycentre frequency of the $D(0)$ sampling function were of even higher frequency than the assumed 7 Hz, the value of $D(0)$ should be biased higher than the model fits, not lower as seen in Fig. 4.19.

4.5.2.3 Noisy $D(\omega)$ with Axons Perpendicular to the Field

The diffusion spectra measured parallel to axons of the genu and mid body specimens had the monotonic increase expected for spectra. However, the spectrum for the splenium specimen showed significantly more scatter (red diamonds in Fig. 4.18). The main difference was that the former two scans had axons parallel to the magnetic field, whereas the latter had axons perpendicular. Axons are covered in myelin, which has

a susceptibility mismatch with water and will cause local magnetic field distortions when at an angle to the main field. Further studies with the samples at varying angles to the main field could confirm this effect. The diffusion spectra perpendicular to the axons for the splenium sample do not appear to be affected. Perhaps this effect only confounds diffusion measured parallel to axons. This effect should also be less at lower field strengths, which offers another avenue for testing.

The diffusion spectra measured parallel to the axons are not uniform across frequencies, whereas the spectrum for the fibre phantom was constant. This indicates hindrance parallel to axons (e.g., from the axoplasm, narrowing of the axons at the nodes of Ranvier, glia, etc.). Glia may also affect the diffusion spectrum perpendicular to axons because they may have a different length scale from that of axons. Longer diffusion time scans, as will be described in the next chapter, could potentially better characterize hindrances over spatial scales on the order of tens of microns. Electron (Mikula et al., 2012) and polarized light (Axer et al., 2011) microscopy could also independently elucidate the presence of axial hindrance.

4.6 Conclusions

This chapter has presented experimental measurements of diffusion spectra from a axonal phantom to support the EAS model from Chapter 3. This chapter has also extended that model to include the signal contribution from the IAS. Axonal volume fraction and size distribution estimated from experimental data from brain specimens, which matched literature values, were presented. This four-parameter model can potentially be used to estimate the geometric properties of cylindrical structures such as those found in white matter.

Chapter 5

Measurements at Long Diffusion Time

5.1 Introduction

The preceding chapters introduced models for microstructure that consider diffusion from the viewpoint of translational frequency of particles using oscillating gradients. Although such information was useful for accessing the small length scales of axon diameter and extra-axonal spaces, oscillating gradients are not easily applied at low translational frequencies (with long effective diffusion times) since waveforms longer than the T_2 relaxation time would be required. The longest diffusion times using PGSE and OGSE sequences applied to the specimens in Chapter 4 were 59 and 9 ms, respectively; the latter is calculated using Eq. 13 in Parsons et al. (2003). This chapter considers measurements of diffusivity at longer diffusion times, a regime that has not typically been investigated in brain tissue. Such measurements can potentially be used to study tissue properties associated with longer time scales such as slow exchange phenomena or diffusion that is hindered or restricted over larger length scales.

A related motivation for measuring diffusion at long time scales is in trying to

understand and model diffusion in the direction parallel to axons. Several studies showed that surprisingly complex patterns of diffusion occur along axons. For instance, OGSE experiments presented in Chapter 4 as well as in literature (Aggarwal et al., 2012; Baron and Beaulieu, 2014) show a frequency dependence of the axial diffusivity. Similarly, experiments using multi-shell approaches (multiple b values) have also shown that diffusion along axons does not follow a simple monoexponential form (Alexander et al., 2010). Yet, and as noted throughout this thesis, white matter is often idealized as parallel cylinders of infinite length. In such systems, the diffusivity when measured parallel to the cylinder axes is modelled as free diffusivity, which does not account for the experimental data.

In this chapter, we present some new observations from in vivo experiments of diffusion with long diffusion times. We fit this data using a model of white matter microstructure that has been proposed by Stanisz et al. (1997) to model excised nerve tissue. The model is deliberately complex, comprising several compartments (with different sizes and diffusivities) as well as exchange, and serves as a starting point that allows us to investigate several nested sub-models in order to determine the minimal set of assumptions that we would require to accurately describe the in vivo data. Our experiments use stimulated echoes as a more viable alternative to PGSE and OGSE (not used in this chapter) for measuring diffusion at long time scales, and we therefore start with a brief introduction to this technique.

5.1.1 STEAM Sequence

When measurements are desired at diffusion times significantly longer than the T_2 relaxation time of water, PGSE sequences give measurements with unusably low SNR. The stimulated echo acquisition mode (STEAM, also known as pulsed gradient stimulated echo or PGSTE) diffusion sequence (Merboldt et al., 1991) was developed to allow measurements with diffusion times longer than those practically accessible

with the spin echo.

The STEAM sequence stores the transverse magnetization, which has been diffusion encoded, as longitudinal magnetization which experiences T_1 relaxation, but not T_2 (Fig. 5.1). In a STEAM sequence with Stejskal–Tanner diffusion gradients, RF pulses with flips angles of 90° are placed immediately after the first diffusion gradient and before the second; there is no refocusing pulse as the two 90° pulses achieve the same effect. The first 90° pulse stores a portion of the transverse magnetization as longitudinal and the second restores it to the transverse plane. As T_1 relaxation is slower than T_2, this allows a longer diffusion time. However, there is a signal penalty of 50% compared to the spin echo sequence since not all the transverse magnetization contributes to the STEAM echo. (A rigorous derivation can be found in section II A of Larson et al. (2012).)

Figure 5.2 shows calculated signal from STEAM and spin echo diffusion sequences using typical white matter properties at 3 T and clinical scanner gradient strengths. Spin echo gives more signal when Δ is below approximately 75 ms, which is also approximately the T_2 of white matter. Conventional pulse sequences that are used to estimate the diffusion tensor at 3 T typically do not significantly exceed this diffusion time. Here, we aim to investigate diffusion at time scales equal to or larger than the T_2 of white matter, a regime where STEAM outperforms PGSE by a significant margin (Fig. 5.2).

5.1.2 Three-Pool Model

We propose to use an analytic model presented by Stanisz et al. (1997) to estimate microstructural parameters in white matter. The model comprises parameters for diffusivity in and around idealized axons and glial cells, accounting for their size, volume fraction, and membrane permeability. Although there are many other models available to fit data with diffusion weighting from pulsed gradients (Nilsson et al.,

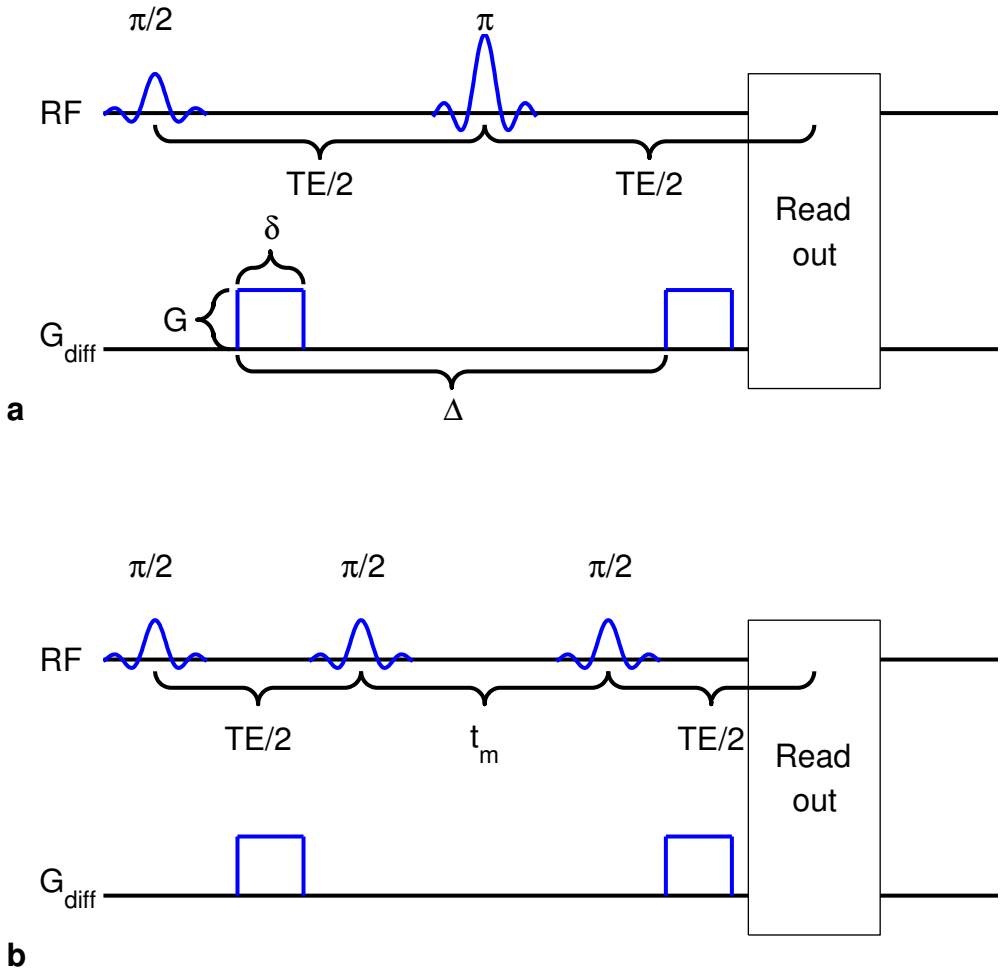


Figure 5.1: Pulse diagrams for (**a**) PGSE and (**b**) STEAM. During the mixing time t_{m} the magnetization undergoes T_1 decay, whereas T_2 decay occurs during the TE/2 periods.

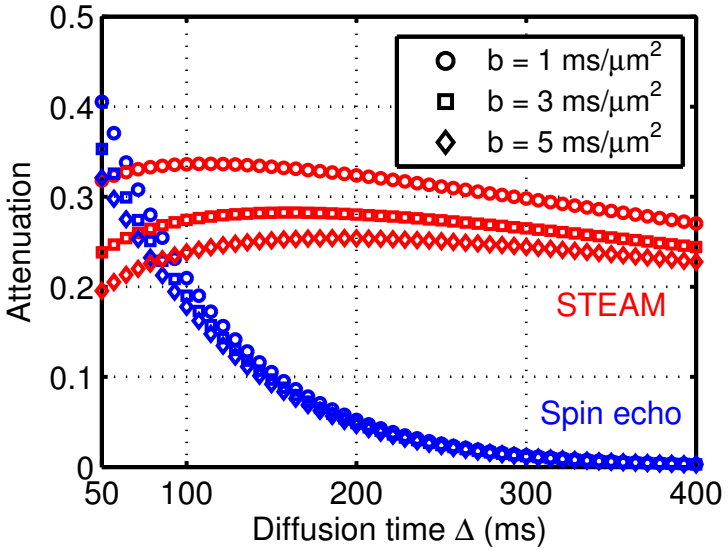


Figure 5.2: Calculated signal attenuation for STEAM and spin echo sequences (including the 50% signal penalty incurred with STEAM, but not accounting for any diffusion effects, which would induce the same effects in both sequences). PGSE is calculated as $\exp(-\mathrm{TE}/T_2)$, and STEAM as $0.5\exp(-t_\mathrm{m}/T_1)\exp(-\mathrm{TE}/T_2)$. Above approximately 75 ms, STEAM gives more signal. Typical values of $T_1 = 840$ ms and $T_2 = 70$ ms of in vivo white matter at 3 T and clinical scanner maximum gradient of $G = 40$ mT/m were used. Imaging gradients and hardware imperfections (e.g., finite slew rate, eddy currents, etc.) were ignored.

Symbol	Parameter
D_{int}	Intracellular diffusivity
$a_{\text{T}}(\perp)$	Ellipsoid minor axis
$a_{\text{T}}(\|\|)$	Ellipsoid major axis
a_{S}	Sphere diameter
V_{T}	Ellipsoid volume fraction
V_{S}	Sphere volume fraction
P_{T}	Ellipsoid permeability
P_{S}	Sphere permeability
D_{ext}	Extracellular diffusivity

Table 5.1: Three-pool model parameters.

2013), we chose this model because it includes a wide variety of parameters and therefore serves here as a starting point for searching model space. The model has nine independent parameters and was originally used to fit data at very high b values, only achievable on animal MR scanners.

The full model includes diffusion within and the exchange of magnetization between three pools while ignoring T_1 and T_2 signal decay and assuming uniform proton density in all compartments. The three pools are 1) axons, which are idealized as parallel, prolate ellipsoids (denoted with the subscript T); 2) glial cells, which are modelled as spheres (subscript S); and 3) the extracellular space (subscript E). The model parameters are given in Table 5.1 and the model compartments are shown schematically in Fig. 5.3. Note that D_{ext} is the free diffusion coefficient in the EAS and is different from the EAS diffusion spectrum $D_{\text{ext}}(\omega)$ in the previous chapters.

The following system of rate equations governs the time-dependent magnetization $M(t)$ between the three compartments.

$$\frac{dM_{\text{T}}(t)}{dt} = -q^2 D_{\text{T}}^{\text{app}} M_T(t) - k_{\text{TE}} M_{\text{T}}(t) + k_{\text{ET}} M_{\text{E}}(t) \tag{5.1}$$

$$\frac{dM_{\text{S}}(t)}{dt} = -q^2 D_{\text{S}}^{\text{app}} M_S(t) - k_{\text{SE}} M_{\text{S}}(t) + k_{\text{ES}} M_{\text{E}}(t) \tag{5.2}$$

$$\frac{dM_{\text{E}}(t)}{dt} = -q^2 D_{\text{E}}^{\text{app}} M_E(t) + k_{\text{TE}} M_{\text{T}}(t) + k_{\text{SE}} M_{\text{S}}(t) - (k_{\text{ET}} + k_{\text{ES}}) M_{\text{E}}(t), \tag{5.3}$$

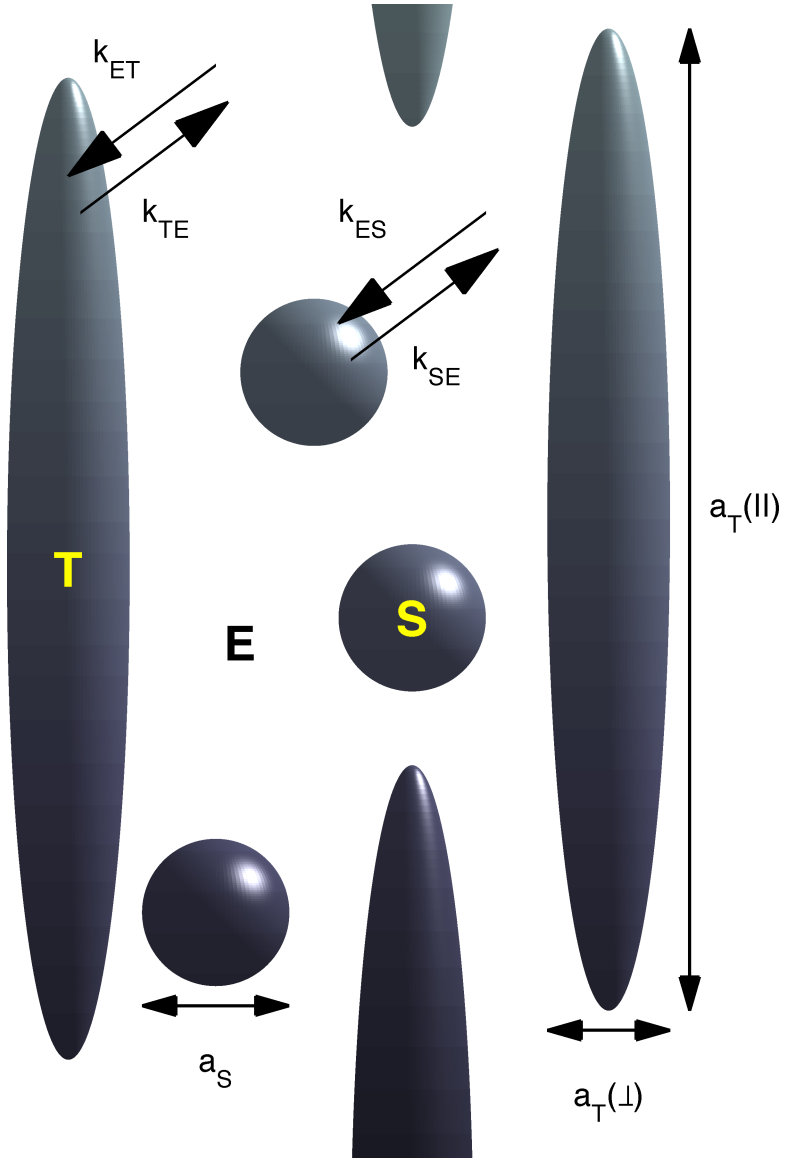


Figure 5.3: Schematic diagram of the three-pool model showing ellipsoid (T), sphere (S), and extracellular (E) compartments with dimensions a and exchange rate constants k.

where q is the magnitude of the $\mathbf{q}$ vector as defined in Eq. 2.11, $D_{\mathrm{X}}^{\mathrm{app}}$ is the apparent diffusivity for compartment X, and k_{XY} are rate constants for magnetization exchange from compartment X to Y (Fig. 5.3). There is no direct exchange between ellipsoids and spheres. The above differential equations can easily be integrated analytically using a matrix formalism, giving values for the magnetisations at all time points.

The intracellular apparent diffusivities $D_{\mathrm{T}}^{\mathrm{app}}$ and $D_{\mathrm{S}}^{\mathrm{app}}$ for the ellipsoidal and spherical compartments, respectively, are different because these compartments can have different restricted dimensions. Also, since the ellipsoid is anisotropic, it has different apparent diffusivities $D_{\mathrm{T}}^{\mathrm{app}}(||)$ and $D_{\mathrm{T}}^{\mathrm{app}}(\perp)$ for the cases where the diffusion gradient is parallel and perpendicular to the major axis, respectively.

The apparent diffusivities are defined from $A = \exp(-bD^{app})$, where A is the signal attenuation along a given diffusion direction and b is the b value. Signal attenuation for restricted diffusion can be written analytically in simple geometric cases such as parallel plates, cylinders, or spheres. Here we use expressions for restriction between parallel plates separated by a distance l, which represents the average restricted distance (related to the main dimensions of the ellipsoids and spheres in the model). In this case, the apparent diffusion coefficient is written (Tanner and Stejskal, 1968):

$$D^{\mathrm{app}} = -\frac{1}{b}\ln\left\{2\frac{1-\cos(ql)}{(ql)^2} + 4(ql)^2\sum_{n=1}^{\infty}\frac{1-(-1)^n\cos(ql)}{[(ql)^2-(n\pi)^2)]^2}\exp\left[-(n\pi)^2 D_{\mathrm{int}}\frac{\Delta}{l^2}\right]\right\}. \tag{5.4}$$

The average restricted distance for spheres and ellipsoids can be approximated as:

$$l_{\mathrm{T}}(||) = a_{\mathrm{T}}(||) \tag{5.5}$$

$$l_{\mathrm{T}}(\perp) = a_{\mathrm{T}}(\perp)/2 \tag{5.6}$$

$$l_{\mathrm{S}} = a_{\mathrm{S}}/2. \tag{5.7}$$

Diffusion within the ECS is modelled as hindered diffusion with apparent diffusivity $D_{\mathrm{E}}^{\mathrm{app}}$ which does not have a restricted distance since the ECS is not an enclosed space on a subvoxel length scale. It is related to the ECS diffusivity D_{ext} and tortuosity through Eq. 2.4, which is recast here using the relevant variables:

$$\lambda = \sqrt{D_{\mathrm{ext}}/D_{\mathrm{E}}^{\mathrm{app}}}. \tag{5.8}$$

The tortuosity is anisotropic and approximated by a function of the ellipsoid and sphere volume fractions V_{T} and V_{S}, respectively, and the normalized hindrance length L along the three dimensions. L is based on effective medium theory for electrical conductivity in porous media (Sen et al., 1981), which has been used as an analogue for other transport processes such as diffusion (Latour et al., 1994; Sen and Basser, 2005a). The extracellular apparent diffusivity is given by

$$D_{\mathrm{E}}^{\mathrm{app}} = D_{\mathrm{ext}} V_{\mathrm{E}}^{\alpha}, \tag{5.9}$$

where α is a geometric correction factor that has been estimated by Sen et al. (1981). In the case of a mixture of ellipsoids and spheres, this factor is given by:

$$\alpha = \frac{\frac{1}{2}V_{\mathrm{S}} + \frac{L}{1-L}V_{\mathrm{T}}}{V_{\mathrm{S}} + V_{\mathrm{T}}}. \tag{5.10}$$

In the above equation, the factor L depends on the orientation of gradient with respect to the ellipsoids as:

$$L(||) = \ln\left[\frac{2a_{\mathrm{T}}(||)}{a_{\mathrm{T}}(\perp)} - 1\right]\left[\frac{a_{\mathrm{T}}(\perp)}{a_{\mathrm{T}}(||)}\right]^2 \tag{5.11}$$

$$L(\perp) = \frac{1}{2}(1 - L(||)). \tag{5.12}$$

Now we turn to the exchange component of the model and the rate constants k_{TE}

and k_{SE} that govern the exchange from the ellipsoids and spheres, respectively, to ECS. The rate constants are given by the product of the permeability and surface-to-volume ratio of the restricted compartments (Chen and Springer, 1981):

$$k_{\mathrm{TE}} = P_{\mathrm{T}} \frac{3}{a_{\mathrm{T}}(||)} \left[1 + \frac{a_{\mathrm{T}}(||)}{a_{\mathrm{T}}(\perp)} \frac{\sin^{-1} \xi}{\xi} \right] \tag{5.13}$$

$$k_{\mathrm{SE}} = P_{\mathrm{S}} \frac{6}{a_{\mathrm{S}}}, \tag{5.14}$$

where $\xi^2 = 1 - [a_T(\perp)/a_T(||)]^2$.

The remaining rate constants k_{ET} and k_{ES} for exchange from the ECS to ellipsoids and spheres, respectively, are given by magnetization balances at steady state (at $t = 0$):

$$k_{\mathrm{ET}} M_{\mathrm{E}}(0) = k_{\mathrm{TE}} M_{\mathrm{T}}(0) \tag{5.15}$$

$$k_{\mathrm{ES}} M_{\mathrm{E}}(0) = k_{\mathrm{SE}} M_{\mathrm{S}}(0). \tag{5.16}$$

Finally, since each compartment is assumed to have equal proton density, initial magnetizations are proportional to the volume fraction of each compartment, i.e.,

$$M_{\mathrm{T}}(0) = V_{\mathrm{T}} \tag{5.17}$$

$$M_{\mathrm{S}}(0) = V_{\mathrm{S}} \tag{5.18}$$

$$M_{\mathrm{E}}(0) = 1 - V_{\mathrm{T}} - V_{\mathrm{S}}. \tag{5.19}$$

The signal attenuations $E(\mathbf{q}(||), \Delta)$ and $E(\mathbf{q}(\perp), \Delta)$ for diffusion parallel and perpendicular, respectively, to the ellipsoids are the sum of the magnetizations in each

compartment at time $t = \Delta$, i.e.,

$$E(\mathbf{q}(||), \Delta) = M_{\mathrm{T}}(|\mathbf{q}(||)|, \Delta) + M_{\mathrm{S}}(|\mathbf{q}(||)|, \Delta) + M_{\mathrm{E}}(|\mathbf{q}(||)|, \Delta) \tag{5.20}$$

$$E(\mathbf{q}(\perp), \Delta) = M_{\mathrm{T}}(|\mathbf{q}(\perp)|, \Delta) + M_{\mathrm{S}}(|\mathbf{q}(\perp)|, \Delta) + M_{\mathrm{E}}(|\mathbf{q}(\perp)|, \Delta). \tag{5.21}$$

The model as presented above describes signal attenuation parallel and perpendicular to axons separately. It is useful to have one equation to describe the attenuation with diffusion gradients at arbitrary angles to the axons, as will be the case with our measurements on tissue. If we assume that displacements parallel and perpendicular to the tissue are independent, then the attenuation for an arbitrary $\mathbf{q}$ with respect to the normalized ellipsoid major axis $\hat{\mathbf{u}}$ is given by the product of attenuations parallel and perpendicular as shown in Assaf et al. (2004):

$$E(\mathbf{q}, \Delta) = E(\mathbf{q}(||), \Delta)E(\mathbf{q}(\perp), \Delta), \tag{5.22}$$

where

$$\mathbf{q}(||) = (\mathbf{q} \cdot \hat{\mathbf{u}})\hat{\mathbf{u}} \tag{5.23}$$

$$\mathbf{q}(\perp) = \mathbf{q} - \mathbf{q}(||). \tag{5.24}$$

This concludes our description of the Stanisz model. We now describe our in vivo experimental set-up and show how well we can use the above model to describe the experimental data.

5.2 Methods

5.2.1 Measurements

In order to test the predictions from the model, experiments were performed with a variety of long Δ scans. Phantoms, both isotropic and anisotropic, were scanned to validate the pulse sequence and healthy volunteers were scanned to determine the applicability of the model in vivo. All scans were performed on a wide-bore 3T clinical scanner (MAGNETOM Verio, Siemens AG, Healthcare Sector, Erlangen, Germany) using a vendor prototype 2D DTI sequence and EPI readout.

5.2.2 Scan Parameters

A STEAM protocol with constant q, but varying Δ, was chosen such that all scans would have the same diffusion sensitivity to spin displacement allowing the probing of diffusion time effects alone. A nominal q value of 0.08 rad/μm was chosen such that the scans would have a mean b value of 0.9 ms/μm^2, which balances the needs for sufficient diffusion contrast and SNR. The minimum Δ was the shortest allowed by the sequence and the maximum was the longest that would yield sufficient SNR. An additional spin echo diffusion-weighted scan with the same diffusion parameters as the STEAM scan with the shortest Δ was performed for comparison purposes. Thirty diffusion directions were used and separate $b = 0$ scans were acquired for each STEAM and spin echo scan. The diffusion parameters are summarized in Table 5.2, where the nominal b-values listed are those entered on the scanner.

The full b matrix (found in the DICOM file header), which includes the diffusion-weighting contributions from both the Stejskal–Tanner and imaging gradients, was used instead of the nominal b values entered at the scanner console to calculate the ADC from the signal. This was suggested by the vendor and has been shown to correct for biases in the calculation of the ADC arising from not accounting for

Parameter	Value
δ (ms) / G (mT/m)	20 / 15
Δ (ms)	STEAM: 70, 100, 150, 200, 250, 300
	Spin echo: 70
Nominal b (ms/μm^2)	STEAM: 0.405, 0.595, 0.915, 1.235, 1.555, 1.875
	Spin echo: 0.405

Table 5.2: Diffusion parameters for the STEAM and spin echo experiments. The nominal b value is that entered at the scanner console. Where there is more than one nominal b value, they correspond to the respective Δ values.

imaging gradients, especially at long Δ (Sigmund et al., 2014). The q value used for modelling was calculated from the largest eigenvalue of the b matrix and Eqs. 2.9 and 2.11.

5.2.3 Isotropic Phantoms

Two isotropic phantoms were scanned to ensure that the sequence did not exhibit directionally dependent biases (e.g., due to poor gradient calibration, scanner b-value miscalculation, etc.) and to ensure that our b-value calculation was correct. Liquid dish soap (Fairy Original, Procter & Gamble, Surrey, United Kingdom) was chosen as it exhibits free diffusion and agar (Sigma-Aldrich Co. LLC, Gillingham, United Kingdom) as it consists of microscopic compartments (Rahbani et al., 2013) and may exhibit hindered diffusion. The soap was scanned in its original container. The agar phantom consisted of 2 L water, 1.0 g agar, 1.0 g sodium chloride, and 0.4 mL Dotarem (Guerbet Laboratories Ltd., Solihull, United Kingdom; to shorten the T_1 relaxation time) in a plastic sphere. The phantoms were placed in a 32-channel head coil and axial slices were acquired (parameters in Table 5.3).

5.2.4 Anisotropic Phantom

The anisotropic phantom (Fieremans et al., 2008b) used in Chapter 4 was again used to represent idealized axon bundles. This phantom provides a simple system to

Parameter	Agar, liquid soap, and volunteers	Fibre phantom
TR (ms)	STEAM: 4200, 5100, 6600, 8100, 9600, 11,100 Spin echo: 4100	2400
TE (ms)	STEAM: 63.2 Spin echo: 104.8	112.4
Number of slices	30	6
Slice spacing	0	0
Field of view (mm × mm)	190 × 190	50 × 25
Slice thickness (mm)	2	10
Matrix	96 × 96	32 × 16
Phase partial Fourier factor	6/8	0
Parallel imaging	GRAPPA ($R = 2$)	None
Averages	2	32

Table 5.3: Non-diffusion parameters for the STEAM and spin echo experiments. The TR values correspond to the respective Δ values in Table 5.2.

ensure the sequence behaved as expected without the confounding factors of complex anatomy or motion. The phantom was placed with fibres parallel to the magnet bore on a 4-cm diameter surface coil and axial slices were acquired (parameters in Table 5.3). A surface coil was necessary to achieve sufficient SNR. The TR and TE are the minimum possible that could be applied to all the scans and the number of averages was determined by the available scan time (≈ 5 h). The slice thickness was also increased compared to the other protocols to maximize SNR. A 1-L bag of saline solution was placed over the phantom for the duration of the scan to allow sufficient signal for prep scans.

5.2.5 Healthy Volunteers

Five healthy volunteers were scanned (three males; mean age ± SD: 26 ± 3). A 32-channel head coil was used and an oblique imaging plane parallel to the body of the corpus callosum prescribed such that the entire corpus callosum would be imaged (≈ 50 min). The TR values were chosen to minimize scan time (parameters in Table 5.3).

5.2.6 Analysis

The FMRIB Software Library (FSL; Smith et al. (2004)) was used to process the data. For the in vivo scans only, 1) the effects of simple subject motion and eddy currents were corrected by affine registration to a reference $b = 0$ image using *eddy_correct* and 2) the skull was removed from the image using *bet* (Smith, 2002). For all scans, a diffusion tensor was fitted to each voxel with *dtifit* using the direction-specific b values calculated from the b matrices (Basser et al., 1994a).

The ADC along the principal diffusion direction (PDD) was plotted as a function of 1) the diffusion direction for the isotropic phantoms and 2) the square of the cosine of the angle between the diffusion direction and fibre orientation for the fibre phantom and in vivo scans. For the in vivo scans, fractional anisotropy (FA) thresholds of 0.2, 0.5, and 0.8 were applied before calculating the ADC to explore potential partial volume effects such those created by crossing fibres. These thresholds are not expected to be necessary for the fibre phantom, as it should contain no crossing fibres.

Bayesian fitting of the in vivo signal attenuation with FA > 0.8 (to exclude areas of crossing fibres) to the model was performed. The Metropolis–Hastings algorithm was used with uninformative, uniform priors and with the fit initialized by the result of non-linear least squares. The non-linear least squares analysis initial values for the full three-pool model are given in Table 5.4.

Since the data may not support the nine-parameter full model, five simplifications were also tested (Table 5.5). The dimensional appropriateness for the measured data was compared both qualitatively (by plotting fits) and quantitatively using the BIC given by Eq. 3.16 (Schwarz, 1978).

All ADC calculations and fitting were performed in MATLAB (R2011b, The MathWorks, Natick, MA).

Parameter	Initial value
D_{int} (μm^2/ms)	1
$a_{\text{T}}(\perp)$ (μm)	1
$a_{\text{T}}(\|\|)$ (μm)	20
a_{S} (μm)	1
V_{T}	0.4
V_{S}	0.2
P_{T} (10^{-3} cm/s)	1
P_{S} (10^{-3} cm/s)	2
D_{ext} (μm^2/ms)	2

Table 5.4: Non-linear least squares analysis initial values for the full three-pool model.

Model	Description	Number of free parameters	Free parameters
1	Three pool, permeable (ellipsoid, sphere, and EAS)	9	D_{int}, $a_{\text{T}}(\perp)$, $a_{\text{T}}(\parallel)$, a_{S}, V_{T}, V_{S}, P_{T}, P_{S}, D_{ext}
2	Three pool, impermeable (ellipsoid, sphere, and EAS)	7	D_{int}, $a_{\text{T}}(\perp)$, $a_{\text{T}}(\parallel)$, a_{S}, V_{T}, V_{S}, D_{ext} ($P_{\text{T}} = P_{\text{S}} = 0$)
3	Two pool, permeable (ellipsoid and EAS)	6	D_{int}, $a_{\text{T}}(\perp)$, $a_{\text{T}}(\parallel)$, V_{T}, P_{T}, D_{ext} ($V_{\text{S}} = 0, P_{\text{S}} = 0$)
4	Two pool, impermeable (ellipsoid and EAS)	5	D_{int}, $a_{\text{T}}(\perp)$, $a_{\text{T}}(\parallel)$, V_{T}, D_{ext} ($V_{\text{S}} = 0, P_{\text{T}} = P_{\text{S}} = 0$)
5	Two pool, permeable (infinite cylinder and EAS)	5	D_{int}, $a_{\text{T}}(\perp)$, V_{T}, P_{T}, D_{ext} ($V_{\text{S}} = 0, P_{\text{S}} = 0$)
6	Two pool, impermeable (infinite cylinder and EAS)	4	D_{int}, $a_{\text{T}}(\perp)$, V_{T}, D_{ext} ($V_{\text{S}} = 0$, $P_{\text{T}} = P_{\text{S}} = 0$)

Table 5.5: Summary of models fitted to the STEAM data.

5.3 Results

5.3.1 Measurements

5.3.1.1 Isotropic Phantoms

The ADCs of the agar and liquid soap phantoms are plotted as a function of the diffusion direction in Fig. 5.4. The minor variations in the ADCs are less than 5% and characteristic of the gradient system (Dr. Robert Frost, private communication). The $\Delta = 300$ ms agar scan is an outlier and a likely cause is noise rectification; it has significantly lower signal than all the other curves. Thus, the relative ADC values corresponding to each series do not appear to correlate with Δ. These measurements indicate that there are generally no systematic biases with diffusion direction or Δ, so long as the signal is sufficiently above the noise floor. The SNR of one $b = 0$ scan (i.e., without averaging) ranged from 31 at the shortest Δ to 5 at the longest for agar and from 39 to 7 for liquid soap.

5.3.1.2 Anisotropic Phantom

The ADC values for the fibre phantom are plotted as a function of the angle between diffusion direction and fibre orientation in Fig. 5.5a. The dependence of ADC parallel to the fibres on Δ could be due to fibres interdigitating within each, relatively thick, 10-mm slice, which would cause hindrance to diffusion. The signal attenuation is plotted in Fig. 5.5b and, as there is no rectification, indicates that the noise floor has not been reached. The SNR of one $b = 0$ scan ranged from 28 at the shortest Δ to 14 at the longest.

Comparing STEAM to spin echo, we observed that the ADC measured by spin echo is 10–20% lower (i.e., less signal attenuation) than that measured by the STEAM scan with the same q and Δ. This was not evident with the isotropic phantoms, so this could be due field inhomogeneity caused by the fibres coupled with 90° pulses

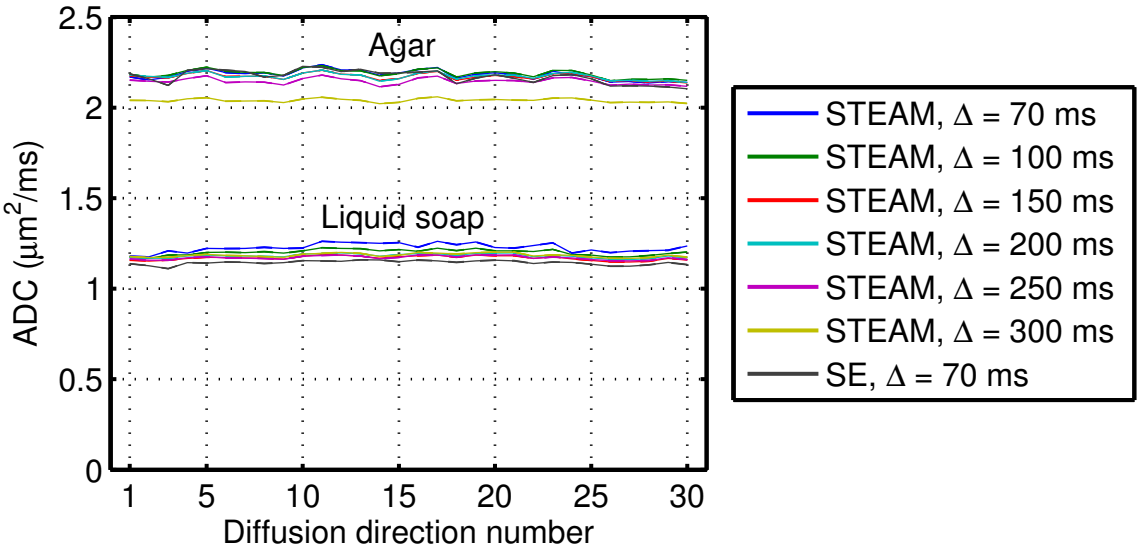


Figure 5.4: The ADC of the agar and liquid soap phantoms versus the diffusion direction number. The standard error of the mean of each curve is too small to appear in the plot. SE denotes the spin echo sequence.

in the STEAM sequence with flip angles that are more corrupted by off-resonance effects than the 180° pulse in the spin echo sequence.

5.3.1.3 Healthy Volunteers

The ADCs along the PDD of a representative in vivo scan are plotted as a function of the angle between diffusion direction and fibre orientation for FA thresholds of 0.2, 0.5, and 0.8 in Fig. 5.6a. The choice of FA threshold influences the observed relationship between ADC values and diffusion times. In the brain, differences in FA can be due to crossing fibres (unlikely in the phantom) as well as differences in packing density. Thus, as the FA threshold increases, the likelihood of selecting voxels with only parallel fibres increases. This is in line with the ADCs perpendicular to the fibres decreasing (at $\cos^2\theta = 0$) and parallel to the fibres increasing (at $\cos^2\theta = 1$) with increasing FA threshold. The signal attenuation is plotted in Fig. 5.6b and again, as there is no rectification, indicating that the noise floor has not been reached. The SNR of one representative $b = 0$ scan ranged from 21 at the shortest Δ to 11 at the

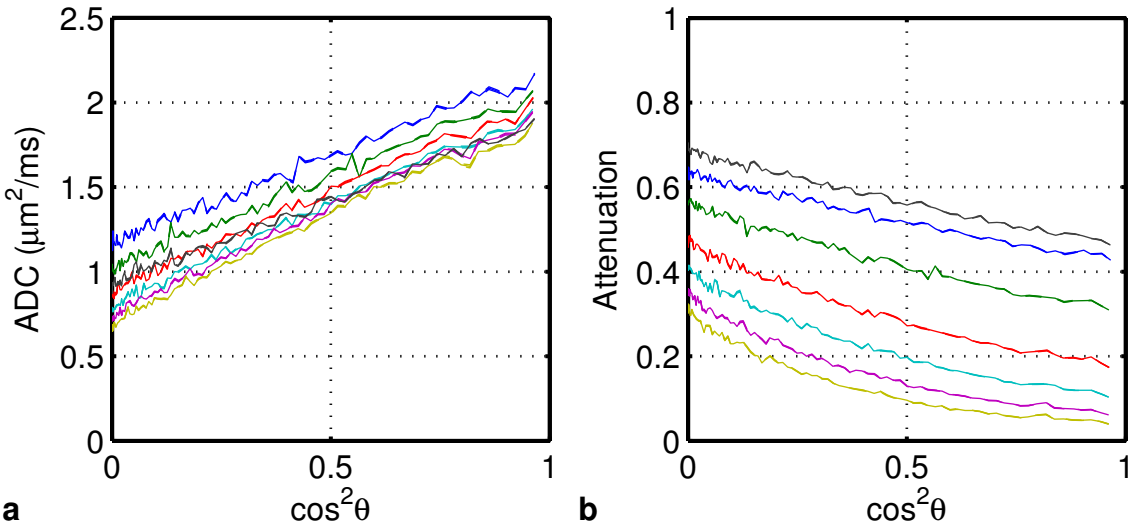


Figure 5.5: The (**a**) ADC and (**b**) signal attenuation along the PDD of the fibre phantom versus the square of the cosine of the angle with the diffusion direction. $\cos^2\theta = 0$ corresponds to diffusion perpendicular to the fibre and $\cos^2\theta = 1$ parallel. The standard error of the mean of each curve is too small to appear on the plots. The legend is as in Fig. 5.4.

longest.

Remarkably, in areas of high FA, it appears as though the diffusion time dependence of ADC is much higher along than across the fibres, which is consistent with literature (Burcaw et al., 2014). This is, as we will demonstrate below, an effect that cannot be accounted for by models of infinite cylinders, even when considering non-monoexponential diffusion.

5.3.2 Model Fitting

Figures 5.7 and 5.8 show the results and residuals, respectively, of fitting different variants of the Stanisz model to the STEAM in vivo scans (FA $>$ 0.8). Overall, the fitted curves match the measured values for all subjects and Δ reasonably well, with the exception of the two (infinite) cylinder models which do not match the data parallel to the fibres. This is expected, as infinite cylinders cannot exhibit hindered axial diffusivity.

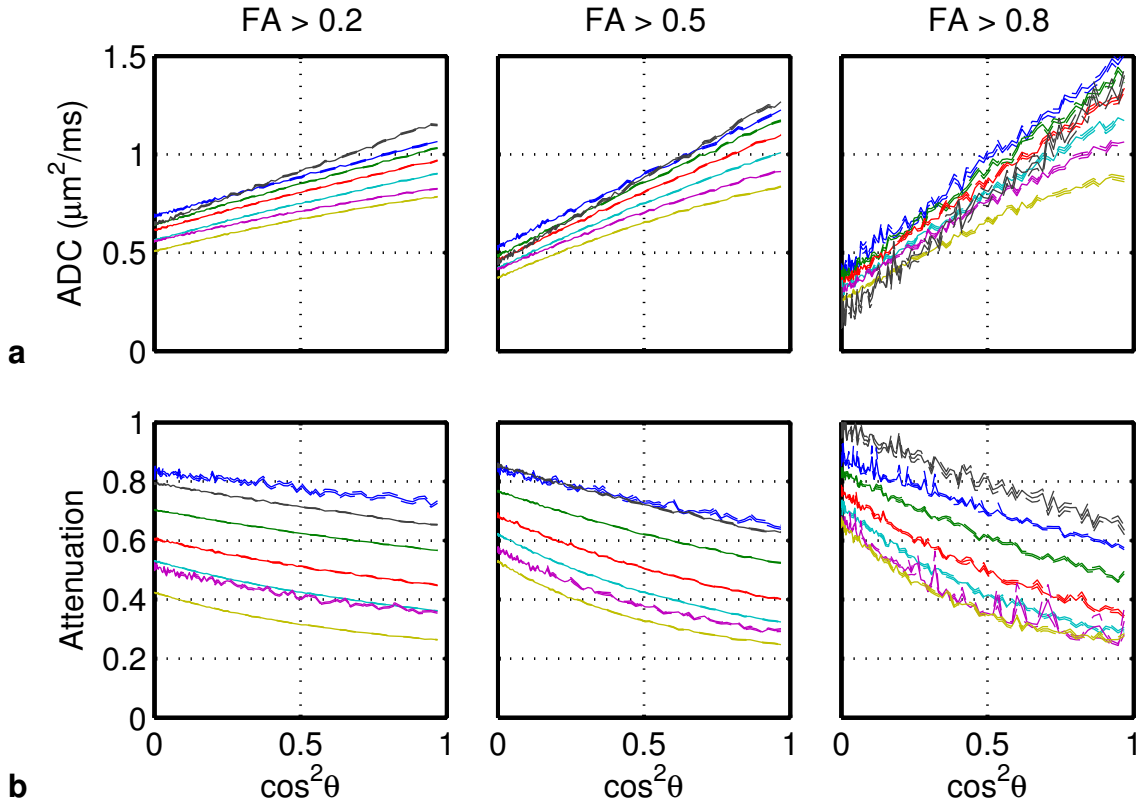


Figure 5.6: As Fig. 5.5, but of a representative in vivo scan versus the diffusion direction with FA $>$ 0.2, 0.5, and 0.8. The dashed lines indicate the standard error of the mean. Note that the vertical scale for the ADC plots is different from that in Fig. 5.5.

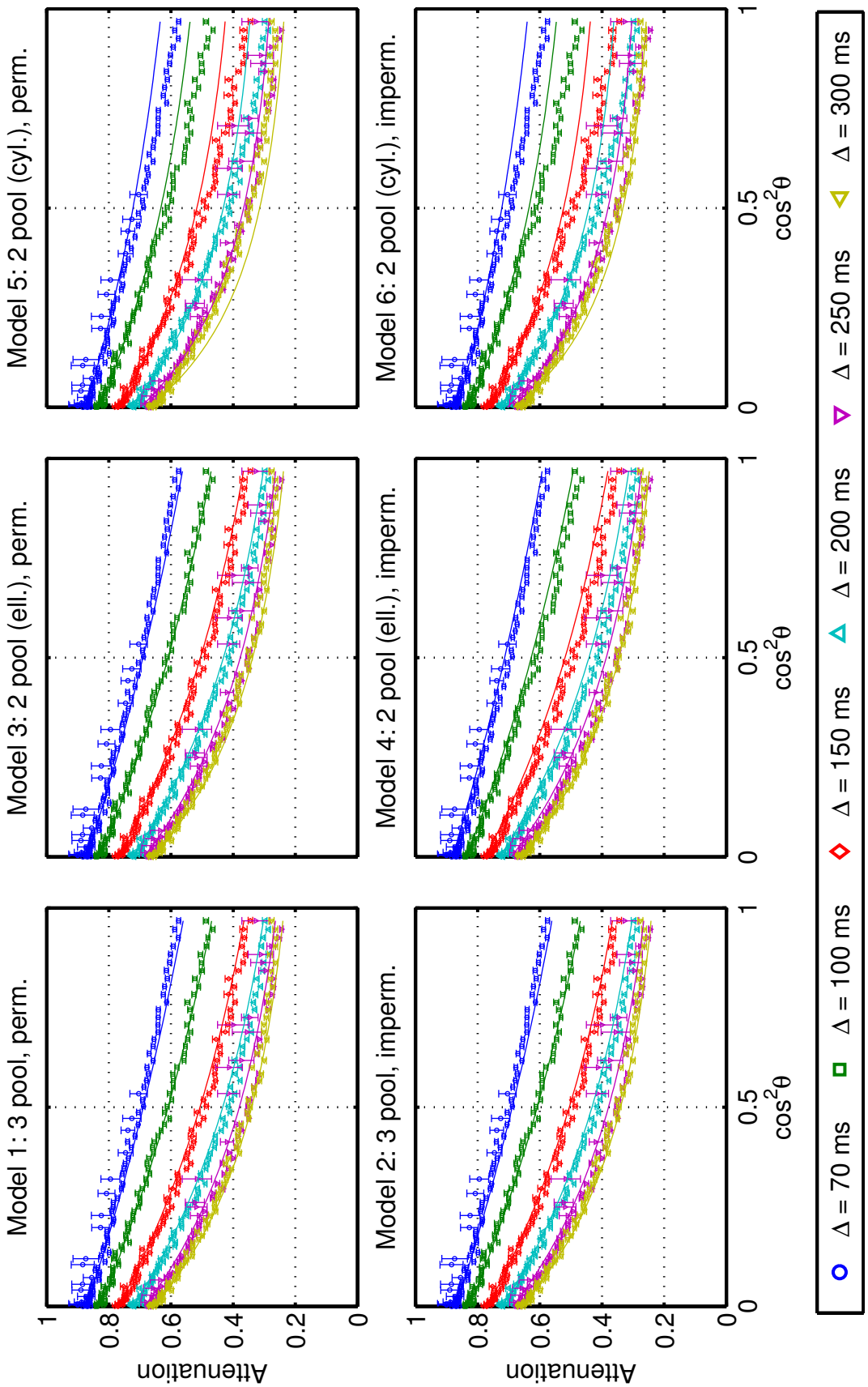


Figure 5.7: Measured (markers) and fitted (lines) STEAM diffusion attenuation versus angle with diffusion direction for a representative in vivo scan with FA > 0.8 fitted to the models in Table 5.5.

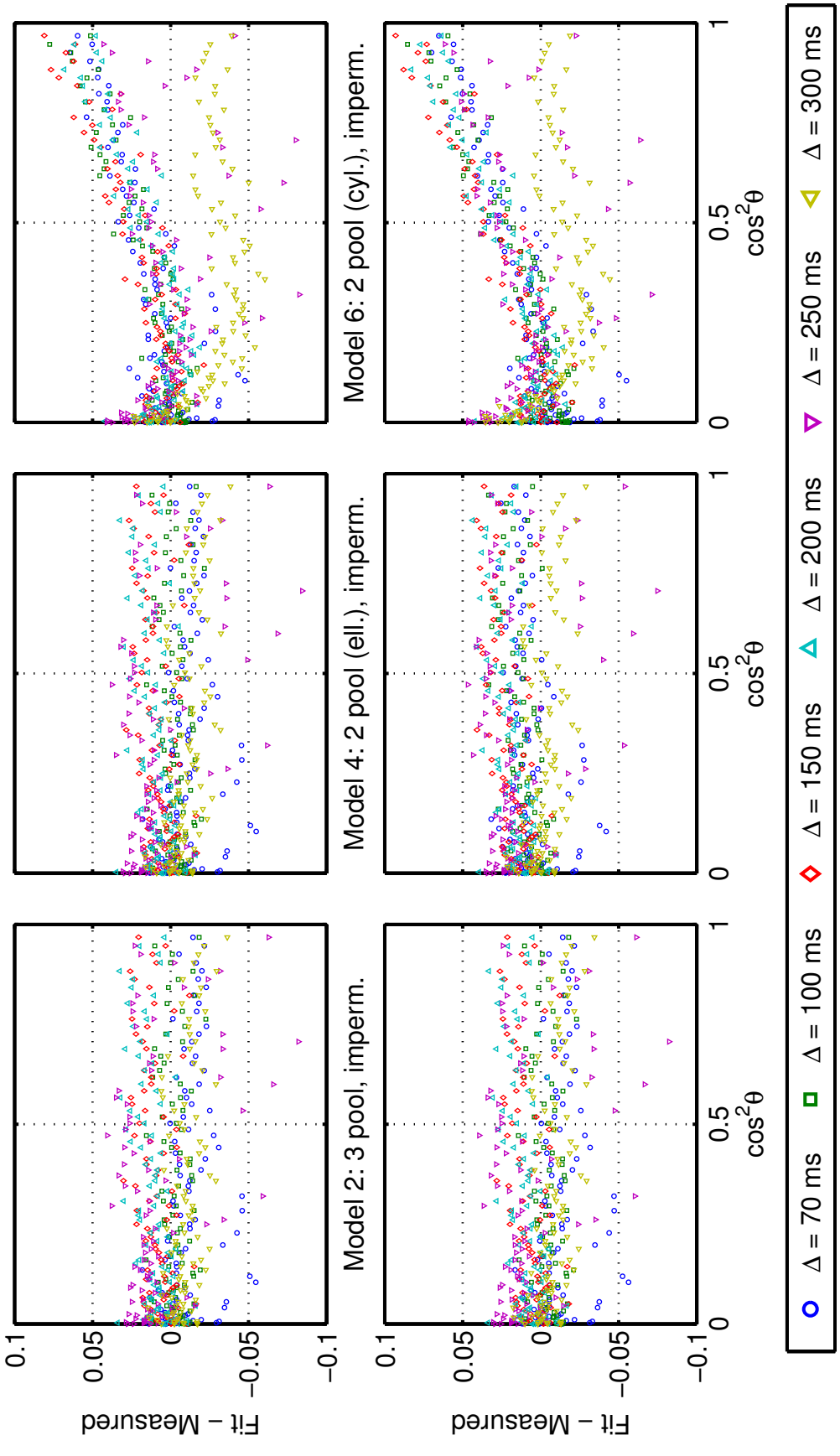


Figure 5.8: Residuals between measured and fitted STEAM diffusion attenuation versus angle with diffusion direction for a representative in vivo scan with FA > 0.8 of the models in Table 5.5.

The BIC of each model is shown in Fig. 5.9 and both three-pool models and the two-pool model with permeable ellipsoids have lowest values, which should indicate more appropriate dimensionality. However, BIC calculations do not reflect stability in parameter estimates. These can be gleaned from the posterior distribution of parameter estimates from the Metropolis–Hastings algorithms. Figure 5.10 summarises observations that were made on the stability and values of the model parameters.

In general, these results show that permeability parameters either had unstable fits or had mean values that were lower than expected, suggesting that there is little evidence for permeability effects in the data given the model. In addition, it is also clear that $a_T(\perp)$, the "axon diameter", was lower than expected. This can potentially be improved using models that include distributions over axon diameters (Assaf et al., 2008), and also by increasing the q value. Indeed, our q value of 0.08 rad/µm is too low to enable sensitivity to small displacements ($1/q = 12$ µm). However, the longitudinal ellipsoid size parameter was stable and significantly improved the fit compared to the infinite cylinder model, despite the latter effectively enabling biexponential diffusion (through D_{int} and D_{ext}). We conclude that the two-pool model with impermeable ellipsoids, which has BIC values overlapping with those of the three rejected models (Fig. 5.9), has the most appropriate dimensionality amongst the tested models. Only this model will be used in the remainder of this work.

The fitted values for the model parameters are shown in Table 5.6. They broadly agree with the values obtained in ex vivo tissue (Stanisz et al., 1997). However, the $a_{\text{T}}(\perp)$ parameter covers a large range. It is quite sensitive to the signal from diffusion perpendicular to axons, where there is the least diffusion contrast, and could likely be improved with higher b values, if sufficient SNR were maintained.

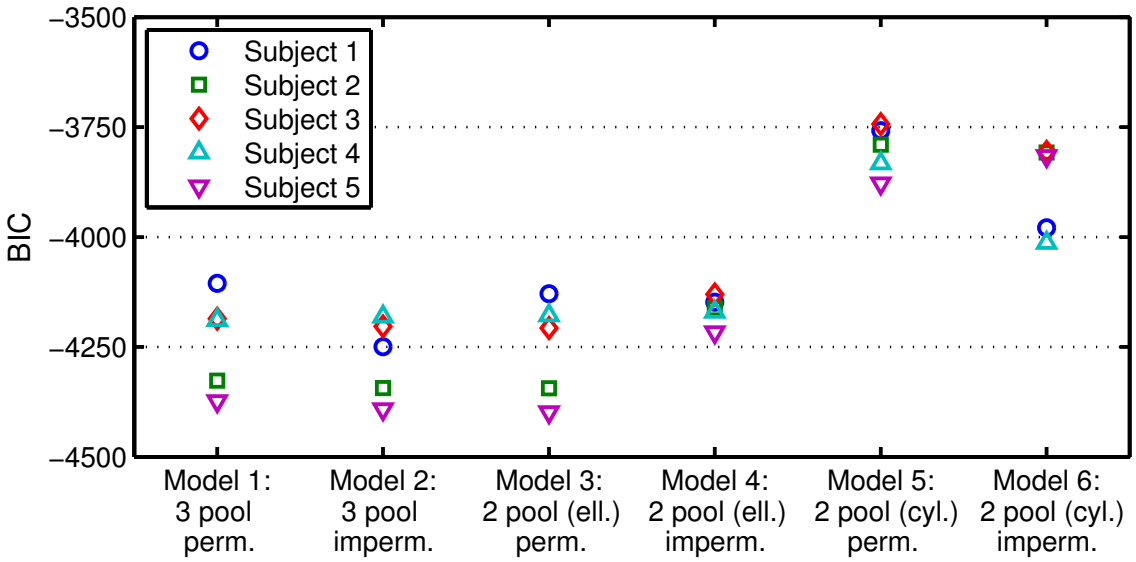


Figure 5.9: Bayesian information criteria (BIC) of the STEAM models in Table 5.5. Lower values indicate more appropriate model dimensionality. However, the three models on the left have fitting instabilities or implausible fitted values that preclude them from being used.

Subject	D_{int} (μm^2/ms)	$a_{\text{T}}(\perp)$ (μm)	$a_{\text{T}}(\parallel)$ (μm)	V_{T}	D_{ext} (μm^2/ms)
1	1.13 ± 0.11	0.52 ± 0.41	57.41 ± 3.39	0.53 ± 0.01	1.72 ± 0.06
2	1.35 ± 0.03	4.02 ± 1.25	45.87 ± 0.60	0.63 ± 0.01	2.29 ± 0.08
3	1.55 ± 0.06	5.43 ± 1.14	40.27 ± 0.39	0.59 ± 0.00	2.05 ± 0.03
4	1.33 ± 0.04	0.72 ± 0.55	46.43 ± 0.94	0.55 ± 0.01	1.83 ± 0.05
5	1.53 ± 0.03	1.18 ± 0.66	42.19 ± 0.40	0.56 ± 0.00	1.84 ± 0.02

Table 5.6: Fitted parameters of the two-pool model with impermeable ellipsoids.

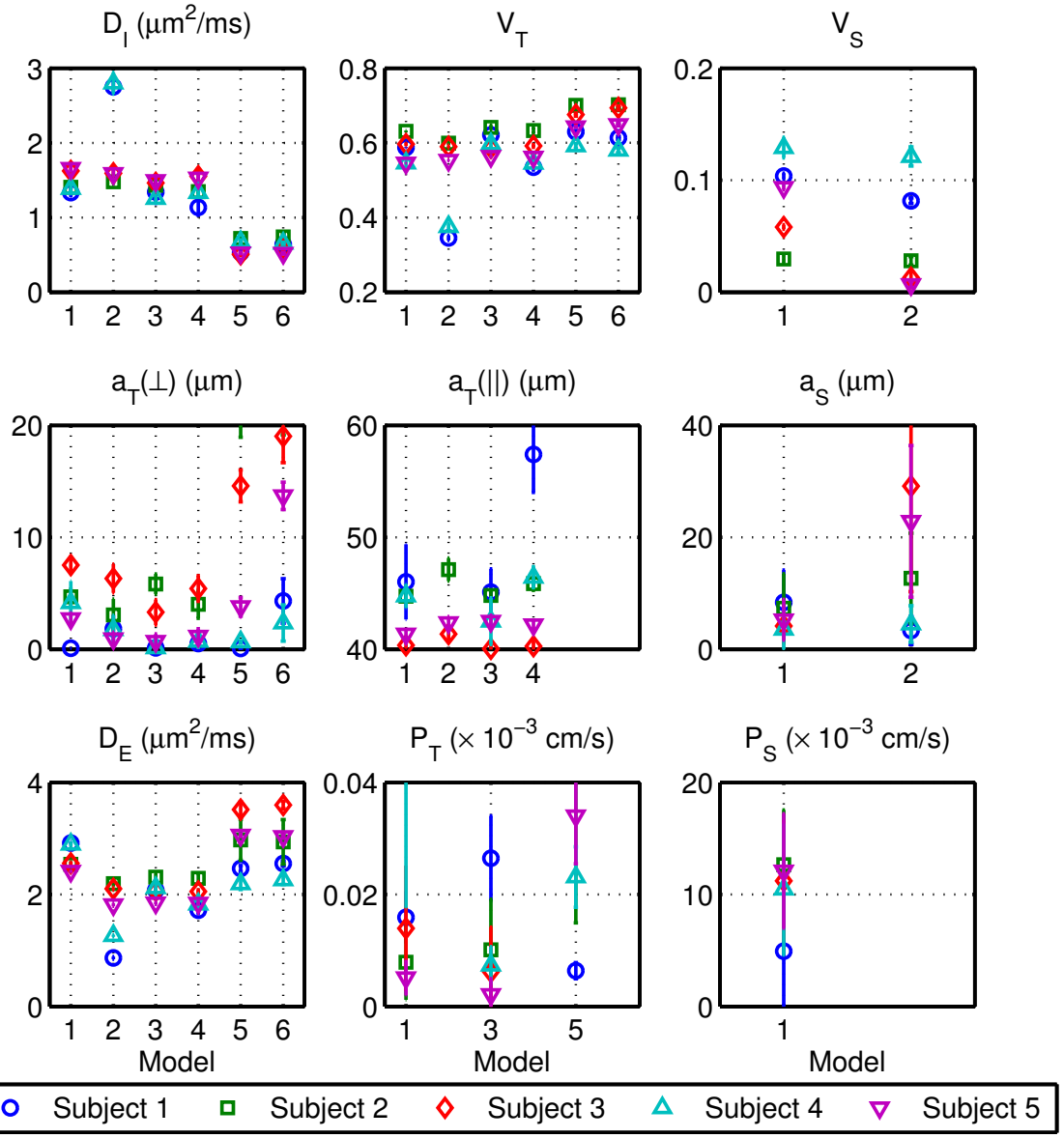


Figure 5.10: Comparison of the fitted parameters (mean and SD of the posterior distributions) of the models in Table 5.5. Models 1-3, 5, and 6 will not be further considered due to the following reasons: The P_S values and a_S values (Model 2) have large SD, which could indicate fitting instabilities. A previous study found P_T values that are an order of magnitude higher in fixed specimens (Stanisz et al., 1997) than those presented here and observed that b values higher than used in this paper are required for sensitivity to permeability. The $a_T(\perp)$ values (Models 5 and 6) cover a range that is larger than observed physiologically; these models also have inferior BICs (see Fig. 5.9). Only Model 4 will be considered in the remainder of this chapter.

5.4 Discussion

In this chapter, we used a nested set of models arising from a single, relatively complex analytic model to fit diffusion data from in vivo white matter acquired using multiple diffusion times ranging from 70 to 300 ms. Our experiments significantly differ from those to which the model was originally applied (Stanisz et al., 1997), which were on ex vivo tissue and used diffusion times in the range 8–30 ms. The observation that ADC is modulated by diffusion time parallel to the axons suggests that an infinite cylinder model is an inadequate description of the data. A model that uses prolate restricting ellipsoids can account for the observed diffusion time effect and the data do not appear to strongly support exchange effects. Below, we discuss these results in more detail.

5.4.1 Fitted Parameter Comparison with Literature

The fitted model parameters are generally in good agreement with those found in literature. The mean D_{int} and D_{ext} closely match the axial diffusivity measured in the in vivo human corpus callosum (Stikov et al., 2011) and, similar to post-mortem specimen data, $D_{\text{int}} < D_{\text{ext}}$ (Stanisz et al., 1997). The $a_{\text{T}}(\perp)$ values are of the correct order of magnitude (Aboitiz et al., 1992) but are also quite variable, possibly due to low diffusion contrast perpendicular to the axons and the low value for q afforded by our clinical scanner. Another possibility is that a distribution of axon diameters may be a more appropriate model.

The mean $a_{\text{T}}(||)$ is approximately twice that of bovine specimens (Stanisz et al., 1997). The lower specimen values could be due to effects such as axon beading from the physical stresses of handling or ischaemia (Budde and Frank, 2010). Alternately, the length scale of longitudinal restriction could be due to an inherent difference between fixed bovine and in vivo human tissues. The mean V_{T} of bovine specimens

reported in literature is 0.75 times that which we estimated in healthy volunteers. Axon shrinkage, which has been reported to shrink tissue to 0.65 of the original size (Aboitiz et al., 1992), could be responsible for this difference assuming that the EAS does not shrink during fixation.

5.4.2 Diffusion Parallel to Axons

Although axons are often modelled as infinite, parallel cylinders (Assaf et al., 2008; Fieremans et al., 2010; Alexander et al., 2010; Baxter and Frank, 2013), models with axons as infinitely long cylinders performed more poorly than those modelling axons as ellipsoids. This makes intuitive sense, as an infinite cylinder model assumes that axons remain aligned with the gradient orientation over distances much larger than $\sqrt{2D\Delta}$ (≈ 25 μm for $\Delta = 300$ ms).

Our data suggest that axons cannot be modelled as infinite cylinders when diffusion is measured over time scales exceeding 100 ms. However, the model that we used assumes longitudinal, intra-axonal diffusion to be restricted. An alternative could be to model it as hindered diffusion. For instance, a model with infinite cylinders that exhibit fanning would also display diffusion-time dependence along the longitudinal (average) direction. Such a model provides an interesting alternative to models that attempt to estimate fanning from single shell data by accurately modelling diffusion along a large number of directions (Sotiropoulos et al., 2012; Reisert et al., 2012). Instead, using long diffusion time measurements (with STEAM), it would be sufficient to measure diffusion along axons.

Our experimental data do not allow us to distinguish between pure restriction along axons and hindrance due to fanning. However, we can use simulations to establish how much fanning would be required in order to observe diffusion-time behaviours of the sort seen in our data. Figure 5.11 shows the calculated ADC using the two-pool model with impermeable infinite cylinders under four different amounts

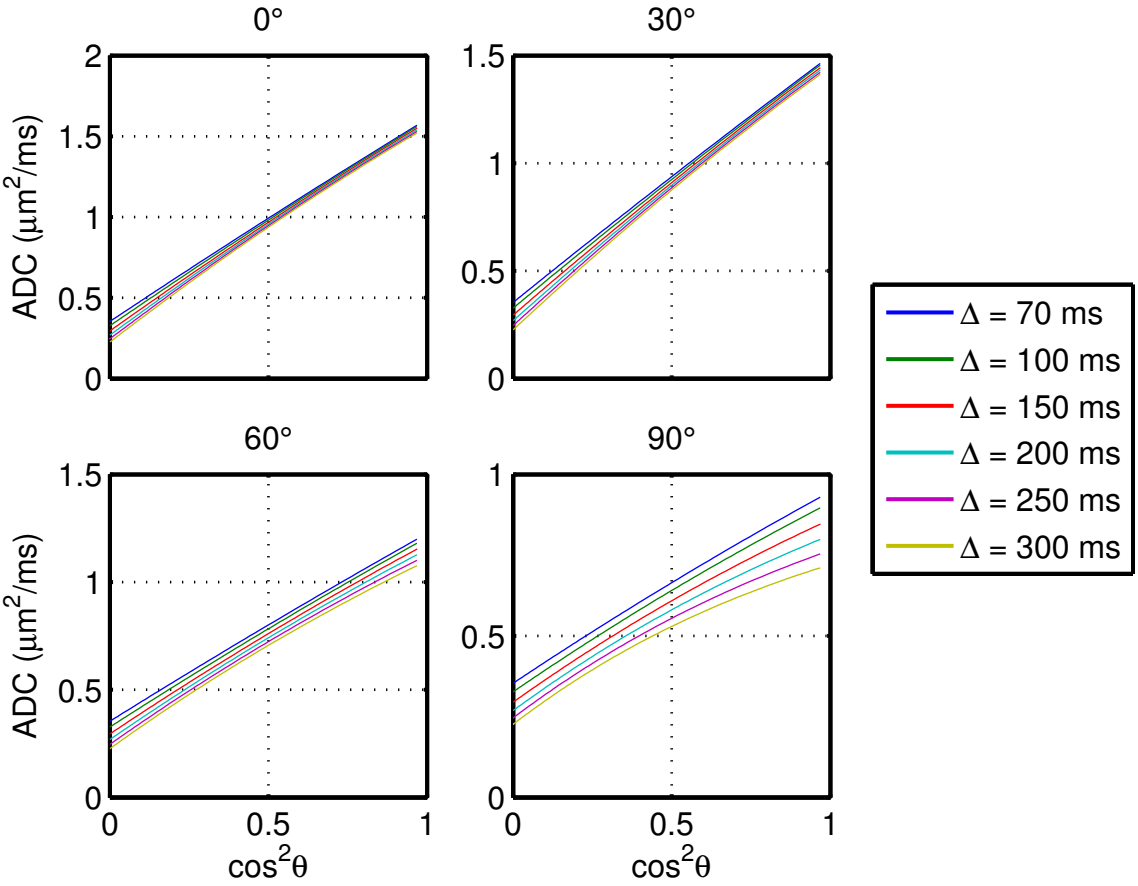


Figure 5.11: Forward model of the ADC along the PDD versus the square of the cosine of the angle with the diffusion direction for fibres with fanning angles of 0°, 30°, 60°, and 90°. $\cos^2\theta = 0$ corresponds to diffusion perpendicular to the fibre and $\cos^2\theta = 1$ parallel.

of fanning (i.e., the cylinders are not constrained to be parallel). Only the case with 90° of fanning is sufficient to produce greater Δ dependence parallel to the axons than perpendicular, as seen in our data. This amount of fanning may appear to be excessive, but it is consistent with findings from electron microscopy that axons in the mouse corpus callosum can fan with 80° (Fig. 2c in Mikula et al. (2012)). It is not known whether this is also true in humans, nor whether fanning occurs at a microscopic or voxel-wise scale.

There exist other possibilities for the physical basis of axial hindrance. First is the possibility of the narrowing of axons by 30–50% at nodes of Ranvier (Hildebrand

et al., 1993). The internodal length of the rat corpus callosum can be significantly larger than the mean $a_T(||)$, and was observed to be 80 ± 3.6 μm in one study (Bakiri et al., 2011) and ≈ 20–200 μm in another (Chong et al., 2012). However, since there is a linear relationship between axon diameter and internodal length (Murray and Blakemore, 1980) and the proportion of smaller axons is higher in humans than in macaques and even more so in mice (Aboitiz et al., 1992), the mean internodal length in humans could be less than that in rats and be comparable to the mean $a_T(||)$. Second, narrowing of axons in optic nerve specimens by a factor of 2 ± 0.6, not necessarily at nodes of Ranvier, has been reported and surmised to exist in vivo (Perge et al., 2009). This could cause axial hindrance to diffusion. However, the interval between these constrictions was not reported and thus cannot be compared to the mean $a_T(||)$. Third, hindrance could be caused by the processes of fibrous astrocytes, which occupy a significant volume fraction in white matter (Fig. 2.1), but these processes are known to be quite permeable Stanisz et al. (1997) as they are not myelinated. The span of fibrous astrocyte processes, which run parallel to axons, has been measured to be 183.2 ± 6.1 μm in humans (Oberheim et al., 2009, 2012), which is four times larger than the mean $a_T(||)$. Thus, the terminations of astrocyte processes likely does not account for the value of $a_T(||)$.

5.4.3 Model Assumptions

The current model assumes equal T_1 and T_2 relaxation times as well as proton density for all compartments. Stanisz et al. (1997) commented that the latter two assumptions were likely responsible for the higher than expected extracellular volume fraction that they observed. In our experiments, we also observed elevated extracellular fraction, but T_1 differences between compartments may also have played a role. The intra- and extracellular T_1 relaxation times have been estimated in the in vivo rat brain to be 235 ± 10 and 48 ± 8 ms, respectively, which are of comparable magnitude to

the Δ values in our experiment (Silva et al., 2002). To test this, the model could be extended to fit for compartment-specific T_1 values, but fitting T_1 accurately would require altering mixing time and diffusion time independently, which was not the case in our experiment.

5.5 Conclusions

We have applied an analytic model that estimates physical properties of white matter to diffusion-weighted MR data from healthy volunteers. The model fitted the acquired data well and the estimated parameters largely match those reported in literature for tissue specimens. This model can potentially be used to estimate the diffusivities, dimensions, and volume fraction of idealized axons of in vivo, single fibre white matter using a clinical scanner.

Chapter 6

Summary and Future Work

This thesis has focused on estimating microstructural information of white matter using diffusion-weighted MR imaging.

In Chapter 3, the need for accurate modelling of the diffusion spectrum around axons to properly interpret OGSE signal was recognized. A model was developed for the EAS diffusion spectrum of particles around parallel, impermeable cylinders with different packing geometries using spectra generated by Monte Carlo methods as the ground truth.

In Chapter 4, successful validation of the EAS diffusion spectrum model using OGSE data from an EAS phantom was shown. As well, the model was extended to include the contributions to the diffusion spectrum from the IAS. This model, after simplification to make it more robust, was applied to OGSE data from corpus callosum specimens, which is a simple model system.

In Chapter 5, long diffusion time scans were employed to access information that is not available to the relatively short diffusion times of OGSE. The ADC parallel to the axons in the corpus callosum was found to have hindered diffusion instead of free diffusion. A series of nested models was applied to this data, one of which was able to robustly quantify the length scale of this hindrance as well as estimate other

parameters such as IAS and EAS diffusivity and volume fraction.

6.1 Future Work

Each of Chapters 3–5 raised interesting results while also raising additional questions. Here we discuss some of these questions and ways they can potentially be answered.

6.1.1 EAS Diffusion Spectrum Model Improvement

An important comment was raised when the EAS diffusion spectrum model in Chapter 3 was presented at the 22$^{\text{nd}}$ Annual Meeting of ISMRM in Milan, Italy in 2014. The commenter pointed out that the case which is the most applicable to white matter – tightly packed randomly placed cylinders with a distribution of radii (Fig. 3.13, left plot, blue circles) – has a discrepancy between the model prediction and simulation around 1 kHz and that this is not the case with either square or hexagonally packed cylinders. He cited earlier work (Burcaw et al., 2013), which stated that $D_{\text{ext}}(\omega)$ at low ω should be functions of ω^2 and $|\omega|$ for regular and random packing, respectively, and that this was not accounted for in the EAS model, which has an ω^2 dependency for both packing types – see also Burcaw et al. (2015). Fits of both functions of ω to simulated $D_{\text{ext}}(\omega)$ support this (Fig. 6.1). Indeed, the random packing case is the most interesting and, as a consequence, deserves to have its model improved. Perhaps the cited findings can be used to modify the model to have it match the simulated diffusion spectra more accurately.

6.1.2 EAS Diffusion Spectrum Model Validation

The models fits to the diffusion spectra of the corpus callosum specimens in Chapter 4 return values that are comparable to those in literature (Table 4.4). However, these compelling values need to be validated by rigorous means such as histology as is

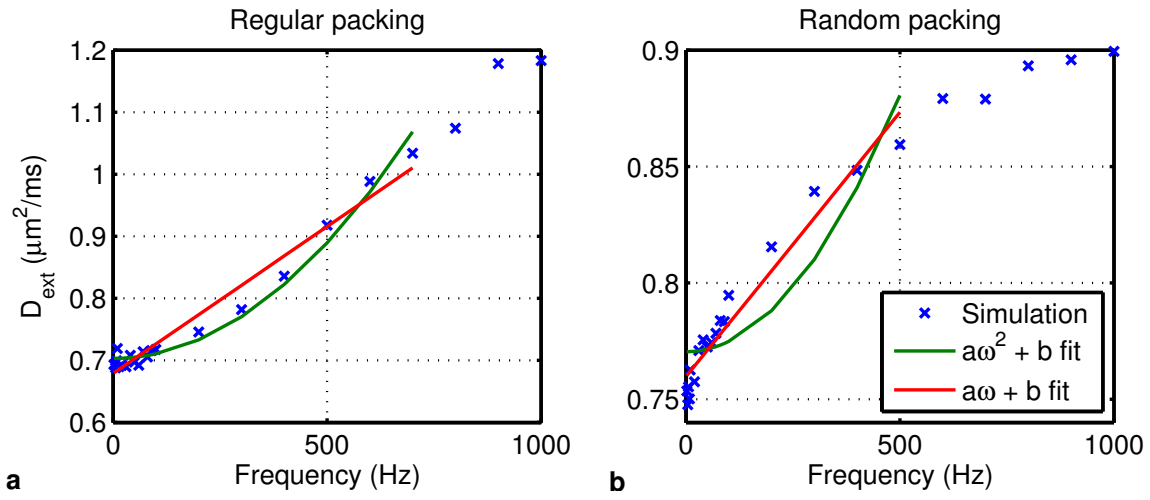


Figure 6.1: Representative simulated $D_{\text{ext}}(\omega)$ (markers) from Chapter 3 for (**a**) regular and (**b**) random packing at low ω with fits showing ω^2 dependence for the former and ω for the latter. This is in agreement with Burcaw et al. (2013).

commonly done (Assaf et al., 2008; Barazany et al., 2009). The samples have been carefully placed in storage and are available to be scanned by electron microscope.

6.1.3 EAS Diffusion Spectra of Tissue

In Chapter 4, fibre phantom and tissue specimens scans were described. However, they span a large range of geometric complexity; the phantom has relatively simple EAS and the specimens quite complex IAS and EAS signal contributions. An intermediate level of complexity with only the EAS of tissue would be a useful step for further testing of the EAS diffusion spectrum model. There is potentially an indirect way of accessing only the EAS diffusion spectrum of tissue. The diffusion spectrum of the IAS could be subtracted from the combined IAS and EAS as acquired in Chapter 4. The IAS-only diffusion spectrum could potentially be acquired by performing diffusion encoding on metabolites which are known only to be in the IAS (Marchadour et al., 2012). This would not be trivial as metabolites will likely have a different free diffusivity than that of water.

Another possible experiment would address the issue raised in Chapter 4 about

exchange between the IAS and EAS. If indeed there is exchange, then the diffusion spectrum model will need to be modified. To probe such effects, perhaps additional PGSE scans at various q and Δ values could be included to inform a model such as that presented in Chapter 5 (or a subset of it, of course) combined with the diffusion spectrum model.

6.1.4 The Origins of Axial Hindered Diffusion

The hindered diffusion seen along the direction of axons in Chapter 5 led to many questions as to the cause of this hindrance. Higher resolution MR scans on specimens in an animal scanner which use a hundred diffusion directions could fit an axon dispersion model to verify whether this effect due to bending that occurs on the scale of hundreds of micrometers, which is the typical resolution of such scanners (Dyrby et al., 2012). Electron (Mikula et al., 2012) and polarized light (Axer et al., 2011) microscopy could also shed light on whether large axon fanning occurs within a small space within bundles of "parallel" fibres. The details gained from such experiments could serve to improve the models applied to conventional STEAM or spin echo diffusion-weighted scans.

References

Aboitiz, F., Scheibel, A. B., Fisher, R. S., and Zaidel, E. (1992). Fiber composition of the human corpus callosum. *Brain Res*, 598(1-2):143–153.

Aggarwal, M., Jones, M. V., Calabresi, P. A., Mori, S., and Zhang, J. (2012). Probing mouse brain microstructure using oscillating gradient diffusion MRI. *Magn Reson Med*, 67(1):98–109.

Alexander, D. C. (2005). Multiple-fiber reconstruction algorithms for diffusion MRI. *Ann N Y Acad Sci*, 1064:113–133.

Alexander, D. C., Hubbard, P. L., Hall, M. G., Moore, E. A., Ptito, M., Parker, G. J. M., and Dyrby, T. B. (2010). Orientationally invariant indices of axon diameter and density from diffusion MRI. *NeuroImage*, 52(4):1374–1389.

Andersson, J. and Sotiropoulos, S. N. (2014). A Gaussian Process based method for detecting and correcting dropout in diffusion imaging. In *Proceedings of the 22nd Annual Meeting of ISMRM*, page 2567, Milan, Italy.

Andersson, J. L. R., Skare, S., and Ashburner, J. (2003). How to correct susceptibility distortions in spin-echo echo-planar images: Application to diffusion tensor imaging. *Neuroimage*, 20(2):870–888.

Andersson, J. L. R., Xu, J., Yacoub, E., Auerbach, E., Moeller, S., and Ugurbil, K. (2012). A comprehensive Gaussian Process framework for correcting distortions and movements in diffusion images. In *Proceedings of the 20th Annual Meeting of ISMRM*, page 2426, Melbourne, Australia.

Andrews, T. J., Osborne, M. T., and Does, M. D. (2006). Diffusion of myelin water. *Magn Reson Med*, 56(2):381–385.

Assaf, Y., Blumenfeld-Katzir, T., Yovel, Y., and Basser, P. J. (2008). AxCaliber: A method for measuring axon diameter distribution from diffusion MRI. *Magn Reson Med*, 59(6):1347–1354.

Assaf, Y. and Cohen, Y. (1998). Non-mono-exponential attenuation of water and N-acetyl aspartate signals due to diffusion in brain tissue. *J Magn Reson*, 131(1):69–85.

Assaf, Y., Freidlin, R. Z., Rohde, G. K., and Basser, P. J. (2004). New modeling and experimental framework to characterize hindered and restricted water diffusion in brain white matter. *Magn Reson Med*, 52(5):965–978.

Assaf, Y., Kafri, M., Shinar, H., Chapman, J., Korczyn, A. D., Navon, G., and Cohen, Y. (2002). Changes in axonal morphology in experimental autoimmune neuritis as studied by high b-value q-space (1)H and (2)H DQF diffusion magnetic resonance spectroscopy. *Magn Reson Med*, 48(1):71–81.

Avram, A. V., Özarslan, E., Sarlls, J. E., and Basser, P. J. (2013). In vivo detection of microscopic anisotropy using quadruple pulsed-field gradient (qPFG) diffusion MRI on a clinical scanner. *NeuroImage*, 64:229–239.

Axer, H., Beck, S., Axer, M., Schuchardt, F., Heepe, J., Flücken, A., Axer, M., Prescher, A., and Witte, O. W. (2011). Microstructural analysis of human white matter architecture using polarized light imaging: Views from neuroanatomy. *Front Neuroinform*, 5:28.

Bakiri, Y., Káradóttir, R., Cossell, L., and Attwell, D. (2011). Morphological and electrical properties of oligodendrocytes in the white matter of the corpus callosum and cerebellum. *J Physiol*, 589(Pt 3):559–573.

Barazany, D., Basser, P. J., and Assaf, Y. (2009). In vivo measurement of axon diameter distribution in the corpus callosum of rat brain. *Brain*, 132:1210–1220.

Barnett, M. W. and Larkman, P. M. (2007). The action potential. *Pract Neurol*, 7(3):192–197.

Baron, C. A. and Beaulieu, C. (2014). Oscillating gradient spin-echo (OGSE) diffusion tensor imaging of the human brain. *Magn Reson Med*, 72(3):726–736.

Barres, B. A. (2008). The mystery and magic of glia: A perspective on their roles in health and disease. *Neuron*, 60(3):430–440.

Basser, P. J., Mattiello, J., and LeBihan, D. (1994a). Estimation of the effective self-diffusion tensor from the NMR spin echo. *J Magn Reson B*, 103(3):247–254.

Basser, P. J., Mattiello, J., and LeBihan, D. (1994b). MR diffusion tensor spectroscopy and imaging. *Biophys J*, 66(1):259–267.

Baumann, N. and Pham-Dinh, D. (2001). Biology of oligodendrocyte and myelin in the mammalian central nervous system. *Physiol Rev*, 81(2):871–927.

Baxter, G. T. and Frank, L. R. (2013). A computational model for diffusion weighted imaging of myelinated white matter. *NeuroImage*, 75C:212–220.

Beaulieu, C. and Allen, P. S. (1994). Determinants of anisotropic water diffusion in nerves. *Magn Reson Med*, 31(4):394–400.

Behrens, T. E. J., Johansen-Berg, H., Jbabdi, S., Rushworth, M. F. S., and Woolrich, M. W. (2007). Probabilistic diffusion tractography with multiple fibre orientations: What can we gain? *NeuroImage*, 34(1):144–155.

Bernstein, M. A., King, K. F., and Zhou, X. J. (2004a). *Handbook of MRI Pulse Sequences*, page 960. Elsevier Academic Press, San Diego.

Bernstein, M. A., King, K. F., and Zhou, X. J. (2004b). *Handbook of MRI Pulse Sequences*, chapter 11. Elsevier Academic Press, San Diego.

Bonkowsky, J. L., Nelson, C., Kingston, J. L., Filloux, F. M., Mundorff, M. B., and Srivastava, R. (2010). The burden of inherited leukodystrophies in children. *Neurology*, 75(8):718–725.

Budde, M. D. and Frank, J. A. (2010). Neurite beading is sufficient to decrease the apparent diffusion coefficient after ischemic stroke. *Proc Natl Acad Sci USA*, 107(32):14472–14477.

Burcaw, L., Fieremans, E., and Novikov, D. S. (2013). Singular behavior of time-dependent diffusion in a fiber bundle geometry due to a disordered packing. In *Proceedings of the 21st Annual Meeting of ISMRM*, page 495, Salt Lake City, Utah, USA.

Burcaw, L., Veraart, J., Novikov, D. S., and Fieremans, E. (2014). In vivo observation of time-dependent diffusion in white matter in humans. In *Proceedings of the 22nd Annual Meeting of ISMRM*, page 4434, Milan, Italy.

Burcaw, L. M., Fieremans, E., and Novikov, D. S. (2015). Mesoscopic structure of neuronal tracts from time-dependent diffusion. *NeuroImage*, 114(0):18 – 37.

Callaghan, P. T. (1991). *Principles of Nuclear Magnetic Resonance Microscopy*, page 331. Oxford University Press, Oxford.

Callaghan, P. T., Coy, A., MacGowan, D., Packer, K. J., and Zelaya, F. O. (1991). Diffraction-like effects in NMR diffusion studies of fluids in porous solids. *Nature*, 351:467–469.

Callaghan, P. T., Eccles, C. D., and Xia, Y. (1988). NMR microscopy of dynamic displacements: k-Space and q-space imaging. *J Phys E*, 21(8):820–822.

Chapman, M. C., Jelsone-Swain, L., Johnson, T. D., Gruis, K. L., and Welsh, R. C. (2013). Diffusion tensor MRI of the corpus callosum in amyotrophic lateral sclerosis. *J Magn Reson Imaging*, 39:641–647.

Chen, K. C. and Nicholson, C. (2000). Changes in brain cell shape create residual extracellular space volume and explain tortuosity behavior during osmotic challenge. *Proc Natl Acad Sci USA*, 97(15):8306–8311.

Chen, S.-T. and Springer, C. S. (1981). Ionophore-catalyzed cation transport between phospholipid inverted micelles manifest in dNMR. *Biophys Chem*, 14(4):375–388.

Chong, S. Y. C., Rosenberg, S. S., Fancy, S. P. J., Zhao, C., Shen, Y.-A. A., Hahn, A. T., McGee, A. W., Xu, X., Zheng, B., Zhang, L. I., Rowitch, D. H., Franklin, R. J. M., Lu, Q. R., and Chan, J. R. (2012). Neurite outgrowth inhibitor Nogo-A establishes spatial segregation and extent of oligodendrocyte myelination. *Proc Natl Acad Sci USA*, 109(4):1299–1304.

Clark, C. A. and Le Bihan, D. (2000). Water diffusion compartmentation and anisotropy at high b values in the human brain. *Magn Reson Med*, 44(6):852–859.

Coleman, M. P. and Freeman, M. R. (2010). Wallerian degeneration, Wld(S), and Nmnat. *Annu Rev Neurosci*, 33:245–267.

Colvin, D. C., Loveless, M. E., Does, M. D., Yue, Z., Yankeelov, T. E., and Gore, J. C. (2011). Earlier detection of tumor treatment response using magnetic resonance diffusion imaging with oscillating gradients. *Magn Reson Imaging*, 29(3):315–323.

Compston, A. and Coles, A. (2008). Multiple sclerosis. *Lancet*, 372(9648):1502–1517.

Cook, P. A., Bai, Y., Nedjati-Gilani, S., Seunarine, K. K., Hall, M. G., Parker, G. J. M., and Alexander, D. C. (2006). Camino: Open-source diffusion-MRI reconstruction and processing. In *Proceedings of the 14th Annual Meeting of ISMRM*, page 2759, Berlin, Germany.

Cory, D. G. and Garroway, A. N. (1990). Measurement of translational displacement probabilities by NMR: An indicator of compartmentation. *Magn Reson Med*, 14(3):435–444.

Cox, E. F. and Gowland, P. A. (2010). Simultaneous quantification of T2 and T2' using a combined gradient echo-spin echo sequence at ultrahigh field. *Magn Reson Med*, 64(5):1440–1445.

D'Arceuil, H. E., Westmoreland, S., and de Crespigny, A. J. (2007). An approach to high resolution diffusion tensor imaging in fixed primate brain. *NeuroImage*, 35(2):553–565.

De Santis, S., Drakesmith, M., Bells, S., Assaf, Y., and Jones, D. K. (2014). Why diffusion tensor MRI does well only some of the time: Variance and covariance of white matter tissue microstructure attributes in the living human brain. *NeuroImage*, 89:35–44.

de Swiet, T. M. and Sen, P. N. (1994). Decay of nuclear magnetization by bounded diffusion in a constant field gradient. *J Chem Phys*, 100(8):5597–5604.

Delannoy, J., Chen, C.-N., Turner, R., Levin, R. L., and Le Bihan, D. (1991). Noninvasive temperature imaging using diffusion MRI. *Magn Reson Med*, 19(2):333–339.

Dhital, B., Labadie, C., Möller, H. E., and Turner, R. (2011). Activation energies for water diffusion in ex-vivo white matter. In *Proceedings of the 19th Annual Meeting of ISMRM*, page 78, Montréal, Québec, Canada.

Does, M. D., Parsons, E. C., and Gore, J. C. (2003). Oscillating gradient measurements of water diffusion in normal and globally ischemic rat brain. *Magn Reson Med*, 49(2):206–215.

Drobnjak, I. and Alexander, D. C. (2011). Optimising time-varying gradient orientation for microstructure sensitivity in diffusion-weighted MR. *J Magn Reson*, 212(2):344–354.

Drobnjak, I., Siow, B., and Alexander, D. C. (2010). Optimizing gradient waveforms for microstructure sensitivity in diffusion-weighted MR. *J Magn Reson*, 206(1):41–51.

Du, J., Ma, G., Li, S., Carl, M., Szeverenyi, N. M., Vandenberg, S., Corey-Bloom, J., and Bydder, G. M. (2013). Ultrashort echo time (UTE) magnetic resonance imaging of the short T2 components in white matter of the brain using a clinical 3T scanner. *NeuroImage*, 87C:32–41.

Dyrby, T. B., Søgaard, L. V., Hall, M. G., Ptito, M., and Alexander, D. C. (2012). Contrast and stability of the axon diameter index from microstructure imaging with diffusion MRI. *Magn Reson Med*, 70:711–721.

Einstein, A. (1905). Über die von der molekularkinetischen Theorie der wärme geforderte Bewegung von in ruhenden flüssigkeiten suspendierten Teilchen. *Ann Physik*, 322(8):549–560.

Fields, R. D. (2008). White matter in learning, cognition and psychiatric disorders. *Trends Neurosci*, 31(7):361–370.

Fieremans, E., Deene, Y. D., Delputte, S., Özdemir, M. S., Achten, E., and Lemahieu, I. (2008a). The design of anisotropic diffusion phantoms for the validation of diffusion weighted magnetic resonance imaging. *Phys Med Biol*, 53(19):5405–5419.

Fieremans, E., Deene, Y. D., Delputte, S., Özdemir, M. S., D'Asseler, Y., Vlassenbroeck, J., Deblaere, K., Achten, E., and Lemahieu, I. (2008b). Simulation and experimental verification of the diffusion in an anisotropic fiber phantom. *J Magn Reson*, 190(2):189–199.

Fieremans, E., Novikov, D. S., Jensen, J. H., and Helpern, J. A. (2010). Monte Carlo study of a two-compartment exchange model of diffusion. *NMR Biomed*, 23(7):711–724.

Fonteijn, H. M., Hall, M. G., and Alexander, D. C. (2009). A study on the validity of the tortuosity approximation for extracellular diffusion using monte carlo simulations. In *Proceedings of the 17th Annual Meeting of ISMRM*, page 1361, Honolulu, Hawai'i, USA.

Ford, J. C. and Hackney, D. B. (1997). Numerical model for calculation of apparent diffusion coefficients (ADC) in permeable cylinders–comparison with measured ADC in spinal cord white matter. *Magn Reson Med*, 37(3):387–394.

Fordham, E. J., Mitra, P. P., and Latour, L. L. (1996). Effective diffusion times in multiple-pulse PFG diffusion measurements in porous media. *J Magn Reson A*, 121:187–192.

Glasser, M. F. and Van Essen, D. C. (2011). Mapping human cortical areas in vivo based on myelin content as revealed by T1- and T2-weighted MRI. *J Neurosci*, 31(32):11597–616.

Gore, J. C., Xu, J., Colvin, D. C., Yankeelov, T. E., Parsons, E. C., and Does, M. D. (2010). Characterization of tissue structure at varying length scales using temporal diffusion spectroscopy. *NMR Biomed*, 23(7):745–756.

Hahn, E. L. (1950). Spin echoes. *Phys Rev*, 80(4):580–594.

Hall, M. G. and Alexander, D. C. (2009). Convergence and parameter choice for Monte-Carlo simulations of diffusion MRI. *IEEE Trans Med Imaging*, 28(9):1354–1364.

Hanisch, U.-K. (2013). Functional diversity of microglia - how heterogeneous are they to begin with? *Front Cell Neurosci*, 7:65.

Hanson, L. G. (2008). Is quantum mechanics necessary for understanding magnetic resonance? *Concepts Magn Reson*, 32A(5):329–340.

Hildebrand, C., Remahl, S., Persson, H., and Bjartmar, C. (1993). Myelinated nerve fibres in the CNS. *Prog Neurobiol*, 40(3):319–384.

Horch, R. A., Gore, J. C., and Does, M. D. (2011). Origins of the ultrashort-T2 1H NMR signals in myelinated nerve: A direct measure of myelin content? *Magn Reson Med*, 66(1):24–31.

Hrabe, J., Hrabetová, S., and Segeth, K. (2004). A model of effective diffusion and tortuosity in the extracellular space of the brain. *Biophys J*, 87(3):1606–1617.

Hsu, K.-S., Liang, Y.-C., and Huang, C.-C. (2000). Influence of an extracellular acidosis on excitatory synaptic transmission and long-term potentiation in the ca1 region of rat hippocampal slices. *J Neurosci Res*, 62(3):403–415.

Hwang, S. N., Chin, C.-L., Wehrli, F. W., and Hackney, D. B. (2003). An image-based finite difference model for simulating restricted diffusion. *Magn Reson Med*, 50(2):373–382.

Ianuş, A., Siow, B., Drobnjak, I., Zhang, H., and Alexander, D. C. (2013). Gaussian phase distribution approximations for oscillating gradient spin echo diffusion MRI. *J Magn Reson*, 227:25–34.

Jiang, P.-C., Yu, T.-Y., Perng, W.-C., and Hwang, L.-P. (2001). Pore-to-pore hopping model for the interpretation of the pulsed gradient spin echo attenuation of water diffusion in cell suspension systems. *Biophys J*, 80(6):2493–2504.

Jin, S., Zador, Z., and Verkman, A. S. (2008). Random-walk model of diffusion in three dimensions in brain extracellular space: Comparison with microfiberoptic photobleaching measurements. *Biophys J*, 95(4):1785–1794.

Johansen-Berg, H. (2010). Behavioural relevance of variation in white matter microstructure. *Curr Opin Neurol*, 23(4):351–358.

Jones, D. K. and Cercignani, M. (2010). Twenty-five pitfalls in the analysis of diffusion MRI data. *NMR Biomed*, 23(7):803–820.

Kärger, J. (1969). Zur Bestimmung der Diffusion in einem Zweibereichsystem mit Hilfe von gepulsten Feldgradienten. *Ann Physik*, 24(1/2):1–4.

Kiruluta, A. J. M. (2008). Probing restrictive diffusion dynamics at short time scales. *J Magn Reson*, 192(1):27–36.

Komlosh, M. E., Özarslan, E., Lizak, M. J., Horkayne-Szakaly, I., Freidlin, R. Z., Horkay, F., and Basser, P. J. (2013). Mapping average axon diameters in porcine spinal cord white matter and rat corpus callosum using d-PFG MRI. *NeuroImage*, 78:210–216.

Kornek, B., Storch, M. K., Bauer, J., Djamshidian, A., Weissert, R., Wallstroem, E., Stefferl, A., Zimprich, F., Olsson, T., Linington, C., Schmidbauer, M., and Lassmann, H. (2001). Distribution of a calcium channel subunit in dystrophic axons in multiple sclerosis and experimental autoimmune encephalomyelitis. *Brain*, 124(Pt 6):1114–1124.

Kumar, S., Yin, X., Trapp, B. D., Paulaitis, M. E., and Hoh, J. H. (2002). Role of long-range repulsive forces in organizing axonal neurofilament distributions: Evidence from mice deficient in myelin-associated glycoprotein. *J Neurosci Res*, 68(6):681–690.

Lam, W. W., Jbabdi, S., and Miller, K. L. (2015). A model for extra-axonal diffusion spectra with frequency-dependent restriction. *Magn Reson Med*, 73(6):2306–2320.

Landis, C. S., Li, X., Telang, F. W., Coderre, J. A., Micca, P. L., Rooney, W. D., Latour, L. L., Vétek, G., Pályka, I., and Springer, C. S. (2000). Determination of the MRI contrast agent concentration time course in vivo following bolus injection: Effect of equilibrium transcytolemmal water exchange. *Magn Reson Med*, 44(4):563–574.

Larson, P. E. Z., Kerr, A. B., Reed, G. D., Hurd, R. E., Kurhanewicz, J., Pauly, J. M., and Vigneron, D. B. (2012). Generating super stimulated-echoes in MRI and their application to hyperpolarized C-13 diffusion metabolic imaging. *IEEE Trans Med Imaging*, 31(2):265–275.

Lasič, S., Åslund, I., and Topgaard, D. (2009). Spectral characterization of diffusion with chemical shift resolution: Highly concentrated water-in-oil emulsion. *J Magn Reson*, 199(2):166–172.

Lasič, S., Nilsson, M., Lätt, J., Ståhlberg, F., and Topgaard, D. (2011). Apparent exchange rate mapping with diffusion MRI. *Magn Reson Med*, 66(2):356–365.

Latour, L. L., Mitra, P. P., Kleinberg, R. L., and Sotak, C. H. (1993). Time-dependent diffusion coefficient of fluids in porous media as a probe of surface-to-volume ratio. *J Magn Reson A*, 101(3):342–346.

Latour, L. L., Svoboda, K., Mitra, P. P., and Sotak, C. H. (1994). Time-dependent diffusion of water in a biological model system. *Proc Natl Acad Sci USA*, 91(4):1229–1233.

Lätt, J., Nilsson, M., van Westen, D., Wirestam, R., Ståhlberg, F., and Brockstedt, S. (2009). Diffusion-weighted MRI measurements on stroke patients reveal water-exchange mechanisms in sub-acute ischaemic lesions. *NMR Biomed*, 22(6):619–628.

Laule, C., Vavasour, I. M., Kolind, S. H., Li, D. K. B., Traboulsee, T. L., Moore, G. R. W., and MacKay, A. L. (2007). Magnetic resonance imaging of myelin. *Neurotherapeutics*, 4(3):460–484.

Le Bihan, D., Breton, E., Lallemand, D., Grenier, P., Cabanis, E., and Laval-Jeantet, M. (1986). MR imaging of intravoxel incoherent motions: Application to diffusion and perfusion in neurologic disorders. *Radiology*, 161(2):401–407.

Le Bihan, D., Delannoy, J., and Levin, R. L. (1989). Temperature mapping with MR imaging of molecular diffusion: Application to hyperthermia. *Radiology*, 171(3):853–857.

Le Bihan, D., Moonen, C. T. W., van Zijl, P. C. M., Pekar, J., and DesPres, D. (1991). Measuring random microscopic motion of water in tissues with MR imaging: A cat brain study. *J Comput Assist Tomogr*, 15(1):19–25.

Lee, J., Shmueli, K., Fukunaga, M., van Gelderen, P., Merkle, H., Silva, A. C., and Duyn, J. H. (2010). Sensitivity of MRI resonance frequency to the orientation of brain tissue microstructure. *Proc Natl Acad Sci USA*, 107(11):5130–5135.

Lee, J.-H. and Springer, C. S. (2003). Effects of equilibrium exchange on diffusion-weighted NMR signals: The diffusigraphic "shutter-speed". *Magn Reson Med*, 49(3):450–458.

Lee, M. K. and Cleveland, D. W. (1996). Neuronal intermediate filaments. *Annu Rev Neurosci*, 19:187–217.

Liu, C., Bammer, R., Acar, B., and Moseley, M. E. (2004). Characterizing non-Gaussian diffusion by using generalized diffusion tensors. *Magn Reson Med*, 51(5):924–937.

Ludwin, S. K. (1997). The pathobiology of the oligodendrocyte. *J Neuropathol Exp Neurol*, 56(2):111–124.

Lundell, H., Sønderby, C. K., and Dyrby, T. B. (2014). Diffusion weighted imaging with circularly polarized oscillating gradients. *Magn Reson Med*, doi: 10.1002/mrm.25211.

Lundgaard, I., Osório, M. J., Kress, B. T., Sanggaard, S., and Nedergaard, M. (2014). White matter astrocytes in health and disease. *Neuroscience*, 276C:161–173.

MacKay, A., Whittall, K., Adler, J., Li, D., Paty, D., and Graeb, D. (1994). In vivo visualization of myelin water in brain by magnetic resonance. *Magn Reson Med*, 31(6):673–677.

Maier, S. E., Bogner, P., Bajzik, G., Mamata, H., Mamata, Y., Repa, I., Jolesz, F. A., and Mulkern, R. V. (2001). Normal brain and brain tumor: Multicomponent apparent diffusion coefficient line scan imaging. *Radiology*, 219(3):842–849.

Malysz, T., Ilha, J., do Nascimento, P. S., Angelis, K. D., Schaan, B. D., and Achaval, M. (2010). Beneficial effects of treadmill training in experimental diabetic nerve regeneration. *Clinics*, 65(12):1329–1337.

Mansfield, P. (1977). Multi-planar image formation using NMR spin echoes. *J Phys C: Solid State Phys*, 10(3):L55–L58.

Marchadour, C., Brouillet, E., Hantraye, P., Lebon, V., and Valette, J. (2012). Anomalous diffusion of brain metabolites evidenced by diffusion-weighted magnetic resonance spectroscopy in vivo. *J Cereb Blood Flow Metab*, 32(12):2153–2160.

Mathai, J. C., Tristram-Nagle, S., Nagle, J. F., and Zeidel, M. L. (2008). Structural determinants of water permeability through the lipid membrane. *J Gen Physiol*, 131(1):69–76.

Mazel, T., Šimonová, Z., and Syková, E. (1998). Diffusion heterogeneity and anisotropy in rat hippocampus. *Neuroreport*, 9(7):1299–1304.

Medana, I. M. and Esiri, M. M. (2003). Axonal damage: A key predictor of outcome in human CNS diseases. *Brain*, 126(Pt 3):515–530.

Meier, C., Dreher, W., and Leibfritz, D. (2003). Diffusion in compartmental systems. i. a comparison of an analytical model with simulations. *Magn Reson Med*, 50(3):500–509.

Merboldt, K.-D., Hänicke, W., and Frahm, J. (1991). Diffusion imaging using stimulated echoes. *Magn Reson Med*, 19(2):233–239.

Mikula, S., Binding, J., and Denk, W. (2012). Staining and embedding the whole mouse brain for electron microscopy. *Nat Methods*, 9(12):1198–1201.

Mills, R. (1973). Self-diffusion in normal and heavy water in the range 1-45. *J Phys Chem*, 77(5):685–688.

Mitra, P. P. (1995). Multiple wave-vector extensions of the NMR pulsed-field-gradient spin-echo diffusion measurement. *Phys Rev B*, 51(21):15074–15078.

Mitra, P. P., Sen, P. N., and Schwartz, L. M. (1993). Short-time behavior of the diffusion coefficient as a geometrical probe of porous media. *Phys Rev B*, 47(14):8565–8574.

Mulkern, R. V., Gudbjartsson, H., Westin, C.-F., Zengingonul, H. P., Gartner, W., Guttmann, C. R., Robertson, R. L., Kyriakos, W., Schwartz, R. B., Holtzman, D., Jolesz, F. A., and Maier, S. E. (1999). Multi-component apparent diffusion coefficients in human brain. *NMR Biomed*, 12(1):51–62.

Murray, J. A. and Blakemore, W. F. (1980). The relationship between internodal length and fibre diameter in the spinal cord of the cat. *J Neurol Sci*, 45(1):29–41.

Nandigam, R. K. and Kroll, D. M. (2007). Three-dimensional modeling of the brain's ECS by minimum configurational energy packing of fluid vesicles. *Biophys J*, 92(10):3368–3378.

Nave, K.-A. and Trapp, B. D. (2008). Axon-glial signaling and the glial support of axon function. *Annu Rev Neurosci*, 31:535–561.

Nedergaard, M., Ransom, B. R., and Goldman, S. A. (2003). New roles for astrocytes: Redefining the functional architecture of the brain. *Trends Neurosci*, 26(10):523–530.

Nicholson, C. (2001). Diffusion and related transport mechanisms in brain tissue. *Rep Prog Phys*, 64(7):815–884.

Nicholson, C. and Syková, E. (1998). Extracellular space structure revealed by diffusion analysis. *Trends Neurosci*, 21(5):207–215.

Niendorf, T., Dijkhuizen, R. M., Norris, D. G., van Lookeren Campagne, M., and Nicolay, K. (1996). Biexponential diffusion attenuation in various states of brain tissue: Implications for diffusion-weighted imaging. *Magn Reson Med*, 36(6):847–857.

Nilsson, M., van Westen, D., Ståhlberg, F., Sundgren, P. C., and Lätt, J. (2013). The role of tissue microstructure and water exchange in biophysical modelling of diffusion in white matter. *MAGMA*, 26(4):345–370.

Novikov, D. S. and Fieremans, E. (2012). Relating extracellular diffusivity to cell size distribution and packing density as applied to white matter. In *Proceedings of the 20th Annual Meeting of ISMRM*, page 1829, Melbourne, Australia.

Novikov, D. S. and Kiselev, V. G. (2011). Surface-to-volume ratio with oscillating gradients. *J Magn Reson*, 210(1):141–145.

Oberheim, N. A., Goldman, S. A., and Nedergaard, M. (2012). Heterogeneity of astrocytic form and function. In Milner, R., editor, *Astrocytes*, volume 814 of *Methods in Molecular Biology*, pages 23–45. Humana Press.

Oberheim, N. A., Takano, T., Han, X., He, W., Lin, J. H. C., Wang, F., Xu, Q., Wyatt, J. D., Pilcher, W., Ojemann, J. G., Ransom, B. R., Goldman, S. A., and Nedergaard, M. (2009). Uniquely hominid features of adult human astrocytes. *J Neurosci*, 29(10):3276–3287.

Ogawa, S., Lee, T. M., Kay, A. R., and Tank, D. W. (1990). Brain magnetic resonance imaging with contrast dependent on blood oxygenation. *Proc Natl Acad Sci USA*, 87(24):9868–9872.

Ong, H. H. and Wehrli, F. W. (2010). Quantifying axon diameter and intra-cellular volume fraction in excised mouse spinal cord with q-space imaging. *NeuroImage*, 51(4):1360–1366.

Özarslan, E. (2009). Compartment shape anisotropy (CSA) revealed by double pulsed field gradient MR. *J Magn Reson*, 199(1):56–67.

Özarslan, E., Nevo, U., and Basser, P. J. (2008). Anisotropy induced by macroscopic boundaries: Surface-normal mapping using diffusion-weighted imaging. *Biophys J*, 94(7):2809–2818.

Parsons, E. C., Does, M. D., and Gore, J. C. (2003). Modified oscillating gradient pulses for direct sampling of the diffusion spectrum suitable for imaging sequences. *Magn Reson Imaging*, 21(3-4):279–285.

Parsons, E. C., Does, M. D., and Gore, J. C. (2006). Temporal diffusion spectroscopy: Theory and implementation in restricted systems using oscillating gradients. *Magn Reson Med*, 55(1):75–84.

Paus, T. and Toro, R. (2009). Could sex differences in white matter be explained by g ratio? *Front Neuroanat*, 3:14.

Perge, J. A., Koch, K., Miller, R., Sterling, P., and Balasubramanian, V. (2009). How the optic nerve allocates space, energy capacity, and information. *J Neurosci*, 29(24):7917–7928.

Perge, J. A., Niven, J. E., Mugnaini, E., Balasubramanian, V., and Sterling, P. (2012). Why do axons differ in caliber? *J Neurosci*, 32(2):626–638.

Perrins, W. T., McKenzie, D. R., and McPhedran, R. C. (1979). Transport properties of regular arrays of cylinders. *Proc R Soc Lond A*, 369(1737):207–225.

Portnoy, S., Flint, J. J., Blackband, S. J., and Stanisz, G. J. (2012). Oscillating and pulsed gradient diffusion magnetic resonance microscopy over an extended b-value range: Implications for the characterization of tissue microstructure. *Magn Reson Med*, 69(4):1131–1145.

Quirk, J. D., Bretthorst, G. L., Duong, T. Q., Snyder, A. Z., Springer, C. S., Ackerman, J. J. H., and Neil, J. J. (2003). Equilibrium water exchange between the intra- and extracellular spaces of mammalian brain. *Magn Reson Med*, 50(3):493–499.

Raff, M. C., Whitmore, A. V., and Finn, J. T. (2002). Axonal self-destruction and neurodegeneration. *Science*, 296(5569):868–871.

Rahbani, J., Behzad, A. R., Khashab, N. M., and Al-Ghoul, M. (2013). Characterization of internal structure of hydrated agar and gelatin matrices by cryo-sem. *Electrophoresis*, 34(3):405–408.

Reisert, M., Kellner, E., and Kiselev, V. G. (2012). About the geometry of asymmetric fiber orientation distributions. *IEEE Trans Med Imaging*, 31(6):1240–1249.

Rushton, W. A. H. (1951). A theory of the effects of fibre size in medullated nerve. *J Physiol*, 115(1):101–122.

Schmahmann, J. S., Smith, E. E., Eichler, F. S., and Filley, C. M. (2008). Cerebral white matter: Neuroanatomy, clinical neurology, and neurobehavioral correlates. *Ann N Y Acad Sci*, 1142:266–309.

Schwarz, G. (1978). Estimating the dimension of a model. *Ann Statist*, 6(2):461–464.

Sehy, J. V., Ackerman, J. J. H., and Neil, J. J. (2002). Evidence that both fast and slow water ADC components arise from intracellular space. *Magn Reson Med*, 48(5):765–770.

Sen, P. N. and Basser, P. J. (2005a). A model for diffusion in white matter in the brain. *Biophys J*, 89(5):2927–2938.

Sen, P. N. and Basser, P. J. (2005b). Modeling diffusion in white matter in the brain: A composite porous medium. *Magn Reson Imaging*, 23(2):215–220.

Sen, P. N., Scala, C., and Cohen, M. H. (1981). A self-similar model for sedimentary rocks with application to the dielectric constant of fused glass beads. *Geophysics*, 46(5):781–795.

Shemesh, N., Adiri, T., and Cohen, Y. (2011). Probing microscopic architecture of opaque heterogeneous systems using double-pulsed-field-gradient NMR. *J Am Chem Soc*, 133(15):6028–6035.

Shemesh, N., Álvarez, G. A., and Frydman, L. (2013). Measuring small compartment dimensions by probing diffusion dynamics via non-uniform oscillating-gradient spin-echo (NOGSE) NMR. *J Magn Reson*, 237:49–62.

Sigmund, E. E., Novikov, D. S., Sui, D., Ukpebor, O., Baete, S., Babb, J. S., Liu, K., Feiweier, T., Kwon, J., McGorty, K., Bencardino, J., and Fieremans, E. (2014). Time-dependent diffusion in skeletal muscle with the random permeable barrier model (rpbm): Application to normal controls and chronic exertional compartment syndrome patients. *NMR Biomed*, 27(5):519–528.

Silva, M. D., Omae, T., Helmer, K. G., Li, F., Fisher, M., and Sotak, C. H. (2002). Separating changes in the intra- and extracellular water apparent diffusion coefficient following focal cerebral ischemia in the rat brain. *Magn Reson Med*, 48(5):826–837.

Simpson, J. H. and Carr, H. Y. (1958). Diffusion and nuclear spin relaxation in water. *Phys Rev*, 111:1201–1202.

Siow, B., Drobnjak, I., Chatterjee, A., Lythgoe, M. F., and Alexander, D. C. (2012). Estimation of pore size in a microstructure phantom using the optimised gradient waveform diffusion weighted NMR sequence. *J Magn Reson*, 214(1):51–60.

Smith, S. M. (2002). Fast robust automated brain extraction. *Hum Brain Mapp*, 17(3):143–155.

Smith, S. M., Jenkinson, M., Woolrich, M. W., Beckmann, C. F., Behrens, T. E. J., Johansen-Berg, H., Bannister, P. R., Luca, M. D., Drobnjak, I., Flitney, D. E., Niazy, R. K., Saunders, J., Vickers, J., Zhang, Y., Stefano, N. D., Brady, J. M., and Matthews, P. M. (2004). Advances in functional and structural MR image analysis and implementation as FSL. *NeuroImage*, 23 Suppl 1:S208–S219.

Sotiropoulos, S. N., Behrens, T. E. J., and Jbabdi, S. (2012). Ball and rackets: Inferring fiber fanning from diffusion-weighted MRI. *NeuroImage*, 60(2):1412–1425.

Stanisz, G. J., Kecojevic, A., Bronskill, M. J., and Henkelman, R. M. (1999). Characterizing white matter with magnetization transfer and T(2). *Magn Reson Med*, 42(6):1128–1136.

Stanisz, G. J., Szafer, A., Wright, G. A., and Henkelman, R. M. (1997). An analytical model of restricted diffusion in bovine optic nerve. *Magn Reson Med*, 37(1):103–111.

Stejskal, E. O. and Tanner, J. E. (1965). Spin diffusion measurements: Spin echoes in the presence of a time-dependent field gradient. *J Chem Phys*, 42(1):288–292.

Stepišnik, J. (1993). Time-dependent self-diffusion by NMR spin-echo. *Physica B*, 183(4):343–350.

Stepišnik, J., Mohorič, A., and Duh, A. (2001). Diffusion and flow in a porous structure by the gradient spin echo spectral analysis. *Physica B*, 307(1-4):158–168.

Stikov, N., Perry, L. M., Mezer, A., Rykhlevskaia, E., Wandell, B. A., Pauly, J. M., and Dougherty, R. F. (2011). Bound pool fractions complement diffusion measures to describe white matter micro and macrostructure. *NeuroImage*, 54(2):1112–1121.

Sugiyama, M., Takao, M., Hatsuta, H., Funabe, S., Ito, S., Obi, T., Tanaka, F., Kuroiwa, Y., and Murayama, S. (2013). Increased number of astrocytes and macrophages/microglial cells in the corpus callosum in amyotrophic lateral sclerosis. *Neuropathology*, 33(6):591–599.

Szafer, A., Zhong, J., and Gore, J. C. (1995). Theoretical model for water diffusion in tissues. *Magn Reson Med*, 33(5):697–712.

Tanner, J. E. and Stejskal, E. O. (1968). Restricted self-diffusion of protons in colloidal systems by the pulsed-gradient, spin-echo method. *J Chem Phys*, 49(4):1768–1777.

Tao, A., Tao, L., and Nicholson, C. (2005). Cell cavities increase tortuosity in brain extracellular space. *J Theor Biol*, 234(4):525–536.

Tijssen, R. H. N., Jenkinson, M., Brooks, J. C. W., Jezzard, P., and Miller, K. L. (2014). Optimizing retroicor and retrokcor corrections for multi-shot 3D fMRI acquisitions. *NeuroImage*, 84:394–405.

Transvalidou, F. and Sotirchos, S. V. (1996). Effective diffusion coefficients in square arrays of filament bundles. *AIChE J*, 42(9):2426–2438.

Tuch, D. S., Reese, T. G., Wiegell, M. R., Makris, N., Belliveau, J. W., and Wedeen, V. J. (2002). High angular resolution diffusion imaging reveals intravoxel white matter fiber heterogeneity. *Magn Reson Med*, 48(4):577–582.

Van, A. T., Holdsworth, S. J., and Bammer, R. (2014). In vivo investigation of restricted diffusion in the human brain with optimized oscillating diffusion gradient encoding. *Magn Reson Med*, 71(1):83–94.

Wang, D. D. and Bordey, A. (2008). The astrocyte odyssey. *Prog Neurobiol*, 86(4):342–367.

Wang, S. S.-H., Shultz, J. R., Burish, M. J., Harrison, K. H., Hof, P. R., Towns, L. C., Wagers, M. W., and Wyatt, K. D. (2008). Functional trade-offs in white matter axonal scaling. *J Neurosci*, 28(15):4047–4056.

Weruaga-Prieto, E., Eggli, P., and Celio, M. R. (1996). Topographic variations in rat brain oligodendrocyte morphology elucidated by injection of lucifer yellow in fixed tissue slices. *J Neurocytol*, 25(1):19–31.

Wolf, J. A., Stys, P. K., Lusardi, T., Meaney, D., and Smith, D. H. (2001). Traumatic axonal injury induces calcium influx modulated by tetrodotoxin-sensitive sodium channels. *J Neurosci*, 21(6):1923–1930.

Wolff, S. D. and Balaban, R. S. (1989). Magnetization transfer contrast (MTC) and tissue water proton relaxation in vivo. *Magn Reson Med*, 10(1):135–144.

Wong, E. C. (2012). Local head gradient coils: Window(s) of opportunity. *NeuroImage*, 62(2):660–664.

World Health Organization (2008). *Atlas: Multiple Sclerosis Resources in the World 2008*, page 14. WHO Press, Geneva.

Wright, P. J., Mougin, O. E., Totman, J. J., Peters, A. M., Brookes, M. J., Coxon, R., Morris, P. E., Clemence, M., Francis, S. T., Bowtell, R. W., and Gowland, P. A. (2008). Water proton T1 measurements in brain tissue at 7, 3, and 1.5 T using IR-EPI, IR-TSE, and MPRAGE: Results and optimization. *MAGMA*, 21(1-2):121–130.

Xu, J., Does, M. D., and Gore, J. C. (2009). Quantitative characterization of tissue microstructure with temporal diffusion spectroscopy. *J Magn Reson*, 200(2):189–197.

Xu, J., Li, K., Smith, R. A., Waterton, J. C., Zhao, P., Chen, H., Does, M. D., Manning, H. C., and Gore, J. C. (2012). Characterizing tumor response to chemotherapy at various length scales using temporal diffusion spectroscopy. *PLoS ONE*, 7(7):e41714.

Yablonskiy, D. A., Bretthorst, G. L., and Ackerman, J. J. H. (2003). Statistical model for diffusion attenuated MR signal. *Magn Reson Med*, 50(4):664–669.

Zhang, B., Yen, Y.-F., Chronik, B. A., McKinnon, G., Schaefer, D. J., and Rutt, B. K. (2003). Peripheral nerve stimulation properties of head and body gradient coils of various sizes. *Magn Reson Med*, 50(1):50–58.

Zhang, Y. and Barres, B. A. (2010). Astrocyte heterogeneity: An underappreciated topic in neurobiology. *Curr Opin Neurobiol*, 20(5):588–594.